Atomic Scale Defects in Thin Film Solar Cell Materials from *ab initio* Calculations

Dissertation
zur Erlangung des Grades
„Doktor der Naturwissenschaften“
im Promotionsfach Chemie

Fachbereich Chemie, Pharmazie und Geowissenschaften
der Johannes Gutenberg-Universität Mainz

vorgelegt von
Elaheh Ghorbani
Nohadanimoghaddam
geboren in Rasht/Iran

Mainz, 2016

List of symbols and abbreviations

Al	aluminium
CB	conduction band
CBD	chemical bath deposition
CBM	conduction band minimum
Cd	cadmium
CdS	cadmium sulfide
CIGSe	$Cu(In,Ga)Se_2$
CI-NEB	climbing image nudged elastic band
Cu	copper
CZTSe	$Cu_2ZnSnSe_4$
DFT	density functional theory
Ga	gallium
GGA	generalized gradient approximation
GS	ground state
HF	Hartree Fock theory
HSE06	Heyd-Scuseria-Ernzerhof screened-exchange hybrid functional
In	indium
K	potassium
KF	potassium fluoride
KS	Kohn-Sham theory
LDA	local density approximation
Li	lithium
LSD	local spin-density approximation
LZ	Lany and Zunger approach

MEP	minimum energy path
Na	sodium
NaF	sodium fluoride
NEB	nudged elastic band
oc	octahedrally coordinated
OVC	ordered vacancy compound
PBE	Perdew, Burke, and Ernzerhof approximation
PDT	post deposition treatment
PEB	plain elastic band
PES	potential energy surface
PV	photovoltaic
SCR	space charge region
S	sulphur
Se	selenium
SLG	soda-lime glass
Sn	tin
SRH	Shockley-Read-Hall recombination
TCO	transparent conductive oxide
TST	transition state theory
VBM	valance band maximum
Zn	zinc
ZnO	zinc oxide

Å	angstrom
eV	electron volt, unit of energy
ϵ	dielectric constant
ϵ_0	dielectric constant of vacuum
η	tetragonal elongation
E_{C}	conduction band
E_{g}	band gap

E_{V}	valance band
h	Planck's constant
I_{drift}	drift current
I_{diff}	diffusion current
K_B	Boltzmann constant
μ	chemical potential
μ_e	electron chemical potential
μm	micrometer, unit of length
ν	frequency
ϕ	diffusion flux
T	temperature
V_{bi}	built-in voltage

Abstract

CIGSe and CZTSe compounds are widely accepted as light absorber layer in efficient and inexpensive thin film solar cells. To further boost the efficiency of CIGSe and CZTSe thin film devices, it is crucial to understand the effects of various defects in these materials. Since the experimental investigations are often hampered by the complex nature of the device, in this thesis a detailed study have been performed to calculate the formation energies and activation energies along the diffusion path of alkaline impurities in $CuInSe_2$ (the bulk CIGSe absorber layer), $CuIn_5Se_8$ (the Cu-poor ordered vacancy compound) and $Cu_2ZnSnSe_4$ (the bulk CZTSe absorber layer).

I have carried out hybrid functional computations on Na and K extrinsic defects in $CuInSe_2$ and $CuIn_5Se_8$, and Li, Na and K defects in the CZTSe solar cell material. The formation energy calculation shows that in CISe Na is mostly incorporated either in form of interstitial defects coordinated by cations, or into dumbbells in the Cu sublattice. However, due to its large atomic radius K does not form interstitial defects. In $CuIn_5Se_8$, both Na and K prefer to occupy the pristine Cu vacancy sites either as point defects, or by forming dumbbells. In CZTSe similar to $CuInSe_2$, the most favourable way to incorporate Na, K and also Li impurities is to form substitutional defects in the copper sub-lattice. In general, the formation energy of Na-related defects are lower than the corresponding K impurities in all studied sites in both CISe and CZTSe.

Besides the static calculations, the migration of point defects in CISe and CZTSe have been also investigated through the climbing image nudged elastic band (CI-NEB) method. These calculations reveal that in both CISe and CZTSe, the V_{Cu} native defect contributes to the vacancy mediated mass transport mechanism. Since Na interstitials have a very low diffusion barrier both in the CISe and CZTSe materials, their diffusion is feasible even at relatively low temperatures.

Contents

Chapter 1

Introduction and Motivation

1.1 Motivation

The global energy demand is constantly on the rise, whereas the available oil products, natural gas, coal and uranium resources are dwindling worldwide. In addition to the rising price of these resources, fossil fuel combustion impose serious detrimental damage on the environment. Namely, burning fossil fuels cause air pollution in form of sulphur dioxide and nitrous oxides and other undesired by-products. These can lead to serious health problems, especially around densely populated areas, and the CO_2 gas promote global warming by the green-house gas effect. Nuclear energy on the other hand produces large amounts of highly radioactive waste, which is very dangerous both for people and for the environment. Hence, the currently mainstream energy resources are not sustainable, especially considering that third world countries have just started building out their infrastructure, which will lead to a sudden jump in the price of these limited energy carriers and the pollution caused.

Therefore, we clearly need to look for alternative renewable energy resources being able to substitute fossil fuel, which are ecologically more friendly. These alternatives are water power, wind power and solar energy. Worldwide so far these alternatives are not yet major contributors to the amount of energy produced. This is mainly because the paradigm shift towards such alternative energy resources have not been made by many

countries. Still, due to the ongoing efforts, renewable energy did provide already 30% of electricity production in the EU in 2014, and this value is on the rise.

One of the very promising alternatives is photovoltaics (PV), where PV devices convert sunlight directly into electricity. Replacing fossil fuels with PV (especially in combination with wind farms) is a viable approach because there are numerous advantages. Solar energy is renewable and abundant being available in most parts of the globe. It is sustainable, and once the PV devices have been manufactured and installed, there is no further air pollution created, because there is no need to burn coal, oil or gas.

The main factors which slow down the more widespread application of PV and renewable energies in general is the relative high price per Watt of energy produced compared to traditional resources. Furthermore, PV as renewable energy is often being criticized due to its intermittence and seasonality of sunlight, since no energy is created at night and under substantial cloud cover. The storage technologies for power generated from renewable resources, such as ultra high energy-density batteries, super-capacitors and spinning mechanical wheels are still in their infancy. Additionally, some PV solar cells contain expensive, rare and toxic materials.

In spite of these shortcomings, PV technologies are being constantly improved, leading to more competitive products from the perspective of the price to power ratio. Among PV devices one important field is concerning the thin film solar cells. This is because in thin film polycrystalline devices a smaller amount of light absorber material is used. Hence, these thin film cells offer comparable efficiency at a lower price point compared to single crystal devices. This means that thin film PV offers a good remedy for one of the major drawbacks of solar energy by providing high power output for an affordable price, and they are being industrially fabricated and deployed on a massive scale.

In order to make the energy produced by thin-film PV more affordable, their efficiency has to be improved. However, the improvement via trial-and-error procedure via experimental studies and investigations on the pilot scale are both very time and resource consuming. Furthermore, due to the complex structure of a thin-film device, their experimental investigation is rather cumbersome, and in many cases new insights from theoretical calculations are needed to explain and interpret the measured data. There-

fore, in this thesis I have carried out calculations based on first principles to support experimental findings and to contribute to the understanding of the atomic and electronic structure of the materials and impurities in the respective compounds.

1.2 Timeline and Progression of Solar Cells

In solar cells the sunlight is converted into electric current through the photovoltaic effect. Solar cells are fabricated by sandwiching an n-type and a p-type semiconductor forming a p-n junction between two conducting layers, which serve as electrodes to extract the power generated. The discovery of photovoltaic effect is credited to Edmond Becquerel, who has made the world's first photovoltaic cell in 1839. More than a century after his discovery in the 1950s, the first solar cell devices have been produced based on single-crystal silicon in the Bell Labs, which have been used for space exploration. Due to their success, after this peculiar niche application solar cells have received more widespread attention and commercial interest. Since the 1970s solar cells based on single-crystalline and polycrystalline Si have been commercially dominating the PV market. This is why Si solar cells are often being referred as first generation cells. The current record efficiency of the best laboratory scale cells of traditional single crystal silicon is 25.6% [1], and that of polycrystalline Si is 20.8% [1]. Although Si cells are reliable and clean renewable energy resources, due to the indirect band gap of Si the cell thickness has to be about 250 micrometer (μm) to show reasonable conversion efficiencies. Therefore, for efficient Si based PV devices relatively large amounts of single crystalline Si is needed, which makes these devices expensive. This is why it was highly desirable to develop new materials with high light absorption which can be used for light harvesting, leading to the development of so called second generation solar cells. Due to the relatively thin layer of the light absorber material in these devices they are called thin film solar cells. Currently the commercially successful thin film cells employ amorphous silicon, cadmium telluride (CdTe), copper indium gallium selenide (CIGSe), copper zinc tin selenide (CZTSe) or copper zinc tin sulphur selenide (CZTSSe) as light absorber. Because of the thin polycrystalline semiconductor

layer, which is easy and quick to deposit, thin film cells have been cheaper but somewhat less efficient than single crystal Si cells. The record efficiency reached so far for CdTe cells is 21.5% [1], for CIGS cells is 21.7% [1], for CZTSe 9.1% [1] and 12.6% for CZTSSe cells, respectively.

Third generation solar cells consist of multiple p-n junctions made of different thin film semiconductors. These different thin film layers have various band gaps to allow the device to absorb electromagnetic radiations from a wider range of the solar spectrum. A triple junction cell, for example, may contain GaAs, Ge and $GaInP_2$. Hence, multi-junction cells on the laboratory scale have exhibited efficiency of over 38%. In addition to the semiconductor light absorber, there are also some other types of PV devices such as organic, perovskite and dye-sensitized solar cells which show efficiencies in the range of 11% to 20%. However, these cells are rather unstable, because these light absorbers are highly sensitive to moisture and solar radiation.

1.3 Operation of Solar Cells

Solar cells operate based on the photovoltaic effect. When a p-type and a n-type semiconductor is electrically connected, they form a p-n junction. When the bulk compound from which the n-type and p-type doped materials were derived are the same, the p-n junction is called a homojunction, whereas in the other case the resulting p-n junction is called a heterojunction. In the vicinity of the p-n junction excess electrons diffuse from high electron concentration region (from the n-type semiconductor) to the p-type layer and recombine with the holes on the p-type side. Similarly, holes diffuse from the p-type semiconductor to the n-type semiconductor and recombine with the electrons of the n-type side. Due to this phenomenon an electron-hole free region is constructed at the interface region, known as space charge region (SCR). The width of the SCR can be formulated as [2]:

$$W = W_n + W_p = \left(\frac{2\epsilon\epsilon_0}{q} \frac{N_A + N_D}{N_A N_D} \right) V_{bi} \tag{1.1}$$

where ϵ is the dielectric constant of the semiconductor, ϵ_0 is the dielectric constant of vacuum, N_{A} and N_{D} are the acceptor and the donor concentration in the p-type and n-type material respectively, and V_{bi} is the built-in voltage. As a consequence of charge separation, an electric field will be generated at the p-n interface. The presence of this internal electric field allows electrons to flow from the p-side to the n-side, but not the other way. So, there are two opposing currents which compensate each other in the lack of an external voltage:

$$I_{drift} + I_{diff} = 0 \tag{1.2}$$

I_{drift} corresponds to the drift current and I_{diff} correspond to the diffusion current.
Due to the photovoltaic effect, a photon with energy larger than the band gap of the semiconductor can be absorbed into the light absorber layer, and produce an electron-hole pair. The electron and hole are then separated due to the presence of the electric field. So, electrons are sent to the anode region and holes are sent to the cathode region, causing the accumulation of charge across the p-n junction of the diode. Consequently, by providing an external circuit between the anode and the cathode, electrons in the diode can return to the other layer. This current flow will continue as the solar cell is exposed to light. The electrons can flow through the external circuit, yielding a current I in the external circuit, which can be used to power external electronic devices.
In a heterojunction solar cell, photo-excited electrons originating from the conduction band may reduce their energy through recombination. There are three possible recombination processes. In a band-to-band recombination, an electron will occupy an empty state in the valance band and emit a photon with the energy difference between the conduction and valence band $E_{\mathrm{C}} - E_{\mathrm{V}}$. The second type of recombination is called Auger-recombination, which involves three carriers. An electron and a hole recombine, but instead of emitting a photon, the energy is transferred to an electron in the conduction band E_{C}. The third type of recombination is the so called Shockley-Read-Hall recombination (SRH). SRH recombination through defect states occurs in materials containing impurities. Recombinations deteriorate the device performance since these

charge carriers are lost and cannot be collected and used at the external circuit. This is why it is highly important to investigate the various defects and impurities in the light absorber materials.

1.4 Structure of Thin-Film Solar Cell Devices

The main focus of this thesis is the theoretical study of defects, dopants and impurities and their diffusion in the light absorber materials used in thin-film solar cells. A cross section of a thin-film solar device is presented in Fig. 1.1. In this section of the thesis a brief description is presented regarding the function of each individual layer building up a thin-film cell to provide an overview of the materials and interfaces which occur in such a device.

During the manufacturing process, first on top of the substrate (often soda lime glass) the back contact is deposited (mostly metallic molybdenum layer), then the light absorber layer (thin film of CIGS, CZTSe or CZTSSe) is grown on the back contact. A buffer layer (often CdS in a wet chemical process) is being deposited on top of the light absorber. A transparent ZnO layer is on top of the buffer, and on top of the ZnO the front contact (mostly ZnO doped with Al to make it highly conductive, but still transparent) is deposited. Finally, to reduce the amount of light reflected, and thereby improve slightly the overall efficiency, the device is coated by an anti-reflective layer (mostly MgF_2).

1.4.1 Substrates

There are several types of substrates that can be used for thin film chalcogenide solar cells, such as soda-lime glass (SLG) [3] and metal foils (like stainless steel or titanium) [4], and for highly flexible solar cell applications heat resistant polyimide tapes are used. The most important characteristics of good substrates are: mechanical stability, vacuum compatibility, thermal stability, suitable thermal expansion and chemical inertness. Today SLG is the most extensively used substrate due to its favorable prop-

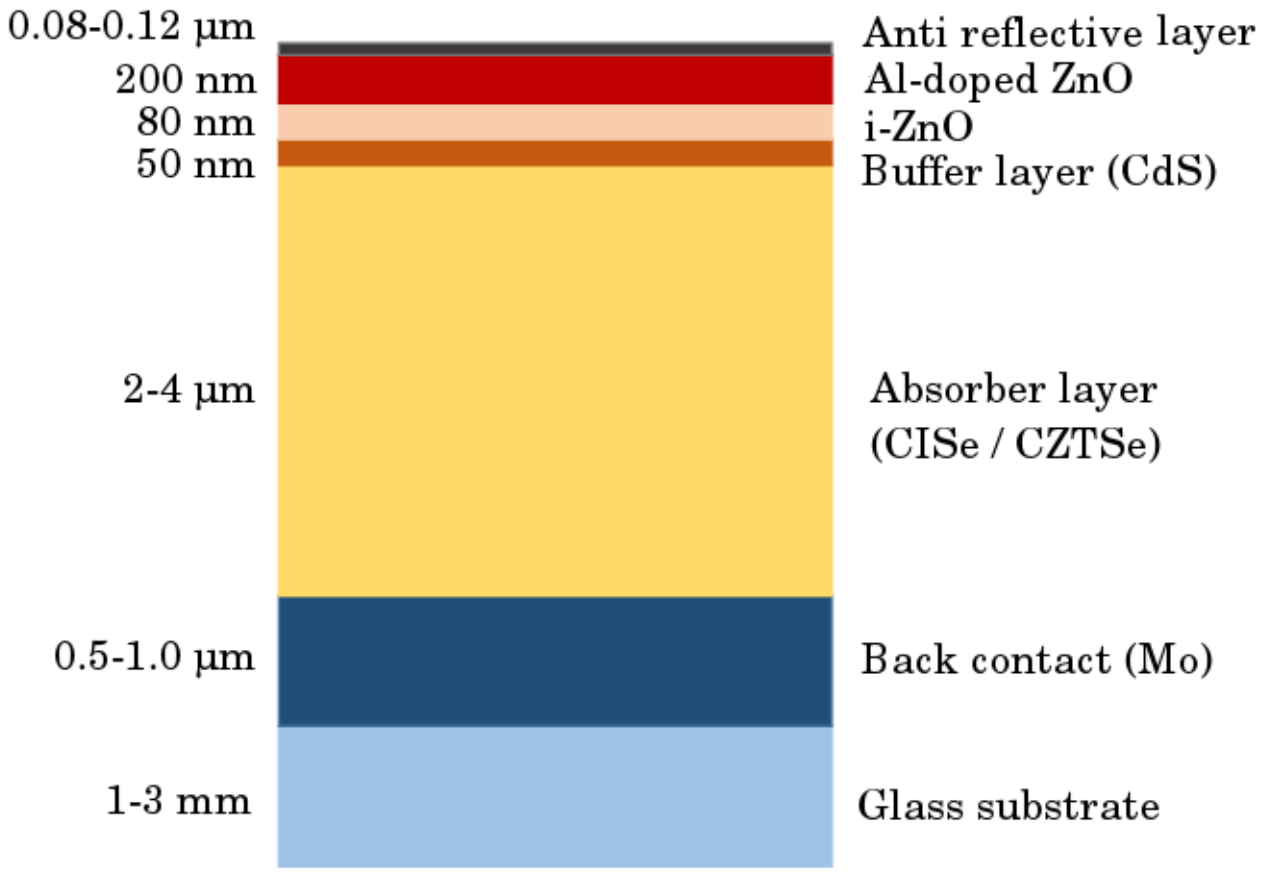

Figure 1.1: Structure of a thin-film solar cell (not drawn to scale) showing the different layers involved in the PV device.

erties and low price. More importantly, SLG contains alkali elements which diffuse into the CIGS absorber layer. As it will be discussed in Section 1.5.1, these alkali impurities are incorporated into the light absorber, which improves the device efficiency.

1.4.2 Back Contact

As back contact, in most commercially available cells a molybdenum (Mo) layer with a thickness of 0.5-1.0 μm is deposited on SLG to serve as the back contact for the device, where the power generated by the cell can be extracted for the external circuit. Mo establishes good adherence to the glass substrate and provides an electric contact with low resistivity [5]. In addition to serving as one of the electrodes, Mo also functions in a thin-film solar device as diffusion barrier. This is because during the growth of the

light absorber, the Mo layer has control over the outward diffusion of various elements from SLG into the absorber layer. Another positive characteristic of Mo is that it does not diffuse into the CIGS layer. For comparison, by using cold rolled stainless steel as substrate and back contact, iron and chromium contaminants are often diffusing into the light absorber, which is undesired.

The main drawback of Mo has been assigned to its low reflectivity [6]. When really thin light absorber with the thickness of lower than 2 μm are used in the PV device, the absorber layer can not soak up all of the incident photons with energies larger than the band gap. These photons should be reflected back towards the front contact, so that they are absorber at the second pass through the light absorber layer. Therefore, in films with really thin absorber material a back contact with higher reflectivity compared to Mo should be used to improve efficiency.

1.4.3 Light Absorber Layer

$Cu(In,Ga)(S,Se)_2$ (CIGS) is one of the most promising materials in PV for thin film applications. Currently cells based on CIGS are the most efficient devices among single-junction thin film solar cells. Beside the high efficiency, another important feature of this material is that it can be produced by several methods [7–12]. In contrast to crystalline silicon, CIGS has a direct band gap (Eg) and therefore has a higher absorption coefficient. The absorption coefficient for a photon energy of $h\nu = E_g + 0.2\,\mathrm{eV}$ is $2{\times}10^5$ cm^{-1} for $CuInSe_2$ and $1{\times}10^3$ cm^{-1} for silicon, respectively [13]. The band gap in the CIGS alloy varies continuously from 1.04 eV (pure $CuInSe_2$) to about 1.7 eV for $CuGaSe_2$ [14–20]. The energy of valance band maximum (E_V) remains fixed, however the energy of conduction band (E_C) shifts up and down, depending on the In and Ga ratio.

Ga and especially indium in CIGS are rather rare elements in the Earth's crust, so this natural material shortage could limit the production of CIGS-based solar cells. On the other hand, $Cu_2ZnSn(S,Se)_4$ (CZTSSe) which consist of earth abundant and inexpensive materials has been regarded as an alternative absorber layer and has attracted a

lot of research interest in the last years. The indium and gallium in CIGS is substituted by the elements zinc and tin. The optoelectronic properties of Cu_2ZnSnS_4 (CZTS) were investigated by Ito *et al.* in 1988 [21]. According to their report, CZTS thin films with p-type conductivity exhibit absorption coefficient greater than 10^4 cm^{-1}. A direct optical band gap of 1.45 eV also makes CZTS a suitable material for thin film solar cells. The highest reported efficiency of 12.6% for CZTSSe was reached in 2014 by IBM [22], which suggest great potential for low cost and high efficiency solar cells.

$CuInSe_2$ and $CuGaSe_2$

$CuInSe_2$ (CISe) and $CuGaSe_2$ (CGSe) crystallises in the chalcopyrite structure which can be obtained by doubling the zinc-blende structure along the c-axis. Because of the two different cation types, the primitive cell of chalcopyrite structure consist of eight atoms and not two as in case of zinc-blende structure. Also, the Se anions will have a free structural parameter u, which depends on the In and Ga cation. Cu, In and Se atoms occupy $4a$, $4b$ and $8d$ lattice sites, respectively, with the crystal coordinates:
Cu atoms assemble in (0.0, 0.0, 0.0) and (0.0, 0.5, 0.5) sites,
In atoms assemble in (0.5, 0.5, 0.0) and (0.5, 0.0, 0.25) sites,
Se atoms assemble in (u, 0.75, 0.125), (0.75, u, 0.875) and (0.25, u, 0.875) sites.
u is the anion displacement parameter. The anions (here Se atoms) are slightly displaced from their ideal tetrahedral sites compared to the zinc-blende structure due to the existence of two cation sublattices rather than one. Se atoms are located closer to Cu atoms than to In atoms because of the larger size of In. The value of u as a function of the a and c cell parameters is given by the formula:

$$u = \frac{1}{2} - \left[\frac{c^2}{32a^2} - \frac{1}{2}\right]^{\frac{1}{2}} \tag{1.3}$$

The experimentally measured value for u is $u = 0.224$ [23] for $CuInSe_2$, where $u = 0.25$ corresponds to the central position in a zinc-blende lattice. In order to increase the band gap, In and Ga atoms share $4b$ lattice sites randomly ($CuIn_xGa_{1-x}Se_2$). The lattice parameter of $CuGaSe_2$ is smaller than $CuInSe_2$, however its band gap increases to 1.7 eV

and the anion displacement equals to 0.25 [23,24]. The conventional tetragonal unit cell of the chalcopyrite structure consist of 16 atoms. In the ternary chalcopyrite structure, each atom has four neighbours and according to the Grimm-Sommerfeld rule, there must be an average of 4 valence electrons per atomic site. So, each atom is surrounded by four neighbouring atoms which are placed at the corners of a common tetrahedron. Each Se atom is coordinated by two Cu and two In atoms, and each cation (i. e. Cu or In) is tetrahedrally coordinated by four Se atoms. Due to the tetragonal elongation along the c axis, the c/a ratio deviates from the ideal value of 2.0.

In a thin film PV cell at the vicinity of the CdS buffer layer a hetero-junction is formed between a p-type CIGS and a highly Cu-poor CIGS phase [25]. The latter is widely accepted to be an ordered vacancy compound (OVC) [26–28], consisting of ordered Cu vacancies and In atoms located on Cu positions as anti sites. The exact physical and chemical properties of these Cu-poor regions are not fully clear as of yet, and their effect upon the cell efficiency is still subject to scientific debates. Among all possible Cu-poor ordered vacancy structures, the $CuIn_3Se_5$ and $CuIn_5Se_8$ stoichiometries were the ones which have drawn particular interests and have been investigated widely. A more detailed discussion on the formation of $CuIn_5Se_8$ will be given as part of the results and discussions.

Cu_2ZnSnS_4 and $Cu_2ZnSnSe_4$

In 2009, Chen *et al.* investigated the structural and electronic properties of CZTS and CZTSe quaternary compounds. They reported three crystal structures for CZTSe, that all obey the octet rule. The ground state structure for CZTSe is the kesterite structure (KS), which is derived from the chalcopyrite (CH) structure. However CZTSe can also be formed in the stannite (ST) and primitive mixed CuAu-like (PMCA) structures. Both ST and PMCA structures are derived from the CuAu-like (CA) structures [29]. In practice when these films are grown, the polycrystalline thin film consists predominantly by the KS form. In ternary compounds, CH structures have larger band gap and are also more stable than CA structures, and CA structures are expected to exist in vapour phase, and the formation energy difference E_f(CA)-E_f(CH) is very small [30].

Similar to their ternary analogues, KS structures have lower total energy, Madelung energy and strain energy compared to the ST and PMCA structures [31, 32].
To study the structural properties of kesterites and stannites conventional X-ray diffraction can not be used. Since Cu^{+} and Zn^{2+} both have 28 electrons, therefore both cations are indistinguishable. In 2007, Schorr *et al.* have carried out neutron diffraction measurements [33, 34]. They obtained a new ordering for $Cu_2ZnSnSe_4$, in which, the atoms in the Cu+Zn (001) layer are disordered, while the Sn atoms remain on their sites unaffected, known as partially disordered KS (PD-KS).
Tuning the band gap of the kesterite structure is feasible through adjusting the S/(S+Se) ratio. The band gap of pure CZTS is around 1.5 eV and the band gap of pure CZTSe is around 1.0 eV [35, 36].

Buffer Layer

On top of the light absorber layer a very thin n-type buffer layer is added in order to create a pn-junction in the thin-film PV device between the p-type absorber and the n-type buffer. The heterojunction should show maximum light admittance as well as being able to pump the created charge carriers through the outer circuit with minimal recombination and electrical resistance losses [37]. To improve the optical output as well as having minimum resistive loss, the buffer layer requires to have a wide band gap for limited light absorption and also it should be as thin as possible. The ideal pn-junction in a solar cell should separate holes from electrons, and allow only one carrier type to pass. To reach this goal, a large difference between the band gaps of p-type and n-type materials should be yielded by providing a wide band gap buffer layer in contrast with optimal low band-gap absorber layer.
The oldest buffer layer material used in the fabrication of thin-film PV cells is cadmium sulphide (CdS) with the band gap of 2.4 eV, which has been studied vastly since 1954. CdS is deposited between the absorber layer and the transparent front electrode (front contact) via chemical bath deposition (CBD) technique, which is a wet chemical process in the presence of a solution containing ammonia and chelating ligands [38].
The standard CIGS/CZTSe based solar cells contain roughly 50nm thick CdS buffer

layer to boost efficiency. Since Cd is a toxic element, and also a wider band-gap material is expected to have lower light absorption, considerable efforts have been made during the last decade, to find an alternative low-absorbing material for CdS, that can serve as buffer layer. The current loss of CIGS devices due to using CdS layer is believed to be in the range of $1\,\mathrm{mA/cm^2}$ [39]. The zinc oxysulfilde (ZnS(O,OH)) buffer layer is one of the most accepted alternative materials for substituting the CBD CdS. ZnS(O,OH) is non-toxic, and has relatively lower price. Due to the recent progress made with ZnS(O,OH) buffer, the newest record efficiency CIGSe based cells have been produced with ZnS(O,OH).

Front Contact

The buffer layer is overlaid with a thin transparent conductive oxide (TCO) [40, 41]. This TCO most commonly consist of a ZnO [42] bilayer used to manufacture the front contact in CIGS and CZTSe thin-film solar cells. In this bilayer the first layer is a thin intrinsic ZnO (i-ZnO) with a thickness of 80 nm and the second layer is a heavily aluminium doped ZnO (ZnO:Al) [43] with a typical thickness of around 200 nm. The ZnO:Al window layer is usually deposited by DC sputtering method, which is often damaging the upper layer [44], so the i-ZnO layer is applied to protect the underlying CdS and the absorber layer from this damage.

1.5 The Importance of Defects in Solids

Defects play an influential role in determining the properties of most materials, in particular that of semiconductors. From the perspective of the electrical and optical characteristics, in order to fine tune their properties to obtain desired characteristics, defects in solids have been widely exploited. More importantly, the general knowledge on the pivotal building blocks of the entire electronics industry – such as diodes, transistors, optoelectronics and solar cells – grew incrementally by understanding and manipulating point defects.

Defects in solids can be categorized into four types: point defects, line defects, planar defects and volume defects. Point defects which are known as zero-dimensional defects are formed by an imperfection at a single atomic site. Point defects can be distinguished as intrinsic and extrinsic defects. An intrinsic point defect is formed when an atom is absent from its common position known as vacancy, or when an exchange of occupation occurs between atoms of different types called antisite defects, or when an atom occupies a crystal site which is usually unoccupied, called an interstitial defects. The extrinsic point defects are foreign atoms, often being referred as impurities, that are incorporated into the materials purposely or accidentally. An extrinsic defect is called a substitutional defect when it occupies a lattice site and is called a interstitial defect when it fills an interstitial site. Line defects or one-dimensional defects include dislocations in the crystal. Planar defects or two-dimensional defects include surfaces and grain boundaries. Volume defects or three-dimensional defects include rods, tubes and point defect clusters [45].

Impurities can boost the performance of solar cell devices by introducing shallow acceptor levels or passivating deep levels. On the other hand they can also have detrimental influence on device performance by forming recombination centers. To understand both the constructive and harmful effects of impurities, a detailed knowledge on the role of impurities in solar cells is essential.

Measurements regarding the defect concentration and especially concerning the migration barrier of defects are hindered by the highly complex nature of thin-film solar cells. Also, the experimental determination of material properties related to defects are further hampered by the sample stoichiometry and quality and they are also suspect to the given experimental conditions. In practice, diverse experimental techniques have been combined together to measure defect characteristics. Therefore, first principle calculations are regarded as an important method for complementing experimental results, contributing to their interpretation, and even anticipating some material properties in advance, before measurements are available [46]. Density Functional Theory (DFT) is a well respected tool in materials research and is regarded as a powerful means for shedding light on different prospects on the defect physics of semiconductors. The con-

tribution of DFT calculations to the general knowledge of defect physics produces very useful information on atomic and electronic structure, wave functions, charge densities, potentials, and total energy of the system [47,48]. The evaluation of all this data in combination with the experimental results contributes to the explanation of the properties of impurities and point defects.

1.5.1 The Role of Na and K in the Light Absorber Layers

Among a wide range of potential external defects, Na is the most remarkable and thoroughly investigated impurity in CIGS. This is because after the seminal work of Hedstroem *et al.* [49] in 1993 it was found that Na impurities play a pivotal role in the efficiency of thin film solar cells. In related experimental works in the contemporary literature similar investigations have been carried out for CZTS and CZTSe absorber layers as well. Very recently it has been established, that in addition to Na, the incorporation of small amounts of K (with the concentration of around 0.1 atomic percent) into the CIGSe layer also result in an increase in the efficiency of the PV solar-cell devices [3, 50].

The most straightforward and extensively used source for introducing alkaline elements in the absorber layer was their outward diffusion from SLG through the Mo back contact. In addition to this alkali source from SLG, other different techniques have been explored as well, especially focusing on ion implantation and post deposition treatment (PDT). PDT has drawn a great deal of attention in recent years. During PDT, alkaline elements are introduced to the system when the growth process of the absorber layer is finished. It has been shown experimentally that through PDT with NaF [51] and/or KF [52] salts the concentration of holes in CIGS layer increased which has a beneficial effect on the performance of solar cells. According to these findings it has been also shown that alkaline elements largely segregate at grain boundaries [53, 54]. In recent works, the main positive roles ascribed for Na in CIGS absorber layer has been the following: an increase in p-type conductivity of the PV device [51, 52, 55, 56], introducing acceptor defects [57], removing the compensating In_{Cu} donor defect [57],

increasing hole concentration from a typical value of 10^{14} cm^{-3} to approximately two orders of magnitude which results in an increase in the open circuit voltage (V_{OC}) and wiping detrimental defects out of grain boundaries [58, 59]. Employing enamelled steel substrate which release more K compared to Na has made a significant role in exploring the beneficial effect of K in device performance [4, 50, 60, 61]. PDT with KF uncovered the outstanding role of K in reducing recombination at the CdS/CIGSe interface and boosting the quality of the pn-junction [50, 62]. Also, PDT with KF results in a shorter deposition period for CdS, which give rise to the formation of a thinner buffer layer, meaning smaller amount of toxic Cd in the cells without a drop in the cell performance [50, 63]. In spite of positive effects, it was also reported that the presence of alkaline elements during the growth process (especially for absorber deposited at low temperatures) can lead to a deterioration of the PV performance [64]. Even though Na in low concentrations is benign, if Na impurities are present in high concentration during growth, it will severely harm the efficiency of the device [65]. Since CISe, CIGSe and CZTSe are structurally similar, exploring the effects of extrinsic defects such as Na and K in CZTSe may revolutionise our understanding of its performance and efficiency. This is why one of the questions which I address in this thesis is the theoretical investigation of the Na and K impurities in CZTSe.

Chapter 2

First Principles Calculations

2.1 Hartree-Fock Approximation

In this chapter I describe the theoretical background on which the calculations presented in this thesis rely. Fist the Hartree-Fock approximation is discussed shortly before the DFT theory and exchange-correlation functionals.

The Hartree-Fock (HF) approximation [66] is the successor of the Hartree method [67, 68]. In the Hartree method [67, 68], electrons are assumed as independent particles and the N-electron wave function can be expressed as direct product of single particle functions, known as Hartree product:

$$\chi_{HP}(r_1, r_2, ..., r_N) = \chi_1(r_1)\chi_2(r_2)...\chi_N(r_N), \tag{2.1}$$

where $\chi_i(r_i)$ denotes a single particle wave function and $\chi_{HP}(r_1, r_2, ..., r_N)$ stands for the many electron wave function. The main issue with the Hartree approximation is that it does not fulfill the Pauli antisymmetry principle [69]. According to the Pauli antisymmetry principle, the sign of the electronic wave function must change if space and spin coordinates of any two fermion particles are interchanged.

In the Hartree-Fock method, the exact wave function of the system containing N electrons is formed by combining single electron wave function in a way that satisfies the Pauli antisymmetry principle in a stationary state. This is done by defining the total

wave function as the determinant of a matrix of single electrons wave functions, called as Slater determinant:

$$\psi_{HF} = \sqrt{\frac{1}{N!}} \begin{vmatrix} \chi_1(x_1) & \chi_2(x_1) & ... & \chi_N(x_1) \\ \chi_1(x_2) & \chi_2(x_2) & ... & \chi_N(x_2) \\ . & . & . & . \\ . & . & . & . \\ . & . & . & . \\ \chi_1(x_N) & \chi_2(x_N) & ... & \chi_N(x_N) \end{vmatrix} \tag{2.2}$$

In the Hartree-Fock approach the electrons are indistinguishable, which means that the slater determinant satisfies the Pauli exclusion principle. The Slater determinant provides an exact electron exchange energy (energy reduction owing to antisymmetrization). There is, however, also another interaction between electrons. Namely, the correlation energy is the energy reduction term taking into account that electrons with unlike-spin also avoid each other [70]. The difference between HF energy and the true ground-state energy gives the correlation energy.

2.2 Density Functional Theory

Density Functional Theory (DFT) is one of the most capable approaches available in condensed-matter physics, computational physics, and computational chemistry. The goal of DFT is to describe via approximations the ground state of an interacting many electron system (in particular atoms, molecules, and condensed phases) in an external potential using the electron density n(r) as the fundamental variable instead of the one electron wave functions as in the HF theory.

If we consider a large number of electrons confined in a box, the Hamiltonian of our system is as follows:

$$\hat{H} = \hat{T} + \hat{V} + \hat{U}, \tag{2.3}$$

with the total energy of

$$E = T + V + U, \tag{2.4}$$

where

$$T \equiv \frac{1}{2}\int \bigtriangledown\psi^*(\mathbf{r}) \bigtriangledown \psi(\mathbf{r})d\mathbf{r} \tag{2.5}$$

$$V(r) \equiv \int v(\mathbf{r})\psi^*(\mathbf{r})\psi(\mathbf{r})d\mathbf{r} \tag{2.6}$$

$$U = \frac{1}{2}\int \frac{1}{|\mathbf{r}-\mathbf{r\prime}|}\psi^*(\mathbf{r})\psi^*(\mathbf{r\prime})\psi(\mathbf{r\prime})\psi(\mathbf{r})d\mathbf{r}d\mathbf{r}'. \tag{2.7}$$

$\psi(\mathbf{r})$ is the electronic wave function, T is the kinetic energy, $V(r)$ is the Coulomb interaction between electrons and nuclei and U is the electron-electron Coulomb interaction. The Hohenberg-Kohn theorem proves that by regarding the ground state density n_0(r), all the physical properties of the system, including the external potential ($V(\mathbf{r})$), can be determined. If we write the hamiltonian of the system as:

$$\hat{H} = \hat{T} + \hat{U} + \int v(\mathbf{r})\hat{n}(\mathbf{r})d^3(\mathbf{r}), \tag{2.8}$$

the $\hat{T}$ and $\hat{U}$ are called universal terms and $\hat{F} = \hat{T} + \hat{U}$, i. e. they apply to all electronic systems in their ground state.

2.3 Hohenberg-Kohn Theorems

The two Hohenberg-Kohn theorems applied by DFT are the following [71]:
1. The non degenerate ground-state (GS) wave function is a unique function of the GS density.

$$\psi_0(\mathbf{r}_1, \mathbf{r}_2, ..., \mathbf{r}_N) = \psi[n_0(\mathbf{r})]. \tag{2.9}$$

2. The exact ground state density minimises the total energy, and the GS energy has the variational property

$$E_v[n_0] \leq E_v[n'], \tag{2.10}$$

where n_0 is GS density in the potential V and n' is some other density. According to the second theorem, the expectation value of the Hamiltonian for any wave function ψ',

that is not its GS wave function is always greater than the GS energy,

$$E_v[\psi_0] = \langle\psi_0|\hat{H}|\psi_0\rangle \leq \langle\psi'|H'|\psi'\rangle = E_v[\psi']. \tag{2.11}$$

2.4 The Kohn-Sham Energy Functional

In 1965, Kohn and Sham (KS) proposed an expression for $\hat{F}$. The $\hat{F}[n]$ –known as the universal functional– has been splitted in such a way that only the so-called exchange-correlation energy functional, $E_{xc}[n]$, is approximated.

The idea behind the KS theory is that if an interacting particle system is replaced by a system of non-interacting quasi-particle, the external potential $v(\mathbf{r})$ for the interacting particle system could be reproduced in a system of non-interacting particles with the external potential $v_s(\mathbf{r})$ [72], and the suitable expressions for $T[n]$ and $U[n]$ are

$$T[n] = T_s[n] + T_c[n] \tag{2.12}$$

and

$$U[n] = U_H[n] + U_x[n] + U_c[n]. \tag{2.13}$$

$T_s[n]$ is the kinetic energy of a non interacting system with density n, in terms of single-particle orbitals $\phi_i(\mathbf{r})$

$$T_s[n] = -\frac{\hbar^2}{2m}\sum_i^N \int d^3r \phi_i^*(\mathbf{r}) \bigtriangledown^2 \phi_i(\mathbf{r}), \tag{2.14}$$

for a system of non-interacting particles, the sum over individual kinetic energies, gives the total kinetic energy of this system. $T_c[n]$ represents the kinetic part of the correlation energy. By definition $T_c[n]$ provides the difference between the kinetic energy of an interacting system and the kinetic energy of a non interacting system $(T - T_s)$. $U_H[n]$ is the Hartree potential, which is the mean-field Coulomb interaction of a single electron

with the charge of all other electrons,

$$U_H[n] = \frac{1}{2}\int d^3r \int d^3r' \frac{n(\mathbf{r})n(\mathbf{r}')}{|\mathbf{r}-\mathbf{r}'|}. \tag{2.15}$$

$U_x[n]$, known as exchange energy, arises due to the Pauli principle. Now one can rewrite the exact energy functional of the system as

$$E[n] = T[n] + U[n] + V[n] = T_s[\phi_i[n]] + U_H[n] + E_{xc}[n] + V[n], \tag{2.16}$$

where by definition E_{xc} is

$$E_{xc} = (T - T_s) + (U - U_s). \tag{2.17}$$

Since the interaction terms are all included in the exchange-correlation energy (except E_{xc}), the other terms of Equation 2.16 can be calculated exactly. The corresponding Schrödinger equation for a KS system is:

$$[-\frac{1}{2m}\bigtriangledown^2 + u_H(n(\mathbf{r}')) + v_{ext}(\mathbf{r}) + v_{XC}(r)]\psi_i(\mathbf{r}) = \varepsilon_i\psi_i(\mathbf{r}), \tag{2.18}$$

$$n(r) = \sum_{i=1}^{N}|\psi_i(\mathbf{r})|^2. \tag{2.19}$$

The above equation can be solved self consistently in several iterations (the explanation comes in Section 2.10). In principle, by solving the Kohn-Sham equation, we do not need empirical data from experimental results. This is why DFT calculation are also known as *ab initio* or first-principle calculation. To solve the Kohn-Sham equation computationally, the following parameters should be defined: a suitable approximation for exchange-correlation energy, a suitable basis set, an appropriate pseudo-potential, mesh for k-point sampling of the Brillouin zone of a solid, and the atomic structure of the unit-cell for the given crystal. These aspects are discussed in the following sections.

2.5 Exchange-Correlation Functionals

Local Density Approximation

The exchange correlation energy in Equation 2.16 can not be evaluated exactly and we need an approximation for the E_{XC} functional. The local density approximation (LDA) [73] was the first approximation that has been used. In this approximation one assumes that for regions of a material where the charge density of the system varies slowly, the exchange correlation energy per electron $\epsilon_{XC}(r)$ at that region is equal to the exchange correlation energy of a homogeneous electron gas with the same density. In this approximation the exchange-correlation energy is given by

$$E_{XC}^{LDA}[\rho] = \int \rho(\mathbf{r})\epsilon_{XC}^{hom}(\rho)\, d(\mathbf{r}), \tag{2.20}$$

where $\epsilon_{XC}^{hom}(\rho)$ is the exchange correlation energy of a homogeneous electron gas with the same density of ρ.

To include electron spin in the approximation, LDA is generalized as local spin-density approximation (LSD) [74]

$$E_{XC}^{LDA}[\rho\uparrow, \rho\downarrow] = \int \rho(\mathbf{r})\epsilon_{XC}^{hom}(\rho\uparrow, \rho\downarrow)\, d(\mathbf{r}). \tag{2.21}$$

The $\epsilon_{XC}^{hom}(\rho)$ is a well established parameter, and as a result, there is only one LDA approximation.

Generalized Gradient Approximation

The so-called Generalized Gradient Approximation (GGA), which has been improved upon the local spin density (LSD) approximates the energy of the true density by including the energy of the gradient of the electron density. Where $\rho = \rho\uparrow + \rho\downarrow$

$$E_{XC}^{GGA}[\rho\uparrow, \rho\downarrow] = \int d(\mathbf{r}) f(\rho\uparrow, \rho\downarrow, \bigtriangledown\rho\uparrow, \bigtriangledown\rho\downarrow). \tag{2.22}$$

The most preferred choice for $f(\rho\uparrow, \rho\downarrow, \bigtriangledown\rho\uparrow, \bigtriangledown\rho\downarrow)$ is still a matter of debate and there are several different parametrizations of the GGA, each resulting in different energies for the same system. The construction of some GGA functionals starts from the uniform electron gas, and some are semi-empirical functionals, which contain one or more parameters fitted to a particular finite system.

Although GGA can yield highly successful results for small molecules, it is often not as predictive for systems with strongly correlated electrons or in systems with delocalized electrons such as simple metals [when $f(\rho\uparrow, \rho\downarrow, 0, 0) \neq \rho(\mathbf{r})\epsilon_{XC}^{hom}(\rho\uparrow, \rho\downarrow)$]. A first-principles numerical GGA can be formulated by setting the second-order density-gradient expansion for the exchange-correlation hole neighbouring the electron in a system where the density alters slowly, then, to satisfy sum rules on the exact hole, its long-range parts is cut-off. In 1991, Perdew and Wang presented a functional known as PW91 [75] to fit this numerical GGA analytically. Afterwards, in 1996, Perdew, Burke, and Ernzerhof (PBE) [76] proposed the formalism for a simplified GGA for exchange and correlation, in which all parameters (other than those in LSD) are basically constant. In general, independent of the model used for the hole (for example PW91), the PBE functional is numerically compatible to PW91 [76].

Hybrid Functionals

One of the stat-of-the-art methods to calculate the XC energy for semiconductors and strongly correlated systems to mitigate the shortcomings of GGA mentioned above is using hybrid functionals [77, 78]. Hybrid functionals are a class of approximations applied to calculate the exchange-correlation energy, which are not pure DFT functionals. The basic idea behind the hybrid functionals is to mix Hartree-Fock exchange energies with those obtained from DFT methods in order to improve the calculations. The simplest form for such a hybrid functional can be written as:

$$E_{XC} = \alpha\, E_X^{HF} + (1-\alpha)\, E_X^{PBE} + E_C^{PBE}. \tag{2.23}$$

The parameter α controls the amount of Hartree-Fock exchange in our hybrid functional calculations, and can be fitted empirically or estimated theoretically. The mixing coefficient α is not equal to or close to 1, since the full exact exchange is not compatible with E_C^{PBE}. The motivation for constructing hybrid functions arises from the fact that combining the DFT and HF functionals one can compensate for their deficiencies. For example, DFT underestimates the band gaps of semiconductors and HF overestimates band gaps, however by applying the hybrid functionals, DFT and HF functionals act complementarily and the predicted band gap is much more accurate. Furthermore, the calculated total energies and system geometries are also more accurate.

2.6 Plane-Wave Basis Sets and Bloch Theorem

By definition, a plane-wave is a constant-frequency wave whose wave fronts consists of infinite parallel planes with a constant amplitude. Although the requisite of having a perfect plane-wave is its propagation to infinite extent, but, many waves are locally considered as plane-waves. The general form for representing a plane-wave is given as:

$$P(\mathbf{r}, t) = P_0 \, e^{i(\mathbf{k}.\mathbf{r} - wt)}, \tag{2.24}$$

where $\mathbf{k}$ is the wave vector inside the first Brillouin zone of the reciprocal lattice, $\mathbf{r}$ is the position vector and w is the wave's angular frequency.
Bloch's theorem states that in a periodically-repeating solid, the wavefunction of an electron assumes the following form [79, 80]:

$$\psi_i(\mathbf{r}) = exp[i\mathbf{k}.\mathbf{r}] \; u_i(\mathbf{r}), \tag{2.25}$$

which is a product of a periodic function, $u_i(\mathbf{r})$, and a plane-wave, $exp[i\mathbf{k}.\mathbf{r}]$. The periodic function can be expanded as:

$$u_i(\mathbf{r}) = \sum_G \; c_{i,G} \; exp[i\mathbf{G}.\mathbf{r}], \tag{2.26}$$

where **G** is the reciprocal lattice vector and is defined by $G.R = 2\pi m$, **R** is the Bravais lattice vector and **m** is an integer. So, each electronic wavefunction can be written as a sum over plane-waves

$$\psi_i(\mathbf{r}) = \sum_G c_{i,k+G}\ exp[i(\mathbf{K}+\mathbf{G}).\mathbf{r}]. \tag{2.27}$$

The Kohn-Sham potential is defined as

$$V_{KS}(\mathbf{r}) \ = \ V_{ext}(\mathbf{r}) + V_H(\mathbf{r}) + V_{xc}(\mathbf{r}). \tag{2.28}$$

In a solid this potential is periodic with the same periodicity as the bravais lattice vector, **R**, so one can write it as:

$$V_{KS}(\mathbf{r}+\mathbf{R}) \ = \ V_{KS}(\mathbf{r}). \tag{2.29}$$

Hence, one can apply the Bloch's theorem and express the KS eigenfunctions of the periodic crystalline solid system as:

$$\psi_k^n(\mathbf{r}) \ = \ (\sum_{\mathbf{G}} \psi_k^n(\mathbf{G})\, e^{i\mathbf{G}\mathbf{r}})\, e^{i\mathbf{k}\mathbf{r}}, \tag{2.30}$$

where the eigenfunctions $\psi_k^n(\mathbf{r})$ are indexed by a vector **k** in the first Brillouin zone and n stands for the band number. The vector **G** corresponds to all the reciprocal lattice vectors and $\psi_k^n(\mathbf{G})$ are the wave function components in the reciprocal space. For computational purposes, this sum is truncated to the plane-waves for which the kinetic energy is lower than a certain cut-off energy, E_{cut}

$$\frac{\hbar^2}{2m}|\mathbf{k}+\mathbf{G}|^2 \ \leq \ E_{cut}. \tag{2.31}$$

The cut-off energy is one of the crucial factors that controls the precision of our computational calculations. The precision can be systematically improved by increasing the cut-off energy, but the calculation gets computationally more expensive. The number

of plane-waves for a specified cut-off energy depends upon the selected k-point mesh. In the center of the BZ the number of plane-waves has the following relationship to the cut-off energy:

$$N_{pw} = \frac{4\pi}{3\Omega_{BZ}}(E_{cut})^{\frac{3}{2}}, \tag{2.32}$$

where Ω_{BZ} is the volume of our BZ. In agreement with above equation, the number of plane-waves scales as $E_{cut}^{\frac{3}{2}}$.

2.7 Pseudo-Potential

Hans Hellmann introduced the concept of pseudo-potential approximation in 1934 [81]. In the framework of the pseudo-potential approximation only the chemically active valence electrons are dealt with explicitly in the Schrödinger equation and the effect of the non-valence electrons (called frozen electrons) and also the nuclei are substituted by an effective potential, called pseudo-potential. Hence, in the Schrödinger equation, instead of the Coulomb interaction term for core electrons and the nuclei, the pseudo-potential is used. Pseudo-potentials make plane-wave basis sets practical to use for computational calculations [82]. Since the core orbitals are bounded very tightly, and also to maintain the orthogonality between the core wave functions and the valence wave functions, the wave function of the valence electrons oscillate rapidly in the core electron region. Therefore, a very large number of plane-waves must be used for an all-electron calculation, which makes such calculations prohibitively expensive from the standpoint of the computational resources. By taking advantage of the pseudo-potential approximation, a much smaller number of plane-wave basis sets can represent the electronic wave function of the system. Consequently, pseudo-potentials are a strongly relevant factor in the plane-wave method.

2.8 Brillouin Zone Sampling

To determine the electronic charge state $n(r)$ from Equation 2.19 applied for a periodic system, one has to perform an integration over the Brillouin zone. For this purpose, the

wave function and their corresponding energies at certain points of the first Brillouin zone are calculated. Points in the reciprocal space grid generated for the BZ integration are usually connected to each other by symmetry operations. The smallest portion of the Brillouin zone (BZ) which can reproduce the BZ via symmetry operations is referred as the irreducible BZ. Using these operations reduces the number of points that are used in the BZ integration, and consequently the computational effort. In this thesis for the investigation of solar cell materials I have used a uniform grid based on the Monkhorst-Pack scheme [83]. In addition to symmetry, for choosing appropriate k-points we need to consider the uniformity of the BZ too. As discussed by Moreno and Soler [84], mesh points that are evenly distributed are preferred over those that have different densities in different dimensions. Furthermore, displacing the mesh origin from the Γ point is a common way to reduce the number of inequivalent mesh points.

2.9 Unit-Cell

The notion of the unit cell is a basic underlying concept for the description and characterization of crystal structures. By definition, the smallest unit of volume, consisting of atoms which has the overall symmetry of a crystal is called the primitive unit cell. By repeating the unit cell in three dimensions, the bulk arrangement of the crystal can be built. In the early 19th century, the work of Auguste Bravais revealed that there are only seven crystal systems, which tell us how the atoms are arranged within the unit cell. Thus, many different crystals share the same unit cell type. One of the most important characteristics of a unit cell is the number of atoms which it contains and the total number of atoms in the entire crystal equals the number of unit cells multiplied by the number of atoms each unit cell contains.

The simulation of large extended crystals can be often dramatically simplified by using a simple unit cell containing only a few atoms and three dimensional periodic boundary conditions, where the unit cell is periodically repeated in the three spatial dimensions.

2.10 Self-Consistency Loop

In order to determine the ground state energy of solids, we need to diagonalize the KS Hamiltonian iteratively in conjunction with an iterative improvement of the charge density. Figure 2.1 shows a typical flowchart diagram for the steps involved in a density functional self-consistent loop.

In the first step, an initial charge density ρ_{in} and a set of trial wave functions ψ_i is chosen. This initial charge density corresponds to the superposition of the atomic pseudo charge densities of each atomic site present in the unit cell. Using this initial density, the total Hamiltonian of the solid can be build, which encompasses the Hartree potential $V_H[\rho_{in}(r)]$, exchange correlation potential $V_{xc}[\rho_{in}(r)]$ and ionic potential $V_{ion}(r)$. Next, the Hamiltonian

$$[-\frac{\hbar^2}{2m} \bigtriangledown^2 + V_{eff}(\rho(r), r)]\psi_i(\mathbf{r}) = \varepsilon_i \psi_i(\mathbf{r}), \tag{2.33}$$

is being diagonalized in order to compute the energies. After diagonalizing the Hamiltonian, a new charge density, $\rho_{out}(r)$ can be computed, where

$$\rho_{out}(r) = \Sigma_i |\psi_i(r)|^2. \tag{2.34}$$

To get the Kohn-Sham ground state energy self consistently, the difference between ρ_{out} and ρ_{in} should be zero. After reaching consistency, the cycle stops and all other desired quantities such as total energy, band structure, density of states, etc. can be computed. However if the output density, $\rho_{out}(r)$, does not equal the starting density, ρ_{in}, a new ρ_{in} will be generated and a new another self consistent cycles starts. In practice, one allows for a small difference between ρ_{out} and ρ_{in}, and once the change is smaller than this convergence criteria, one assumes that the self-consistency have been reached.

2.11 Formation Energy Calculation

One of the many applications of the theoretical methods described above is the calculation of defect formation energies. This parameter has a great importance in the

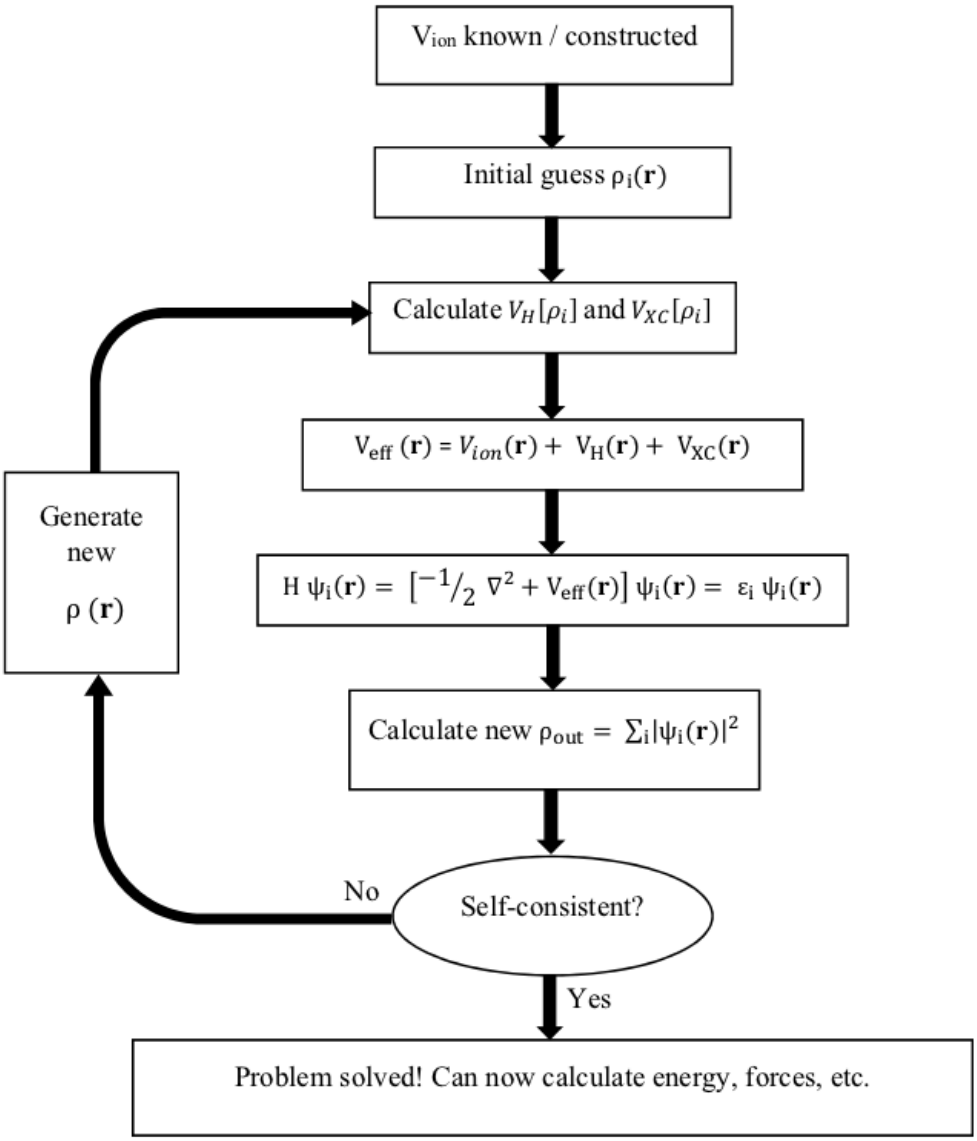

Figure 2.1: Schematic flow chart of a self consistent algorithm for a density functional based calculation.

framework of this thesis, therefore, a detailed description is given in the following paragraphs.

Supercell calculation is the most prevalent procedure to calculate the formation energy of impurities in bulk materials. In this method a defect α with charge state q is surrounded by a finite number of atoms of the bulk compound, and the whole structure is repeated periodically [85]. The dimension of the supercell has to be rather large to reduce the spurious interactions between the defect and its own periodic replicas [26, 47]. The formation energy of a charge neutral defect or impurity α is defined as

$$E_f[\alpha^q] = E_{tot}[\alpha^0] - E_{tot}[\text{pure}] - \Sigma_i n_i \mu_i, \tag{2.35}$$

where $E_{tot}[\alpha^0]$ is the total energy of the supercell with the defect α and $E_{tot}[\text{pure}]$ is the total energy of the equivalent defect-free bulk supercell. n_i represents the number of atoms of type i that have been added to or removed from the bulk supercell to create defects, and μ_i is the associated chemical potential. When the defects are charge neutral, the interactions between neighbouring defects converge quickly with the size of supercell and the obtained value for the formation energy of isolated defects is quite reliable even for small supercell calculations. This is not the case for cells containing charged defects.

2.12 Charge Correction Error

For charged supercells, the computational conditions are more complex for a multitude of reasons [86]. Namely, the periodically repeated defect system effectively consists of a uniform neutralizing background charge. This background charge ensures that the electronic energy per unit cell stays finite. Since the charge of the defect system does not match that of the neutral supercell, a chemical potential for the electrons has be added to the Equation 2.35 to take this contribution into account. As a result, for a

charged supercell the formation energy is defined as

$$E_f[\alpha^q] = E_{tot}[\alpha^q] - E_{tot}[\text{pure}] + E^q_{corr} - \Sigma_i n_i \mu_i + q[E_{VBM} + \mu_e + \Delta v_{0/b}], \quad (2.36)$$

where q is the charge state of the defect, E_{VBM} is the valence band maximum of the defect-free bulk and μ_e is the chemical potential of the electrons. Due to the finite-size of the supercells the formation energies need to be corrected. To do so, first the total energy is being corrected by a potential alignment term, $q\Delta v_{0/b}$. Next, the total energy is corrected by E^q_{corr} that accounts for the interaction of the charged defect with its periodic replicas (image-charge correction). $\Delta v_{0/b}$ is the difference between the average electrostatic potential of the bulk and the supercell containing the associated neutral defect, and it is most straightforward for determine this term based on calculations performed on neutral defects [86]. The $\Delta v_{0/b}$ parameter can be either determined as the difference between local potentials via the averaging over transversal planes (planar-average method) or via averaging over the core zones surrounding the nuclei (core-average method).

The correction term E^q_{corr} in Equation 2.36, that stands for the finite-size supercell correction can be obtained through several schemes. In this thesis we applied the approach proposed by Lany and Zunger (LZ) [87]. E^q_{corr} in the scheme of LZ is obtained by considering the charge density difference between the charged and the neutral supercells through DFT calculations, which is expressed as

$$E^{LZ}_{corr} = [\ 1\ -\ c_{sh}\ (\ 1 - \frac{1}{\varepsilon}\ )]\ \frac{q^2\alpha}{2\varepsilon L}, \quad (2.37)$$

where ε is dielectric constant of the bulk, L is the cubic root of the supercell volume and the term c_{sh} treats the adopted cell shape. According to LZ, both image-charge interaction and potential-alignment effects must be corrected simultaneously.

Chapter 3

The Theory of Diffusion

3.1 Fick's Laws

Defects and impurities which are present in a crystal do not remain still. They exchange their sites with lattice atoms, jump in between them, and diffuse around the crystal lattice constantly. Defect diffusion leads to a redistribution of defects and also mediating the mass transport of the constituent atoms. The presence of different types of defects gives rise to different diffusion mechanisms. Substitutionally dissolved defects diffuse by the same point-defect mechanism as self diffusion. Such a movement or jump of the interstitial atom leads to a significant distortion of the lattice, and this mechanism is more likely to take place when the interstitial atom is smaller than the atoms on the lattice positions of the bulk material. Vacancies and interstitial defects are also mobile defects that mediate self-diffusion [88].

Fick's first law assumes that in a steady state, the flux moves from a high concentration region to a low concentration region. In one dimension the law can be written as:

$$J = -D\frac{\partial \phi}{\partial x}, \tag{3.1}$$

where J is the diffusion flux, ϕ is the concentration in dimension of (mol m^{-3}) and D is a mathematical function which relates the concentration of a specific species with the flux at a specific temperature and is called the diffusion coefficient. Since there

are several different diffusion mechanisms corresponding to the transport of vacancies, interstitial and substitutional atoms, the total diffusion coefficient equals to the sum of these contributions:

$$D_{total} = D_{Vacancy} + D_{Interstitial} + D_{Substitutional}. \tag{3.2}$$

The diffusion coefficient is a product of the defect concentration, C_x, and defect diffusivity, d_x, so

$$D_{total} = \Sigma_x(\frac{n_x}{N})d_x, \tag{3.3}$$

where x refers to different diffusion mechanisms and

$$d_x = D_0^x exp(\frac{-E_m}{K_B T}). \tag{3.4}$$

In the equation above the constant D_0^x is the product of temperature independent terms for a given process and E_m is the enthalpy difference between the initial state and the saddle point along the diffusion path. Defect concentration is proportional to $exp\frac{-E_f}{K_B T}$, where E_f is the formation energy of the defect and by using the following equation in thermal equilibrium, $E_a = E_m + E_f$, (in case of non equilibrium conditions $E_a = E_m$), we obtain the equation below for the diffusion coefficient:

$$D = D_0^x exp\frac{-E_m}{K_B T} exp\frac{-E_f}{K_B T} = D_0^x exp\frac{-E_a}{K_B T}. \tag{3.5}$$

The above equation is called Arrhenius equation [89], where E_a is the overall activation energy for the given process, K_B is the universal gas constant or Boltzmann constant and T is the temperature. For instance, an interstitial-mediated diffusion occurs when an ion moves from one interstitial site to a neighbouring interstitial site, overcoming the migration enthalpy, E_m. For interstitial contribution to the diffusion coefficient, we

have

$$D_I \sim exp\frac{-E_a}{K_B T}. \tag{3.6}$$

Fick's second law assumes that D is a constant, which holds true only for highly diluted liquid solutions. By combining the continuity equation of mass transport

$$\frac{d\phi}{dt} = -\frac{\partial J}{\partial x} \tag{3.7}$$

and Fick's first law, Fick's second law can be derived as

$$\frac{d\phi}{dt} = \frac{\partial}{\partial x}(D\frac{\partial \phi}{\partial x}) = D\frac{\partial^2 \phi}{\partial x^2}. \tag{3.8}$$

Fick's second law of diffusion describes the velocity of accumulation (or depletion) of concentration inside a volume as proportional to the second derivative of the local concentration to tell us the rate at which concentration is changing at any given point in space. Assuming that we know the diffusion coefficient, this formula allows us to determine how much time is needed (on average) for particles being transported by diffusion to travel across a particular distance.

3.2 Transition State Theory

3.2.1 A Brief Introduction to Transition State Theory

Transition state theory (TST) also known as "absolute rate theory" or "activated-complex theory" is base on a hypothetical quasi-equilibrium transitional state that exists between initial state (reactant) and final state (product) during a chemical reaction. Figure 3.1 depicts a reactant, product and a transition state along a hypothetical reaction coordinate, also referred as reaction path. TST has been formulated by Wigner, Eyring, Polanyi and Evans in the 1930s [90–93]. Before TST, the Arrhenius equation was employed for explaining the rate of a chemical reaction. However, this equation

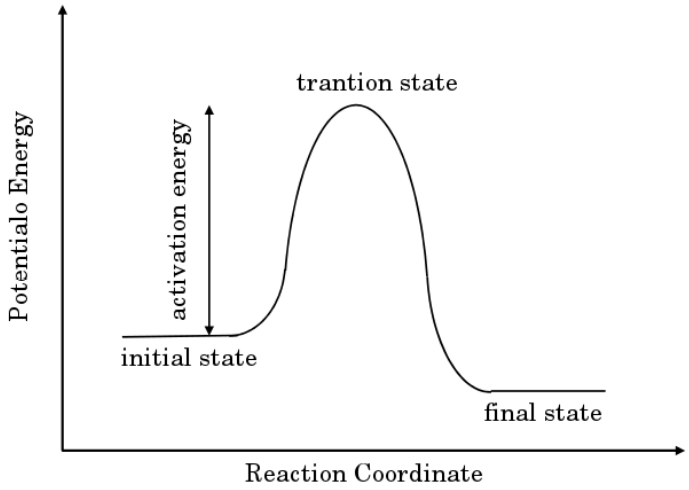

Figure 3.1: A diagram of the reaction coordinate.

can be used only for gas-phase kinetics and since the equation was derived empirically based on experimental findings, the theoretical basis for the pre-exponential factor (D_0) and activation energy was not understood.

According to TST, there is a quasi-equilibrium state between the reactant state and the product state, called transition state. In the transition state, the reactants are joined to a species known as activated complex. The theory presents three basic concepts concerning the activated complex:

1. The activated complexes are in an equilibrium condition with the reactant molecules, even when the reactants and products are not in equilibrium with each other.

2. The reaction rate can be investigated through examining the activated complexes.

3. The activated complexes can break apart either leading back to the the reactants or to form the product.

3.2.2 Assumptions and Limitations of TST

Besides the Born-Oppenheimer (adiabatic) approximation, which is implicit in the use of potential energy surfaces (will be explained in the next section), three additional major assumptions are involved in TST [94]. Although the theory is extensively applicable, each of these three assumption introduce some limitations to it.

According to the first assumption, the atomic nuclei act in accordance with classical mechanics. As a consequence, the reaction will take place only if the atoms and molecules run into each other with enough energy for forming the transition state, otherwise the reaction does not take place. However according to quantum mechanics, even if the particles do not have enough energy for overcoming the energy barrier, there is a possibility of tunnelling across the barrier. So, regarding the laws of the quantum mechanics, even if the particles do not collide with sufficient energy to get over the energy barrier, there is still a chance that reaction will occur leading to a product or multiple products. Since the chance of tunnelling is elevated by lowering the barrier height, this assumption makes a substantial limitation for reactions with comparatively low energy barriers. TST is also based on the assumption that each intermediate state lasts long enough in order to reach the Boltzmann distribution of energies before moving towards the next step. Hence, the TST can provide inaccurate results for states involving short duration.

In the third assumption, the TST premises that for any activated complex that crosses the potential energy barrier the formation of product is inevitable and the activated complex will certainly persist on creating the products of the reaction. However, in a real system some trajectories may get back to the reactant side and traverse the barrier several times.

3.3 Potential Energy Surface

Potential energy surface (PES) is a basic concept in computational chemistry which describes the energy of a system (collection of atoms) in terms of their geometrical parameters like the position of atoms, the bond length and the angle between bonds. If q stands for the geometric parameter of the system, then mathematically a stationary point in PES is the point in which the first derivative of the potential energy with respect to each geometry parameter is zero (each derivative is with respect to only one

geometric variable q of which E is a function):

$$\frac{\partial E}{\partial q_1} = \frac{\partial E}{\partial q_2} = ... = 0. \tag{3.9}$$

The reactant and product structures which represent quasi-stable systems are minimas of the PES and any little transfiguration in the geometry of the system leads to an increases in the energy of the system. Thus, for a minima on the PES, for all q as shown in Fig 3.2 (a)

$$\frac{\partial^2 E}{\partial q^2} > 0 \tag{3.10}$$

Another kind of stationary point on the PES is called a saddle point. A saddle point is

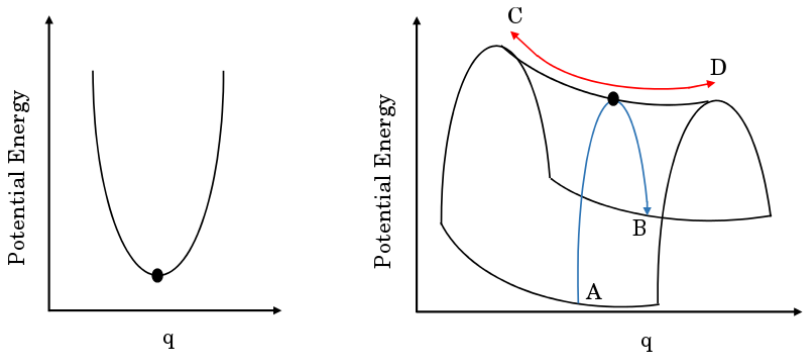

Figure 3.2: The left figure shows a minimum in PES and the right figure shows a transition state or saddle point in PES.

a maxima along the reaction coordinate and a minimum in all other directions. Traveling from one minima (reactant) to the other one (product) on the reaction coordinate requires enough energy (called activation energy) for traversing the maximum barrier (transition state or saddle point). As it is shown in Fig 3.2, along A-B direction, a maxima is placed, however along the C-D direction it corresponds to a minima. Hence, for a transition state or saddle point on the PES for all q excluding the reaction coordinate

$$\frac{\partial^2 E}{\partial q^2} > 0 \tag{3.11}$$

and along the reaction coordinate

$$\frac{\partial^2 E}{\partial q^2} < 0. \tag{3.12}$$

The path which links two minimas on the PES and shows the highest statistical weight is known as minimum energy path (MEP). Several methods have been presented for finding MEP between the reactant and the product structure [95–97]. Some of these methods map out a path with a starting point at a local minimum on the PES and then walk along the PES step by step to find a path of slowest ascent [98–102]. The other types fall downhill from transition state toward energy minima through the steepest descent pathway [103–107]. In this scheme the TS is first optimised and then pathways from TS to the initial and final structures are defined. To avoid the calculation of TS before having onformation on the MEP, a new scheme called chain-of-states method has been developed. In this method reactant and product structures which are minimas on PES are connected with a number of images (also referred as replicas, or states) which are optimized simultaneously while keeping the endpoints fixed. In order to have a smooth propagation of images the distance between neighbouring images must be held equidistant. To achieve this purpose some constraints are applied between them [108–112]. In the following sections we will focus on such chain-of-states methods.

3.4 Plain Elastic Band (PEB) Method

In the framework of the so called chain-of-state methods, several images are linked together in order to span a path between an initial and a final state. To find a the MEP via the plain elastic band (PEB) method [113], first of all an initial guess for the transition path is simply constructed by a linear interpolation between reactant and product configurations in the Cartesian coordinate space. Therefore, the intermediate images will be defined by a set of coordinates as

$$\mathbf{R}_i = \mathbf{R}_0 + i\Delta\mathbf{R}, \quad \Delta\mathbf{R} = \frac{\mathbf{R}_0 - \mathbf{R}_{n+1}}{n+1}, \tag{3.13}$$

where $\mathbf{R}_i$ is the position vector of image number i, $\mathbf{R}_0$ is the position vector of reactant structure, n is the number of intervals which goes from 1 to i and $\mathbf{R}_{n+1}$ is the position vector of the product structure. By introducing a harmonic spring force between neighbouring images, the collapse of the midway images can be prevented. As a result, the atoms from intermediate image i are connected with their neighbouring intermediate images $i-1$ and $i+1$. For such a system the object function can be defined as

$$S(\mathbf{R}_1, \mathbf{R}_2, ..., \mathbf{R}_n) = \sum_{i=0}^{n+1} + \sum_{i=1}^{n+1} \frac{nk}{2} (\mathbf{R}_i - \mathbf{R}_{i-1})^2, \tag{3.14}$$

where $E(\mathbf{R}_i)$ is the energy of the system at image i with atomic positions $\mathbf{R}_i$ and k is the spring constant. In order to find the MEP, the reactant and product configurations should be held fixed and the object function should be minimized with respect to the nuclear coordinates in all replicas $\mathbf{R}_i$. There are two force components acting on the images: the spring force which is defined as

$$\mathbf{F}_i^S \equiv k_i(\mathbf{R}_{i+1} - \mathbf{R}_i) - k_i(\mathbf{R}_i - \mathbf{R}_{i-1}) \tag{3.15}$$

and the true force ($\mathbf{F}_i^t$), which is the gradient of the energy with respect to the atomic positions at the i-th image: $\mathbf{F}_i^t = -\nabla E(\mathbf{R}_i)$.

In consequence, the forces acting on the i-th image in elastic band method can be written as: $\mathbf{F}_i^{EB} = \mathbf{F}_i^t + \mathbf{F}_i^s$. From the perspective of the accuracy of the chain of states methods, the PEB method has a major flaw, because it is not able to locate the TS exactly. In fact, the plain elastic band method can not discover the position of TS even for a very large number of intermediate images, except when i goes to infinity, which is of course computationally not feasible. The two shortcomings of the plain elastic band are described in the following:

1. The images slip down on the PES towards the initial and final minimas, i. e. reatant and product states. As a result there is no high energy image available near the TS, so the resolution of the path is reduced in the most important region of the path and the activation energy will be underestimated. This problem could be solved by increasing

the stiffness of the springs. However, by considerably increasing the spring constant it leads to the so called corner cutting, described below.

2. Since the pathway is not continuous, by increasing k, the path will spuriously bend in the vicinity of TS region and cuts the corners. As a result of the stiffer springs, the path will prefer to go over the high energy parts of PES rather than following the MEP. Because of this the potential energy of the images increases, and the barrier will be severely overestimated.

As a conclusion to the discussion from above, one can not set a perfect k, which corrects the sliding of replicas toward minimas and at the same time prevents corner-cutting. Furthermore, a large number of intermediate images is needed in order to have a good estimation for the TS, which is computationally very expensive for real life systems, especially when one uses hybrid functionals. Because of these two shortcomings of the PEB method, this scheme is outdated and it has been replaced by the so called Nudged Elastic Band (NEB) method, which will be presented in the following section.

3.5 Nudged Elastic Band (NEB) Method

The NEB method is employed for finding the minimum energy path in a chemical reaction and estimating the activation barrier, in which the shortcomings of the PEB method is solved through a force projection scheme. A local tangent to the path at replica i, which is connected to the neighboring $i-1$ and $i+1$ replicas in the chain is constructed as:

$$\tau_i = \frac{\mathbf{R}_i - \mathbf{R}_{i-1}}{|\mathbf{R}_i - \mathbf{R}_{i-1}|} + \frac{\mathbf{R}_{i+1} - \mathbf{R}_i}{|\mathbf{R}_{i+1} - \mathbf{R}_i|}. \tag{3.16}$$

The local tangents τ_i are updated after every M steps (where M is on the order of 10) in the optimization [114], where after every optimization step new forces and energies are calculated based on the new R positions. After applying the τ_i local tangents of the path, the spring forces and true forces are projected into the parallel and perpendicular components according to the τ_i:

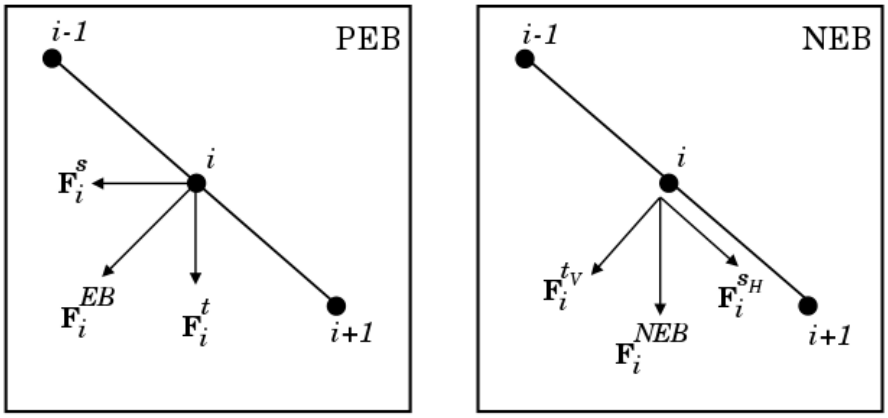

Figure 3.3: The forces acting on the images in plain elastic band (PEB) model and nudged elastic band (NEB) method are illustrated in the left and right panels of the figure, respectively. In NEB method, the $F_i^{t_V}$ and $F_i^{s_H}$ correspond to the vertical component of the true force and horizontal component of the spring force respectively. The i, $i-1$ and $i+1$ stand for the index of the images.

$$\mathbf{F}_i^t = \mathbf{F}_i^{t\parallel} + \mathbf{F}_i^{t\perp}; \quad \mathbf{F}_i^s = \mathbf{F}_i^{s\parallel} + \mathbf{F}_i^{s\perp}. \tag{3.17}$$

The corner cutting problem affecting the PEB method comes from the perpendicular component of the spring force ($\mathbf{F}_i^{s\perp}$) which tends to pull the replicas off the MEP (up on the PES) by straightening the path. On the other hand, the component of the true force which is in the direction of the path ($\mathbf{F}_i^{t\parallel}$) tries to pull the images down toward the two endpoints which causes the problem of the images sliding down. In NEB method, an elastic band is minimized by excluding the perpendicular component of the spring force and the parallel component of the true force. Thus, the forces on each intermediate image i can be written as

$$\mathbf{F}_i^{NEB} = \mathbf{F}_i^{t\perp} + \mathbf{F}_i^{s\parallel} \tag{3.18}$$

in which

$$\begin{aligned} \mathbf{F}_i^{t\perp} &= -\nabla E(\mathbf{R}_i) + \nabla E(\mathbf{R}_i).\hat{\tau}_i\hat{\tau}_i, \\ \mathbf{F}_i^{s\parallel} &= k(|\mathbf{R}_{i+1} - \mathbf{R}_i)| - |\mathbf{R}_i - \mathbf{R}_{i-1}|)\hat{\tau}_i. \end{aligned} \tag{3.19}$$

In the above equations the unit vector $\hat{\tau}_i$ is the normalized local tangent at image i defined as: $\hat{\tau}_i = \frac{\tau_i}{|\tau_i|}$. Due to the force projection, the spring force only takes care of establishing an even distribution of images along the path and does not interfere with $\mathbf{F}_i^{t\perp}$ in the off-path track. So, the k value can be increased without causing corner-cutting. This projection of $\mathbf{F}_i^{t\perp}$ and $\mathbf{F}_i^{s\parallel}$ components has been referred as nudging of the elastic band [115].

3.6 CI-NEB Method

In a calculation where the MEP is being evaluated with the NEB method, most often the number of images is limited in comparison with the length of the MEP. Thus, only few images are available in the vicinity of the saddle point and consequently, the TS obtained via the NEB can be inexact. Thus, even the NEB method is not able to find the saddle point for asymmetric reactions, or for symmetric reactions using even number of intermediate images i. The climbing image NEB (CI-NEB) method is a modification to NEB, which is able to locate the position of the saddle point more accurately [116]. In CI-NEB method a precise convergence to the saddle point is obtained by taking the image with energy resulted from NEB method and acting the following force on it:

$$\begin{aligned} \mathbf{F}_{i_{max}} &= -\nabla E(\mathbf{R}_{i_{max}}) + 2\nabla E(\mathbf{R}_{i_{max}})|_{\parallel} \\ &= -\nabla E(\mathbf{R}_{i_{max}}) + 2\nabla E(\mathbf{R}_{i_{max}}).\hat{\tau_{i_max}}\hat{\tau_{i_max}}. \end{aligned} \tag{3.20}$$

This way the shape of the MEP is maintained and since all images are being optimized simultaneously at every force iteration M, no additional effort is needed to turn the image with the highest energy on the PES into a climbing image. As it is clear from equation 3.20, in CI-NEB modification the climbing image is not influenced by the spring forces and therefore the distances between the intermediate images located on the two sides of the peak in the vicinity of the TS can be different from each other. Accordingly, while the images on one side of the highest energy repplica start to compress, the images on the other side can spread out. In this thesis the CI-NEB scheme has been applied

for finding the transition state, and calculating the activation barrier.

Chapter 4

Results and Discussions

The results of this chapter are based on the following publications:

1. Elaheh Ghorbani, Janos Kiss, Hossein Mirhosseini, Guido Roma, Markus Schmidt, Johannes Windeln, Thomas D. Kühne and Claudia Felser.
Hybrid-Functional Calculations on the Incorporation of Na and K Impurities into the $CuInSe_2$ and $CuIn_5Se_8$ Solar-Cell Materials
J. Phys. Chem. C. **119**, 25197 (2015)

2. Elaheh Ghorbani, Hossein Mirhosseini, Janos Kiss, Thomas D. Kühne and Claudia Felser.
Hybrid Functional Calculations on the Incorporation of Na and K Impurities in Substitutional and Interstitial Positions in $Cu_2ZnSnSe_4$
Proc. 42nd IEEE Photovoltaic Specialists Conf.

3. Elaheh Ghorbani, Hossein Mirhosseini, Janos Kiss and Claudia Felser.
Incorporation of Li dopant into $Cu_2ZnSnSe_4$ photovoltaic absorber: hybrid-functional calculations
J. Phys. D: Appl. Phys. **48**, 482001 (2015)

4. Elaheh Ghorbani, Hossein Mirhosseini, Janos Kiss, Thomas D. Kühne and Claudia Felser.

Hybrid Functional Investigations of the Incorporation of Sodium and Potassium in $CuInSe_2$ and $Cu_2ZnSnSe_4$

Proc. 31th EU-PVSEC Conf. 3DV.1.56, 1271 (2015)

5. Elaheh Ghorbani, Janos Kiss, Hossein Mirhosseini, Guido Roma, Markus Schmidt, Johannes Windeln, Thomas D. Kühne and Claudia Felser.

Insights into Intrinsic Defects and the Incorporation of Na and K in the $Cu_2ZnSnSe_4$ Thin-Film Solar Cell Material from Hybrid-Functional Calculations

J. Phys. Chem. C., **120**, 2064, (2016)

4.1 Background and Scope

The global energy demand is constantly on the rise [117]. If renewable-energy resources like solar cells are to make a significant contribution to this growing demand, they should be able to produce energy in the terawatt scale. Cu(In,Ga)Se_2 (CIGSe) consisting of $CuInSe_2$ and $CuGaSe_2$ is widely used as light absorber layer in efficient and inexpensive thin film solar cells, which have produced maximum conversion efficiencies of up to 21.7 % [118, 119].

Solar cell devices based on CIGSe are manufactured with either a CdS [50, 62, 120] or a zinc oxysulfilde (ZnS(O,OH)) buffer layer deposited between the CIGSe light absorber and the front contact [121, 122]. In the vicinity of the buffer layer a hetero-junction is formed between a p-type CIGSe and a Cu-poor CIGSe phase [25], which is widely accepted to be an ordered vacancy compound (OVC) [26–28].

Intrinsic defect pairs may order in a low energy configuration to minimize the Madelung energy at low temperatures by repeating the defect pair of ($2V_{Cu}^{2-}$+In_{Cu}^{2+}). This process is based on the following reaction: $nCuInSe_2 + mIn \rightarrow Cu_{n-3m}In_{n+m}Se_{2n} + 3mCu$, where m=1,2,3,...N, and n=3,4,5,...N. In their seminal work of Zunger and his coworkers referred above, they consider the following rules to distribute the ($2V_{Cu}^{2-}$+In_{Cu}^{2+}) defects in the OVC: (a) minimum Madelung energy and (b) minimal deviation from the octet rule. Regarding the rule (a), they consider the charge of V_{Cu}, Cu, In and Se equal to their nominal charge, i.e. 0, 1, 3, and -2, respectively. Each Se is surrounded by four cations. Keeping minimum deviation from the octet rule gives rise to three different types of tetrahedron around the Se: V_{Cu}+Cu+2In ($k = 7$), 2Cu+2In ($k = 8$), and V_{Cu}+3In ($k = 9$), where k represents the sum of valence electrons of four cations surrounding Se. Since $k = 7$ and $k = 9$ are differently charged, they remain nearby to raise Coulomb attraction. Furthermore, the number of $k = 7$ and $k = 9$ clusters in $CuIn_5Se_8$ are equal to keep the charge of the whole system neutral. Although $CuInSe_2$ consists of 100 % $k = 8$ clusters, $CuIn_5Se_8$ has 50 % of $k = 7$ and 50 % of $k = 9$ clusters [123], hence, in average the k=8 octet rule is respected.

In recent years there is a constantly growing interest and ongoing scientific discussion

to look for alternative materials containing earth-abundant elements that can be used as efficient absorber material. Current solar cells with high energy conversion efficiency such as Si-based and thin film solar cells using $CuIn_{1-x}Ga_xSe_2$ (CIGSe) have natural limitations that prevent them reaching the terawatt production scale. The low attainability and high expense of In and Ga makes the production of these cells on a massive scale unpractical. For the manufacturing of single-crystal Si cells, tremendous amount of energy and natural resources are needed as well [124] for the purification of Si and for the zone melting process to obtain single crystals with controlled quality. A promising alternative to the ternary CIGSe compound is quaternary $Cu_2ZnSnSe_4$ (CZTSe). Instead of In and Ga, CZTSe contains zinc (Zn) and tin (Sn) that are earth-abundant, inexpensive, and non-toxic elements. CZTSe is derived by substituting half of the indium atoms with zinc and the other half with tin in the $CuInSe_2$ (CISe) chalcopyrite compound. In the CISe chalcopyrite-type structure two different cations (Cu and In) are present in the cation tetrahedra. For comparison, in CZTSe three different cations are involved in the tetrahedra [33]. Although so far CZTSe-based solar cells are not as efficient as CIGSe-based solar cells, the conversion efficiency of 12.6% reached for CZTSe-based devices [22] show a great potential of CZTSe to serve as absorber layer in low-cost and high-efficiency solar cells.

In experimental studies it has been shown that the incorporation of small amounts of Na and K with the concentration of around 0.1 atomic percent into the CIGSe layer increases the efficiency of the solar cell devices [3, 50]. However, so far the driving mechanism behind the benign effect of Na and K upon the efficiency of thin film solar cells is not well understood, and their function is highly debated.

Considering that in solar cells fabricated on an industrial scale mainly soda-lime glass (SLG) is used as the substrate, the issue of Na and K impurities becomes even more important. Namely, SLG contains both Na and K in oxide form, and during the thin film deposition these elements diffuse into the CIGSe absorber layer. The amount of K included in SLG, however, is less than Na [50, 125]. This is why the incorporation of Na into the absorber layer has been a very hot topic of scientific research [57, 126–128], and was extensively studied since the work of Hedstroem *et al.* [49]. In contrast to

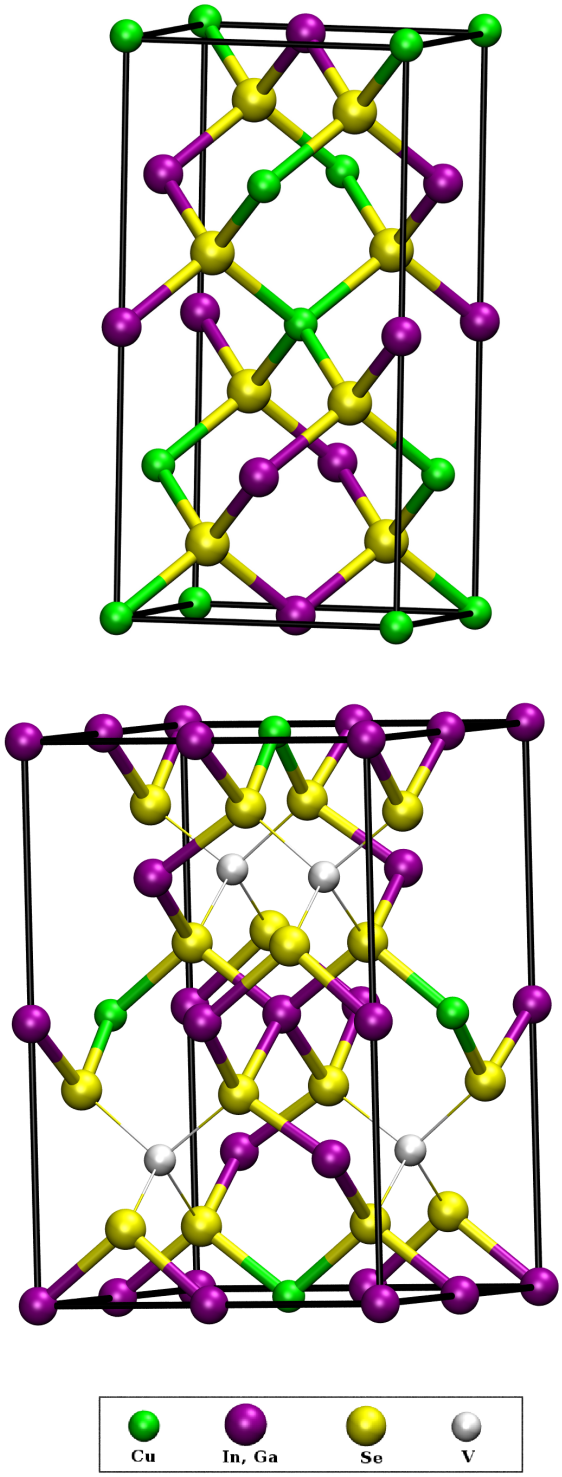

Figure 4.1: The crystal structure showing the conventional tetragonal unit cell of $Cu(In,Ga)Se_2$ (top panel) and chalcopyrite polytipe of $CuIn_5Se_8$ (bottom panel) ordered vacancy compound. V in this notation refers to pristine cupper vacancy sites that are present in $CuIn_5Se_8$.

Na, the diffusion and incorporation of K into the absorber layer is a relatively new topic [4, 50, 60, 61].

Recent experiments on CIGSe thin film solar cells with enamelled steel sheets as substrate, which includes a higher amount of K than Na, have indicated higher doping and stronger elemental grading profiles of K compared to the reference samples on glass substrates [4, 60]. The control over the incorporation of Na and K into the absorber layer is a crucial issue for increasing the efficiency of chalcopyrite thin film solar cells.

Na and K exhibit homologous behaviour and have common chemical properties. This would suggest that they should have similar effects upon the atomic and electronic structure of the light absorber layer. Furthermore, taking into account the ionic radius of K^+, which is larger than Na^+, one would expect a lower diffusivity of K, and K may not be able to occupy certain sites in the absorber layer [129].

The recent report of Wang *et al.* have anounced an efficiency of the CZTSe solar cells reaching 12.6% [22]. Thus, there is a considerable progress being made to further boost the efficiency of CZTSe cells. For this it is highly important to establish the function and understand the effects of various defects in this material as well. By widening our knowledge about the defect physics, one can assess more precisely which defects are detrimental for the performance of the cell, so that the formation of such harmful defects could be prevented during the synthesis.

In 2013 Han *et al.* have studied the effects of intrinsic defects on CZTS. They showed that CZTS is thermodynamically a stable compound and the formation energy of defects are positive. They have also investigated which intrinsic defects stimulate the formation of recombination centers within the absorber layer [130]. However there was not much research published about the effect of extrinsic deffects on CZTSe. Due to the similarity between CISe and CZTSe one may consider acquiring some beneficial conclusions from the vastly investigated CIGSe cells, such as insertion of extrinsic defects like sodium and potassium in the light absorber layer. Considering the empirically well proven fact that the incorporation of a small amount of Na into CISe improved its conversion efficieny and p-type conductivity [131, 132], it was commonly accepted that Na impurities are the best choice for improving the performance of CIGSe cells. However, replacing SLG

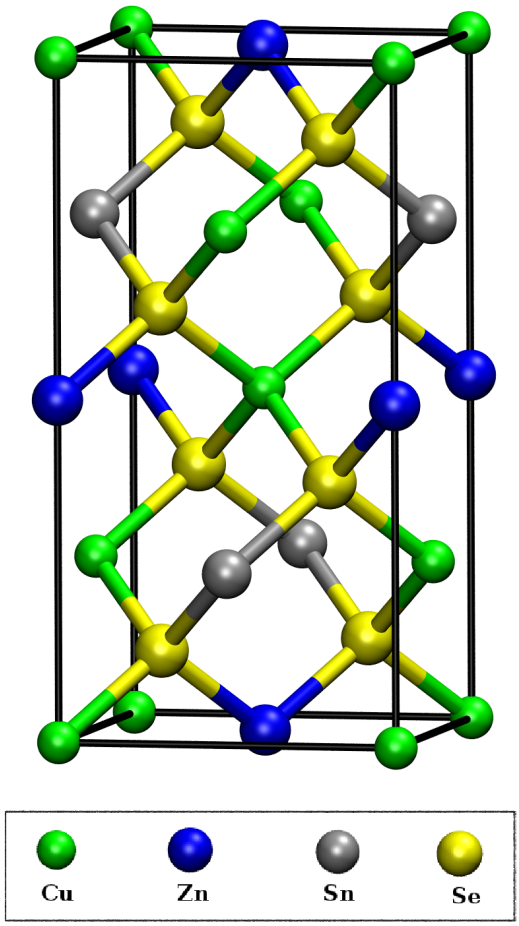

Figure 4.2: The crystal structure of the $Cu_2ZnSnSe_4$ showing the conventional tetragonal cell .

substrate with enameled steel substrate containing more K compared to Na provided a new insight in considering the benign role of K in device performance [4, 50, 60, 61]. In addition to the Na and K diffusing out of the substrate into CIGSe during the growth process, alkaline metals can be also incorporated into the absorber layer via the so called post deposition treatment (PDT). During PDT a small amount of NaF and/or KF salt is deposited onto the CIGSe layer after its growth have been finished. PDT unveiled a remarkable role of K in improving the quality of the pn-junction by reducing recombination at the CdS/CIGSe interface [50, 62]. Also, PDT with additional KF shorten the deposition period of CdS, which results in forming a thinner buffer layer without weakening the cell performance [50, 63]. Considering these regards, one can expect that

sodium and potassium may play a favourable role in CZTSe too.

To provide new insights from theoretical calculations on the structure and energetics of Na and K impurities in CIGSe and CZTSe light absorber layers, the formation energies of K and Na defects in $CuInSe_2$, $CuIn_5Se_8$ and $Cu_2ZnSnSe_4$ have been studied. In addition to Na and K extrinsic defects, the incorporation of Li in CZTSe has been also investigated. $CuInSe_2$ and $CuIn_5Se_8$ serve as models for the bulk CIGSe absorber and for the Cu-poor OVC compound, respectively.

Through the results presented in this work, I assess which lattice sites are more favourable to act as inclusion sites for Na and K, and which of these defects are detrimental for the efficiency of CIGSe solar cells. In addition to point defects related to Li (in CZTSe), Na and K impurities, the formation of other defect complexes like dumbbells have also been investigated. By calculating the band structure of the above mentioned systems in the presence of defects a thorough schematic overview on the electronic structure of these materials in the presence of defects has been presented.

All calculations were carried out within the framework of density functional theory (DFT) as implemented in the VASP program package [133, 134] using the projector-augmented wave method [135,136]. The wave functions were expanded in form of plane-waves up to a cut-off energy of 400 eV. For systems with odd number of electrons spin polarized calculations have been performed. The exchange-correlation potential has been treated with the HSE06 [137] hybrid functional in order to improve the thermodynamics and electronic properties of semiconductors. The parameter α, which determines the amount of Hartree-Fock exchange in the HSE06 calculations, has been set to 0.30 for CISe and 0.27 for CZTSe [138–140]. In the following text we will refer to this functional as HSEα. In comparison to adjusting α, similar methodology is also often used in the literature for the investigation of point defects and impurities in $CuInSe_2$, where instead of α the range separation parameter is adjusted [141, 142].

The crystal structure of the conventional tetragonal cells of bulk $CuInSe_2$ and the chalcopyrite polytipe of $CuIn_5Se_8$ are shown in Figure 4.1. In this work, the calculations were carried out for a 64-atom and 56-atom tetragonal supercells for $CuInSe_2$ and $CuIn_5Se_8$, respectively. In order to estimate the dependency of the formation energies

Table 4.1: Comparison between experimentally measured and calculated equilibrium lattice constants (a and c), tetragonal elongation (η=c/a) and band gaps (E_g) of $CuInSe_2$ and $CuIn_5Se_8$.

	a (Å)	c (Å)	η	E_g (eV)	Ref.
$CuInSe_2$	11.68	11.75	1.006	1.04	Current work
$CuInSe_2$	11.56	11.82	11.005	1.04	[147, 148]
$CuIn_5Se_8$	11.68	11.74	1.005	1.23	Current work
$CuIn_5Se_8$	11.44	11.62	1.016	1.23	[149, 150]
$Cu_2ZnSnSe_4$	11.47	11.40	0.994	0.95	Current work
$Cu_2ZnSnSe_4$	11.36	11.37	1.001	1-1.56	[151–154]

on the size of the supercell, I have performed test calculations on Na and K defects in large 216-atom supercells of $CuInSe_2$, and I found that the formation energies were in the range of $\pm$ 0.1 eV compared to the 64-atom case. Hence, I expect that the data presented here for the 64-atom and 56-atom supercells are qualitatively rather accurate, and using larger supercells would not change the results considerably.

Since the symmetry of CZTSe is lower compared to CISe, the bulk $Cu_2ZnSnSe_4$ was represented by employing a 216-atom supercell. The brillouin zone integration was performed with a 2×2×2 k-point mesh.

To calculate the fundamental bulk properties, first I optimised the atomic positions using the fixed experimental volume and then I relaxed the lattice constants together with the atomic positions for zero external pressure computed via the cell tensors. All the calculations were carried out using the calculated equilibrium volume for a defect-free bulk of CISe and CZTSe.

The optimized cell parameters and band gaps computed with HSEα are summarized in Table 4.1. In agreement with the experimental values, my results show that the calculated band gap of $CuIn_5Se_8$ (1.23 eV) is larger than that of the $CuInSe_2$ (1.04 eV). Regarding CZTSe, one group of experimental studies report a band gap in the range of 1.4-1.6 eV for both CZTS and CZTSe [143–146], which shows a discordance with density functional theory calculations [29]. However, other papers announced a discrepancy of about 0.5 eV for CZTSe and published the band gap energy to be in the range of 0.8-1.0 eV for CZTSe [153–155]. Taking into account that various experimental methos were used for measuring the band gap, the overstimation of band gap can be attributed

to the existing secondary phases, i.e. ZnSe and Cu_2SnSe_3 in the light absorber layer, which can not be discerned by XRD [154]. Furthermore, the underlying methods were also quite different, because methods based on optical excitation and electric resistivity measurements are known to often produce different band gaps.
The formation energies of defects presented in the current chapter have been evaluated through applying the supercell approch and Equation 2.36, as presented in Sections 2.11 and 2.12.

4.2 Static Results on the CISe Absorber Layer

According to the contemporary scientific literature, through the creation of either a Cu vacancy or an In vacancy in $CuInSe_2$ (CISe), the four nearest-neighbour Se atoms relax inward isotropically. In case of V_{Cu}, the Se atoms relax 0.07 Å and in the case of V_{In}, they relax 0.21 Å toward each other. The further relaxation for V_{In} is due to the larger size of In [156]. Each Se is surronded by two Cu and two In atoms which relax under Se vacancy defect condition. While the nearest-neighbour In atoms relax towards each other, Cu atom move away from each other. According to formation energy calculations, under both Cu-rich and Cu-poor conditions, V_{Cu}^{-} is the most favourable of the three vacancies at 0.92 eV [157] under Cu-rich condition and about 0.8 eV under Cu-poor condition [156]. The formation energy of V_{Se}^{2-} is 1.55 eV under Cu-rich and about 2.45 eV under Cu-poor condition. V_{In}^{2-} exhibits high formation energy in both Cu-poor and Cu-rich conditions. For comparison, Zhang *et al.* reported the formation energy of 4.29 eV for V_{In}^{3-} calculated by LDA.

4.2.1 Na and K Point Defects in $CuInSe_2$

To study the energetics of point defect formation related to Na and K impurities, a Na or K atom was placed in a 64-atom supercell of $CuInSe_2$ either as an interstitial or as a substitutional defect. The atomic structure was fully relaxed with the HSEα functional both for charged and neutral defects. The calculated formation energies for different

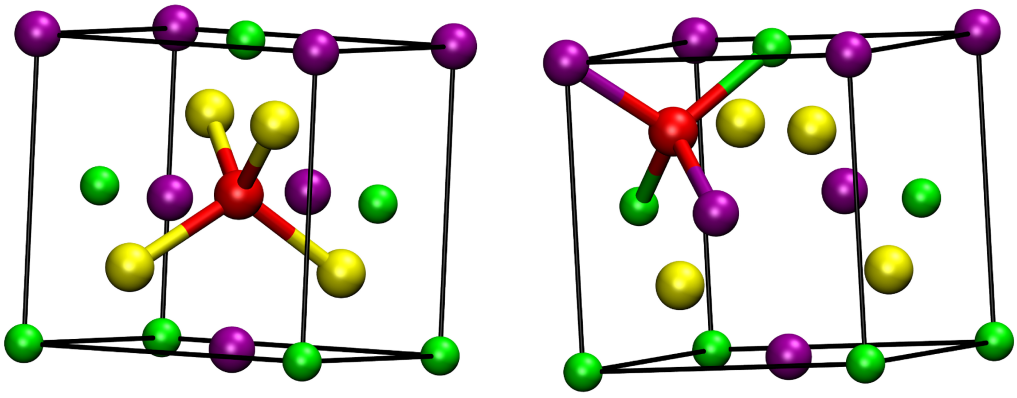

Figure 4.3: The position of the two different interstitial defects in $CuInSe_2$. In left-side and right-side subfigures, the interstitial defect is tetrahedrally coordinated by four anions and by four cations, respectively. Na or K interstitials are shown as red spheres, and the other atoms are presented using the same color scheme as in Figure 4.1. For clarity, only one half of a $CuInSe_2$ conventional cell is shown.

defects are summarized in Table 4.2 for the most stable charge state. Since from the experiments it is known that the light absorber is a p-type material, in this work all formation energies are reported for the scenario where the electron chemical potential μ_e is set at the VBM. Figure 4.4 and Figure 4.5 show the formation energy of various Na and K defects as a function of μ_e.

In full agreement with a previous work [158] which was focusing on Na impurities in $CuInSe_2$, I also found that among Cu, In, and Se substitutional sites the Cu site is energetically the most favorable to host Na or K atoms. I found that for a p-type material where the chemical potential of the electron reservoir is at VBM, both for Na and K the positively charged Na^{+}_{Cu} and K^{+}_{Cu} defects are slightly more stable compared to the charge neutral Na^{0}_{Cu} and K^{0}_{Cu} defects. This is due to the larger electropositivity of Na and K with respect to Cu. Still, one needs to point out that the difference between the formation energies of neutral and +1 charged defects (about 0.08 eV) is comparable with the magnitude of the E^{q}_{corr} correction term resulting from the band alignment and charge correction (see Section 2.12). For Na^{0}_{Cu} and K^{0}_{Cu} substitutional defects, I have calculated a formation energy of -1.08 eV and -0.26 eV, respectively. The negative formation energies suggest that at low impurity concentration such defects can be spontaneously formed. Considering the high formation energies of 0.96 eV

and 1.67 eV calculated for Na^0_{In} and K^0_{In}, respectively, creating substitutional defects in indium positions in $CuInSe_2$ is rather unlikely. Occupying selenium sites by Na or K atoms is also less likely, though the formation energies of 0.66 and 0.55 eV computed for Na^+_{Se} and K^+_{Se} are considerably lower in energy than the In substitutional defects. For substitutional defects on Cu and In positions there is a qualitative difference between Na and K. Namely, the lower formation energies favor Na-related defects (on the order of 0.7 eV versus K). For comparison, on the Se site the Na and K-related substitutional defects are almost isoenergetic.

Beside the substitutional defects I also studied the formation energy of Na and K defects in two different interstitial positions, where the impurity is either being coordinated to four Se anions (as shown in the left panel of Figure 4.3), or four cations (two Cu and two In, as shown in the right panel of Figure 4.3). In table 4.2 and throughout the text these two interstitial positions are represented with the short hand notations *ac*, and *cc*, respectively. Our results show, in agreement with Reference 158, that the *cc* position is more favorable than the *ac* both for Na and K. The corresponding formation energy for the *cc* interstitial position is -1.25 eV and -0.30 eV for Na^+_{cc} and K^+_{cc}, respectively, whereas the formation energies calculated for Na^+_{ac} and K^+_{ac} were -1.17 eV and +0.48 eV. I found that for Na the *cc* interstitial position is more favorable than all substitutional positions, and for K it is energetically unfavorable to be situated in the *ac* interstitial position. From the perspective of the defect formation energy our data indicates that there is a qualitative difference between Na and K also for the interstitial positions. Namely, for Na the energy difference of 0.08 eV between the *cc* and *ac* sites is negligible compared to the 0.78 eV computed for K. Thus, if Na and K were incorporated into $CuInSe_2$ as interstitials, Na could occupy both *cc* and *ac* sites, but K would sit predominantly on *cc* positions. Furthermore, by comparing the formation energies of the interstitial and substitutional defects, it is interesting to note that interstitial positions are thermodynamically more favorable than all substitutional positions for a Na atom. In contrast, this is not the case for K. Thus, our results indicate that for a heavily p-doped $CuInSe_2$ material (where μ_e=0 eV), Na point defects will be incorporated into the bulk $CuInSe_2$ light absorber material as interstitial defects. Above μ_e=0.1 eV the

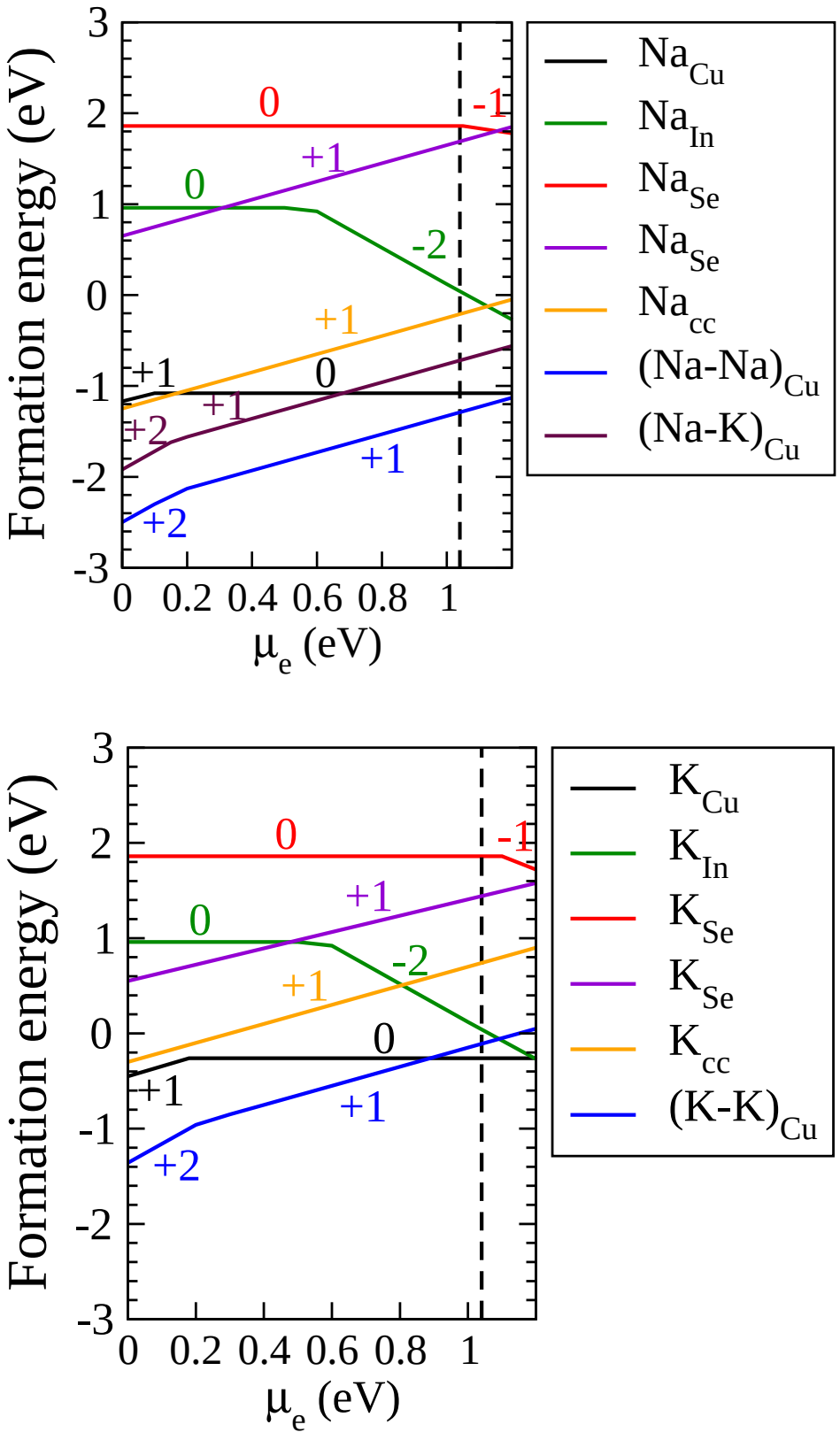

Figure 4.4: Formation energies of various Na and K defects in $CuInSe_2$ as a function of the electron chemical potential, where $\mu_e = 0$ corresponds to a p-type and μ_e = CBM (where CBM is the conduction band minimum) to an n-type material, respectively. The horizontal dashed line indicates the theoretically computed band gap for $CuInSe_2$.

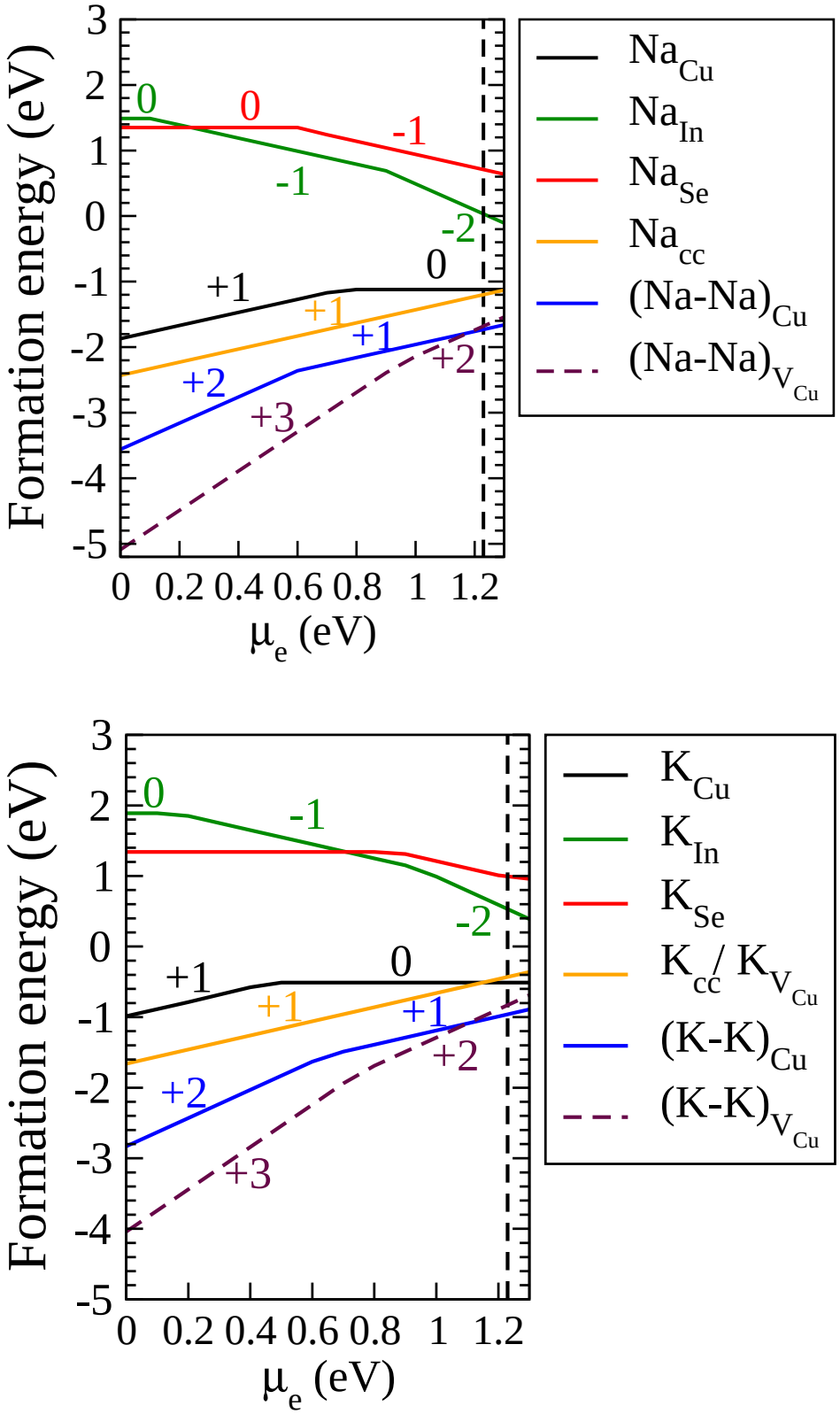

Figure 4.5: Formation energies of various Na and K defects in $CuIn_5Se_8$ as a function of the electron chemical potential, where $\mu_e = 0$ corresponds to a p-type and $\mu_e =$ CBM to an n-type material, respectively. The horizontal dashed line shows the theoretically computed band gap for the bulk defect-free ordered $CuIn_5Se_8$.

Na_{Cu} substitutional defect will become the most stable point defect. In contrast to Na, K will occupy substitutional positions in the Cu sub-lattice for the full range of μ_e, i. e. even under n-type conditions.

Table 4.2: Defect formation energy (in eV) calculated with the HSEα functional for Na and K impurities in $CuInSe_2$ and $CuIn_5Se_8$ assuming that the electron chemical potential $\mu_e = 0$, i. e. referring to a *p*-type material. In the $CuIn_5Se_8$ material the V_{Cu} index refers to the pristine Cu vacancy site in the structure.

Defect	$CuInSe_2$	$CuIn_5Se_8$
Na^{+}_{Cu}	-1.16	-1.90
K^{+}_{Cu}	-0.49	-1.02
Na^{0}_{In}	0.96	1.49
K^{0}_{In}	1.67	1.89
Na^{+}_{Se}	0.66	0.29
K^{+}_{Se}	0.55	0.40
Na^{+}_{ac}	-1.17	-1.34
K^{+}_{ac}	0.48	-0.10
Na^{+}_{cc}	-1.25	-2.42*
K^{+}_{cc}	-0.30	-1.67*
$Na^{+}_{V_{Cu}}$	–	-2.43
$K^{+}_{V_{Cu}}$	–	-1.66
$(Na\text{-}Na)^{+}_{Cu}$	-2.29	-2.95
$(Na\text{-}K)^{+}_{Cu}$	-1.71	-2.12
$(K\text{-}K)^{+}_{Cu}$	-1.11	-2.17
$(Na\text{-}Na)^{2+}_{Cu}$	-2.50	-3.56
$(Na\text{-}K)^{2+}_{Cu}$	-1.93	-2.79
$(K\text{-}K)^{2+}_{Cu}$	-1.36	-2.83
$(Na\text{-}Na)^{2+}_{VCu}$	–	-4.09
$(Na\text{-}K)^{2+}_{VCu}$	–	-3.29
$(K\text{-}K)^{2+}_{VCu}$	–	-3.24
$(Na\text{-}Na)^{3+}_{VCu}$	–	-5.09
$(Na\text{-}K)^{3+}_{VCu}$	–	-3.99
$(K\text{-}K)^{3+}_{VCu}$	–	-4.04

* relaxed to $_{V_{Cu}}$ position

4.2.2 Na and K Dumbbells in $CuInSe_2$

In Reference 158 it was shown that for Na impurities it is possible to form (Na-Na) dumbbells as substitutional defects in Cu sites of $CuInSe_2$. In light of the aforementioned results [158], here I look into the issue whether (K-K) dumbbells can be formed in spite of the larger size of the K impurity. In addition, I have also investigated if mixed dumbbells can be created between Na and K. To clarify this question, I have carried out calculations on three different dumbbells, i. e. (Na-Na), (Na-K) and (K-K) dumbbells located in a Cu substitutional site. My study confirms that the formation of dumbbells is highly probable. I found that dumbbells formed by two Na atoms, or one Na and one K atom, or even by two K atoms could occupy the Cu site, which is surprising due to the large size of these dumbbells. The calculated formation energy of a (Na-Na)$^{2+}_{\mathrm{Cu}}$ dumbbell in a Cu substitutional position is -2.50 eV. Now if one assumes that in $CuInSe_2$ inserting two Na atoms in two distinct and spatially well separated *cc* interstitial position would result in a formation energy twice larger than a Na^{+}_{cc} defect (i. e. -2.50 eV), then the formation of two separated interstitial defects competes with the formation of a dumbbell.

In contrast to Na, I found that for K atoms in $CuInSe_2$ it will be always more preferable to form (K-K)$^{2+}_{\mathrm{Cu}}$ dumbbells with the formation energy of -1.36 eV, which is clearly more stable than having distinct K^{+}_{Cu} or K^{+}_{cc} defects. This binding energy computed for a (K-K) dumbbell compared to distinct K defects suggests that for the system it is more favorable to cluster two K atoms together, probably due to reduced strain.

To check the accuracy of my results, I have recalculated the formation energy of the following defects in a 216-atom $CuInSe_2$ supercell: Na^{+}_{Cu}, K^{+}_{Cu}, Na^{+}_{cc}, (Na-Na)$^{+}_{\mathrm{Cu}}$, (Na-K)$^{+}_{\mathrm{Cu}}$, and (K-K)$^{+}_{\mathrm{Cu}}$. The resulting formation energies were subsequently -1.02, -0.29, -1.13, -2.12, -1.64, and -1.10 eV, which shows that the energies presented in Table 4.2 are well converged even for the smaller 64-atom supercell.

4.2.3 Na and K Point Defects in $CuIn_5Se_8$

After the investigation of the stoichiometric $CuInSe_2$ compound, I have done the same type of calculations for the Cu-poor $CuIn_5Se_8$ phase, which is representative of thin film solar cells grown under Cu-poor conditions and also to the OVC compounds found at the interface with the CdS buffer layer. The structure of $CuIn_5Se_8$ is obtained from $CuInSe_2$ by inserting a periodic arrangement of defect complexes formed by an indium antisite substituting copper (In_{Cu}) and two copper vacancies (referred as "pristine vacancies" [123]), see Figure 4.1.

In the case of $CuIn_5Se_8$, similarly to $CuInSe_2$, the Cu site is the most favorable site within the substitutional positions for both Na and K atoms. However, Na_{Cu} and K_{Cu} substitutional defects in $CuIn_5Se_8$ are more likely to form compared with $CuInSe_2$, despite the low Cu concentration in this Cu-poor phase. This is in agreement with the experimental finding that a KF post-deposition treatment makes the absorber even more Cu-poor [50].

Under strongly doped p-type conditions the formation of charge neutral Na^0_{In}, K^0_{In}, Na^0_{Se}, and K^0_{Se} defects are energetically very unfavorable, similarly to $CuInSe_2$. In contrast to the $CuInSe_2$ stoichiometric compound, where the charge neutral Na^0_{In}, K^0_{In}, Na^0_{Se}, and K^0_{Se} defects are stable over a large range of the electron chemical potential μ_e, in $CuIn_5Se_8$ even in a p-type material the Na^{-1}_{In} and K^{-1}_{In} defects become dominant once μ_e is larger than 0.1 eV (see Figure 4.5). Similarly, in $CuIn_5Se_8$ under n-type conditions the most stable charge state of the Se-related substitutional defects changes from charge neutral to Na^{-1}_{Se}, and K^{-1}_{Se}, whereas in $CuInSe_2$ the charge neutral state is the most stable for the whole range of μ_e.

The insertion of Na and K interstitials is energetically even more favorable in $CuIn_5Se_8$ than $CuInSe_2$ due to the presence of the two pristine Cu vacancies per formula unit, which make the accommodation of the interstitial defects easier in the structure. In fact, if one starts the structural optimization from *cc* interstitial positions, than both the Na and K interstitial atoms relax spontaneously to the pristine Cu vacancy site. By comparing the energetics of Na and K point defects in $CuIn_5Se_8$, I found that energet-

ically the most stable site for the inclusion of Na and K impurities is the pristine Cu defect site. The situation is similar but not identical to the case of Cd insertion [123], because although Na and K prefer copper sites, but due to a different valency these impurities induce a long range disorder in the pristine vacancy network.

4.2.4 Na and K Dumbbells in $CuIn_5Se_8$

By inserting dumbbells into a Cu site as a substitutional defect or into a pristine vacant Cu site I have also investigated the formation of dumbbells in the $CuIn_5Se_8$ material. I found that both Na and K atoms can enter in $CuIn_5Se_8$ in form of (Na-Na), (K-K) or mixed (Na-K) dumbbells. The formation of dumbbells in a pristine vacant Cu site is energetically more favorable than forming dumbbells as substitutional defects in a Cu position. This is not surprising considering that the $CuIn_5Se_8$ compound is already rather Cu-poor compared to $CuInSe_2$. Comparing the formation energies of the (Na-Na) dumbbell in a vacant Cu position with two Na in two pristine Cu positions reveals that the formation of two spatially separated Na point defects is as much likely as the formation of a Na dumbbell.

4.2.5 Band Structure and Transition Levels of Na and K Defects

To assess the effect of Na and K impurities on the electronic structure of $CuInSe_2$ and $CuIn_5Se_8$, first I have calculated the band structure of the impurity-free compounds to serve as a reference. Next I have evaluated the band structure (see Figures 4.6 and 4.7) of the most stable configurations for the Na and K impurities together with the unstable configurations where Na and K is located on Se substitutional positions. The band structures are calculated for the most stable charge state across the range of the electron chemical potential defined by the band gap. I note that adding/removing one electron to/from the ground state of a system with large number of electrons changes its band structure only slightly. This is due to the relaxation of all orbitals in the excited system. The larger band gap of $CuIn_5Se_8$ compared to $CuInSe_2$ is due to a periodic network of Cu vacancies, which decrease the contribution of Cu(d) orbitals at the top

of the valence band of $CuIn_5Se_8$, leading to a reduction of the Cu(d)–Se(p) inter-band repulsion. This lowers the VBM of $CuIn_5Se_8$, resulting in a wider band gap [26, 47].
In addition to the electronic band structures I have also evaluated the thermodynamic charge transition levels of the various defects. The transition levels $\epsilon_\alpha(q/q\prime)$ introduced in Section 2.11 define the position of thermodynamic transitions between the different charge states for the same defect type.
The higher ionization energy of deep levels reduce their contribution to the free charge carriers and acts like detrimental traps by acting as recombination centers. Recombination centers have roughly equal capture cross-sections for both electrons and holes, and are commonly stationed near the middle of the band gap. These levels are very detrimental in a photovoltaic cell, so the formation of such defects should be prevented, because they reduce the cell's efficiency through current loss in the absorber. The calculated charge transition levels indicate that in $CuInSe_2$ the Na_{Cu} and K_{Cu} defects induce extremely deep (0/+) transition levels which are located 0.08 eV and 0.23 eV above the VBM, respectively. As a conclusion, Na_{Cu} and K_{Cu} do not act as recombination centers, and one can derive that Na and K point defects on Cu positions are not having a negative impact on the cell efficiency. In contrast, in $CuIn_5Se_8$ they have (0/+) transition levels which are in the middle of the gap: for Na_{Cu}, $\epsilon_\alpha(0/+) = E_{VBM} + 0.78\,\text{eV}$ and for K_{Cu}, $\epsilon_\alpha(0/+) = E_{VBM} + 0.50\,\text{eV}$. This means that K_{Cu} could act as a major electron trap, especially considering that due to the low formation energy of this defect type one would expect that K_{Cu} defects are abundant in the Cu-poor material. In agreement with this current result, it has been shown previously by experiments that the incorporation of K during CIGSe growth at low process temperatures results in the formation of deep defect levels [62]. Two scenarios were suggested to explain these findings: either K impurities as point defects are directly responsible by creating these deep defect states, or K might impact the elemental inter-diffusion, which leads to higher concentration of intrinsic defects. The investigation of such scenarios through experiments are rather cumbersome, and so far no theoretical study has been carried out to shed new light on this issue [159]. According to my findings, the first scenario conforms to my calculations. However, I cannot either confirm or reject the second scenario without looking into the

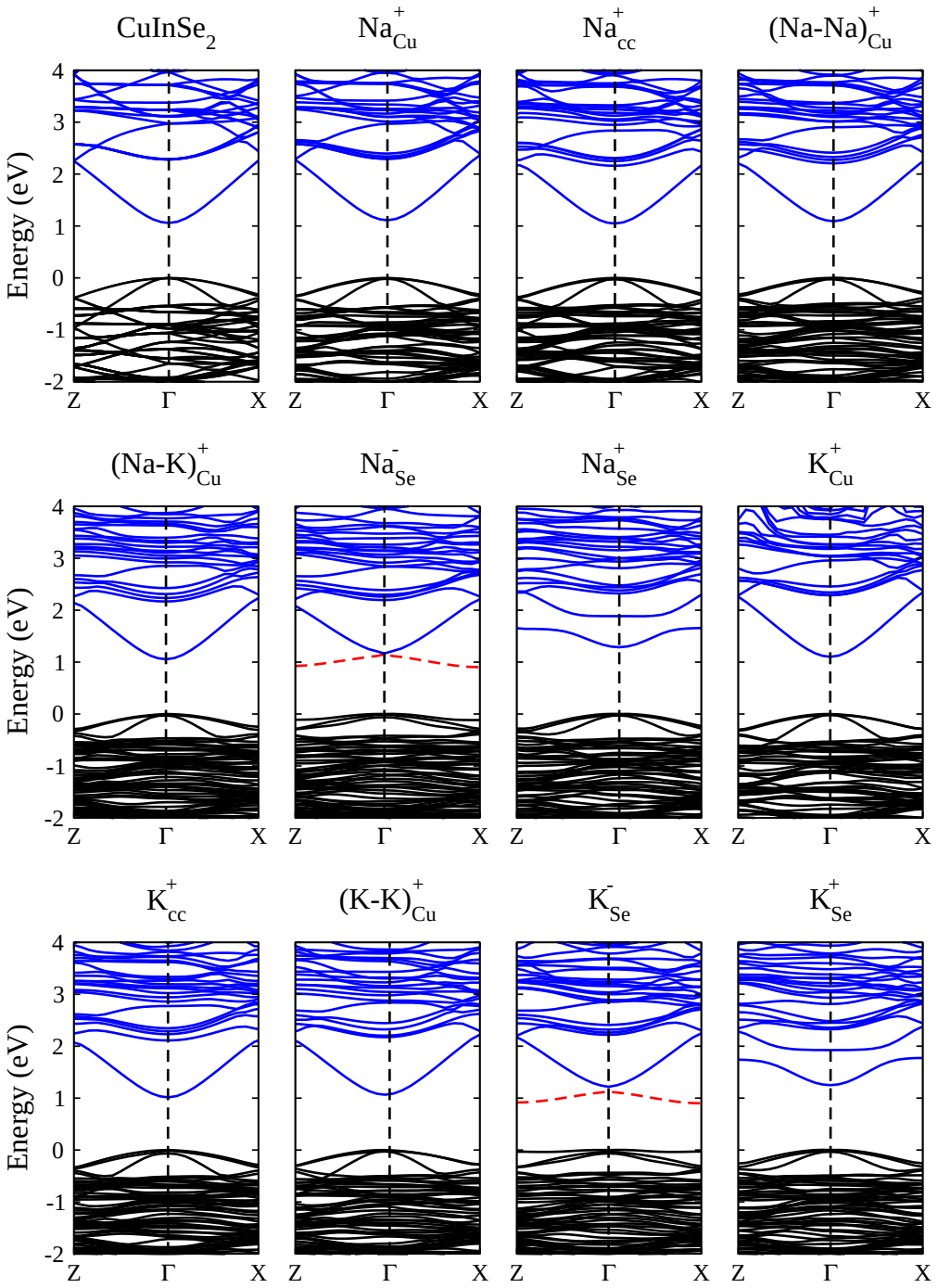

Figure 4.6: Band structure of the clean $CuInSe_2$ compound and the systems with Na and K impurities. The calculated band structure for bulk $CuInSe_2$, Na^{+}_{Cu}, Na^{+}_{cc}, $(Na\text{-}Na)^{+}_{Cu}$,$(Na\text{-}K)^{+}_{Cu}$, Na^{-}_{Se}, Na^{+}_{Se}, K^{+}_{Cu}, K^{+}_{cc}, $(K\text{-}K)^{+}_{Cu}$, K^{-}_{Se} and K^{+}_{Se} defects in $CuInSe_2$ has been illustrated. The occupied and unoccupied levels are shown as black and blue lines, respectively, and red dashed lines represent the defect levels in the gap. The zero of energy is set at the bulk VBM.

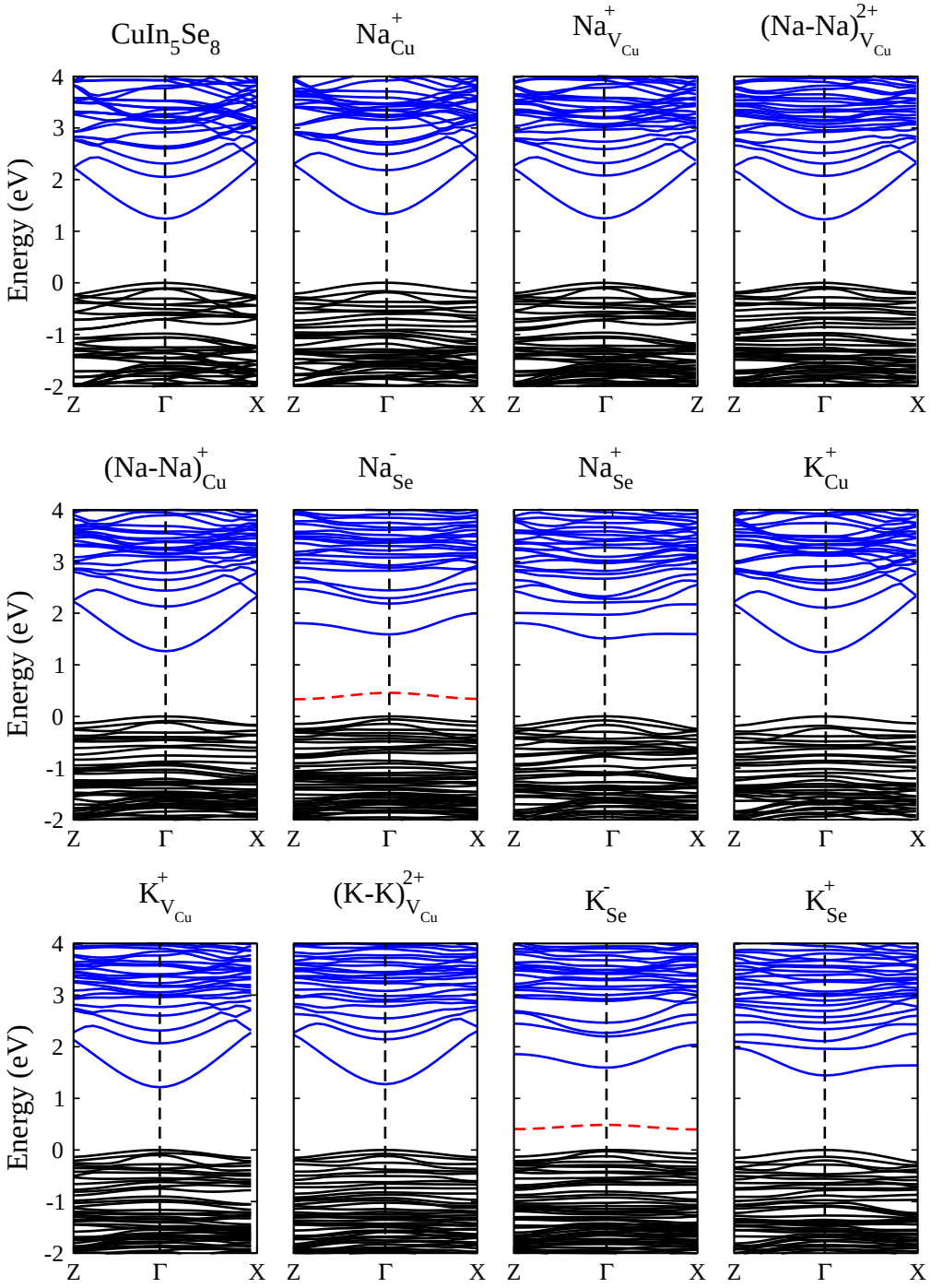

Figure 4.7: Band structure of the clean $CuIn_5Se_8$ compound and the systems with Na and K impurities. The band structure for $CuIn_5Se_8$, Na^{+}_{Cu}, $Na^{+}_{V_{Cu}}$, $(Na\text{-}Na)^{2+}_{V_{Cu}}$,$(Na\text{-}Na)^{+}_{Cu}$, Na^{-}_{Se}, Na^{+}_{Se}, K^{+}_{Cu}, $K^{+}_{V_{Cu}}$, $(K\text{-}K)^{2+}_{V_{Cu}}$, K^{-}_{Se} and K^{+}_{Se} defects in $CuIn_5Se_8$ has been illustrated. The occupied and unoccupied levels are shown as black and blue lines, respectively, and red dashed lines represent the defect levels in the gap. The zero of energy is set at the bulk VBM.

diffusion of the constituent atoms in CIGSe in presence of Na and K.

The charge transition levels created by the (Na-Na) and (K-K) dumbbells in $CuInSe_2$ are located at 0.18 eV and 0.21 eV above the VBM, respectively. This means that creating such dumbbells in the material is not destructive for the carrier transport. On the other hand, the formation of dumbbells by removing a Cu atom in $CuIn_5Se_8$ causes transition levels at 0.60 eV and 0.64 eV above the VBM for $(Na\text{-}Na)_{Cu}$ and $(K\text{-}K)_{Cu}$, respectively. These levels are almost in the middle of the band gap, so they can act as recombination centers, and hinder the carrier transport. This is also true for the (K-K) dumbbell formed in the pristine Cu vacancy in $CuIn_5Se_8$; the transition level is located at 0.75 eV above the VBM. The $(Na\text{-}Na)_{V_{Cu}}$ defect, however, causes a level 0.25 eV below the CBM that is harmless for the carrier transport.

In $CuInSe_2$, Na_{In} and K_{In} exhibit deep (-2/0) transition levels around E_{VBM}+0.60 eV in the band gap, which correspond to a double acceptor level [130], meaning that they undergo a charge transition from 0 directly to -2. Na and K in In site in $CuIn_5Se_8$ show a different behavior and induce two transition levels within the band gap, from 0 to -1 near the VBM, and from -1 to -2 near the CBM. Se-related substitutional defects for both Na and K induce a shallow level near the CBM in $CuInSe_2$ and a deeper level in $CuIn_5Se_8$. Such Se-related defect levels are clearly detrimental for the device efficiency. However, considering their high formation energies these defects should have a low concentration in the CIGSe film.

4.3 Static Results on CZTSe Absorber Layer

4.3.1 Intrinsic Defects in $Cu_2ZnSnSe_4$

The removal of a Cu, Zn, Sn or Se atom from the CZTSe lattice creates intrinsic point defects. The formation of such defects in CZTSe and the isostructural sulfide compound (Cu_2ZnSnS_4) have been studied theoretically [130, 160, 161]. In agreement with the aforementioned work [160], my current results show that among intrinsic point defects in CZTSe the copper vacancy (V_{Cu}) has the lowest formation energy for the

whole range of the chemical potential of the electrons, i. e. under both p- and n-type conditions (see Figure 4.8). By computing the thermodynamic charge transition levels, I found that the only stable charge state for V_{Cu} is -1, i. e. this vacancy does not induce any defect level within the band gap and is not detrimental for the carrier transport in CZTSe. In contrast to V_{Cu}, the tin vacancy (V_{Sn}) creates three levels: ϵ(-2/-) at E_{VBM}+0.08 eV, ϵ(-3/-2) at E_{VBM}+0.27 eV, and ϵ(-4/-3) at E_{VBM}+0.7 eV. As it is shown in Figure 4.8, the formation energy of V_{Sn} falls rapidly by increasing μ_e, i. e. when CZTSe becomes n-type. Considering that V_{Sn} has the highest formation energy among native vacancies (4.21 eV for charge state -1 at the VBM), such defects should have a negligible concentration in a p-type CZTSe material. Although the creation of the ϵ(-4/-3) and ϵ(-3/-2) transition level of V_{Sn} could have negative impact on the efficiency of CZTSe thin film solar cells, this detrimental effect is controlled by the conditions of the CZTSe deposition process, where films are grown p-type and the probability of the formation of Sn vacancies is low. The Zn vacancy (V_{Zn}), similar to V_{Cu}, does not induce transition levels within the band gap. The formation energy of V_{Zn} is rather high compared to V_{Cu} but decreases by increasing μ_e (see Figure 4.8). For the anion vacancy V_{Se} we have calculated the formation energy of 1.91 eV for charge state +1 at the VBM. The presence of V_{Se} in the material induces a charge transition level ϵ(0/+) which is located at E_{VBM}+0.05 eV, so it is not detrimental for the carrier transport.

4.3.2 Li, Na and K Point Defects in $Cu_2ZnSnSe_4$

In this section, I discuss the results of incorporating Li, Na and K into the $Cu_2ZnSnSe_4$ absorber layer, which have been summarized in Table 4.3.

Lithium belongs to the same group of alcali-metal dopants as Na and K. Nevertheless, so far not much have been done to study the effect of Li on the characteristics of the absorber layers. Very recently, a group in the University of Washington has experimentally investigated the effect of group-I dopants on the properties of CZTSe films. Regarding the computational study of the incorporation of Li into CZTSe, only one work is published [162] in which PBE functional is employed for CZTSe. It is well known,

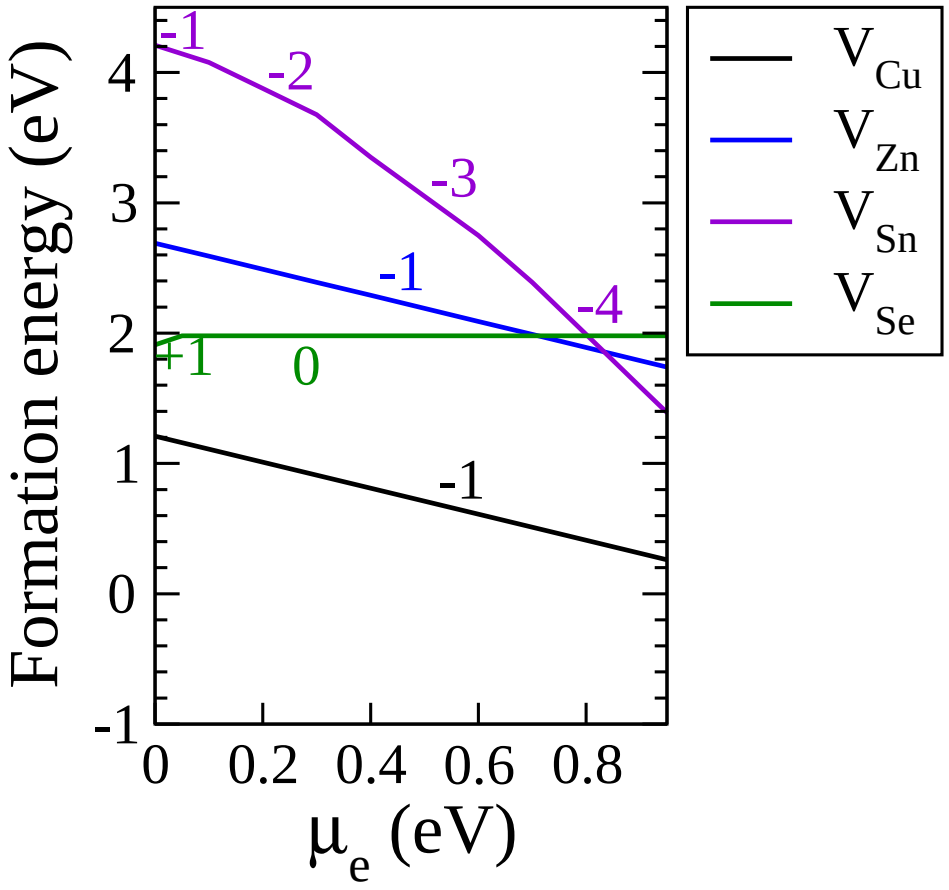

Figure 4.8: The calculated formation energies of pristine vacancies in $Cu_2ZnSnSe_4$ as a function of the chemical potential of the electrons μ_e, where the left (μ_e=0) and right side (μ_e=0.95 eV) of the figure corresponds to p-type and n-type conditions, respectively. The positive and negative numbers next to the lines indicate the most stable charge states for the respective μ_e.

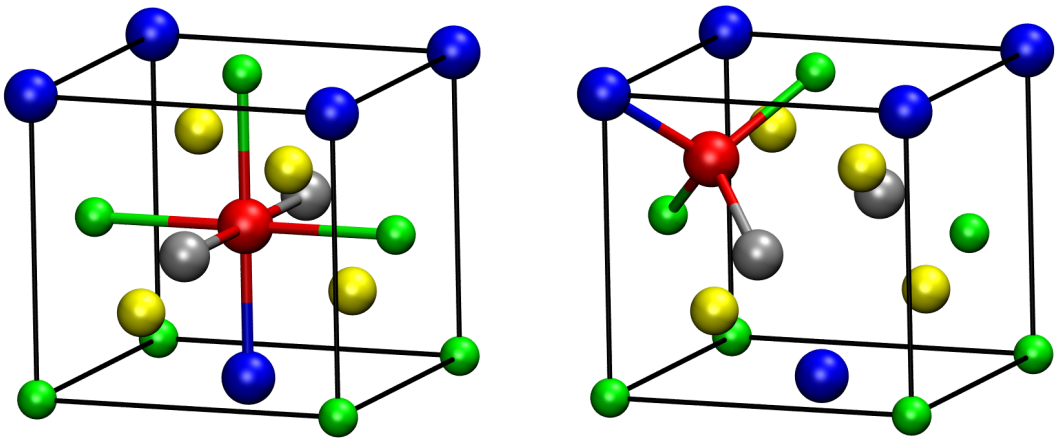

Figure 4.9: Atomic structure showing the local coordination of two different interstitial defects. The octahedrally and tetrahedrally coordinated interstitial is shown in the left and right panel, respectively. The Na or K interstitial atom is represented by a red sphere, and for the rest of the atoms the same color scheme has been used as in Figure 4.2. For clarity, only half of the conventional tetragonal cell is shown.

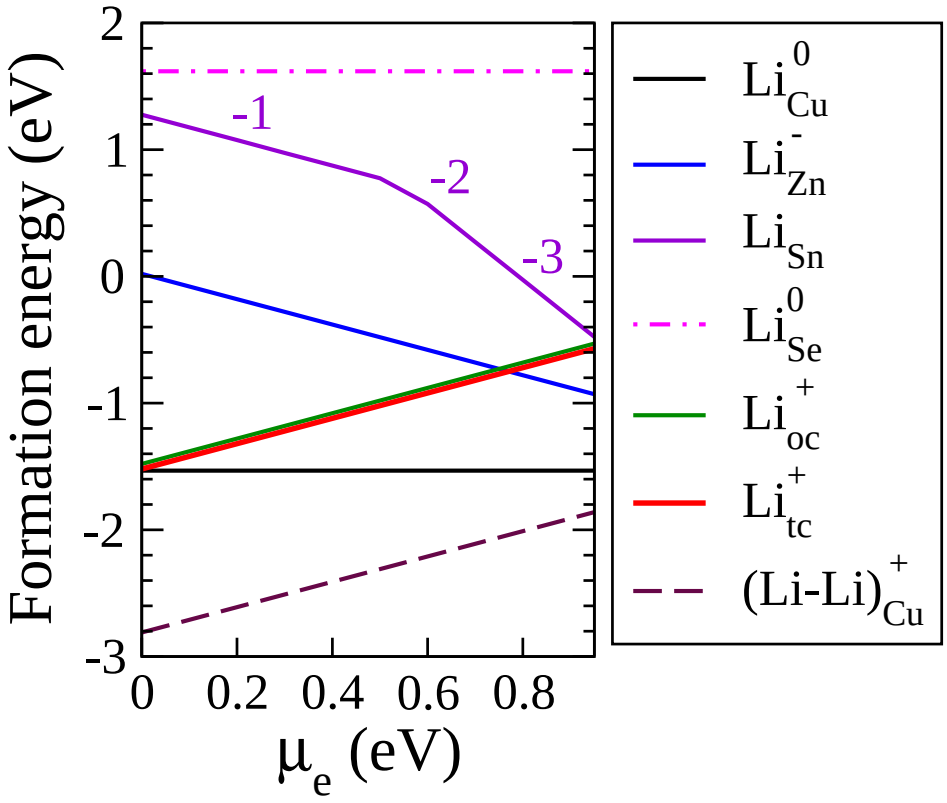

Figure 4.10: The calculated formation energies of Li-related defects in $Cu_2ZnSnSe_4$ as a function of the chemical potential of the electrons μ_e.

however, that semi-local functionals like PBE severely underestimate the bandgap of CZTSe [163], and the right description of the band gap is vital for solar cell devices. In order to shed more light on this topic, I have calculated the formation energy of Li, Na and K defects in different lattice sites by HSE hybrid functional calculations. To assess the relative stability of Li-, Na- and K-related defects, I have computed the formation energies of various defects in different charge states using Equation 1.3.

Interstitial and substitutional defects form by inserting Li, Na and K into the CZTSe bulk and substituting the constituent atoms with Li, Na and K, respectively. The results are summarized in Figures 4.10, 4.11 and 4.12 that show the formation energies as a function of the chemical potential of the electrons μ_e. The group-I dopants can occupy two different interstitial positions with different chemical environments: a Li, Na or K impurity in an interstitial position in the kesterite structure is either octahedrally coordinated (*oc*) by three Cu, two Sn and one Zn cations (see the left panel

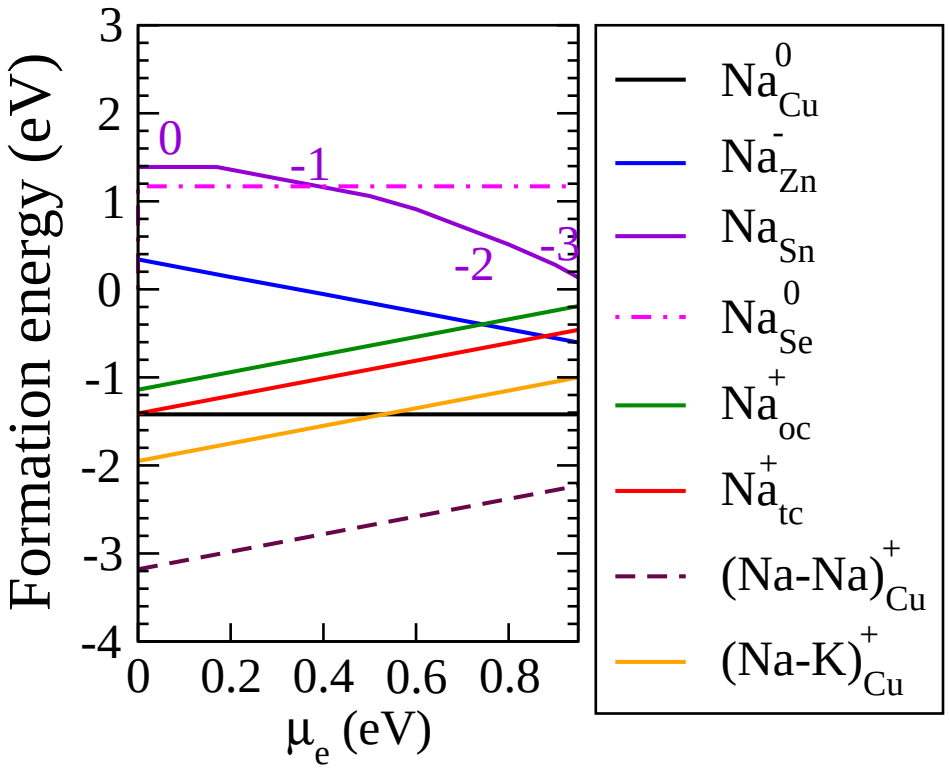

Figure 4.11: The calculated formation energies of Na-related defects in $Cu_2ZnSnSe_4$ as a function of the chemical potential of the electrons μ_e.

in Figure 4.9), or tetrahedrally coordinated (*tc*) by two Cu, one Sn and one Zn atom (see the right panel of Figure 4.9). Our results reveal that for all Li, Na and K impurities, it is energetically more preferable to be located in the *tc* position instead of the *oc* site. For Na impurities in $CuInSe_2$ similar results have been found [158, 164]. Due to the small ion radius for Li, the energy difference of 0.02 eV between the *oc* and *tc* sites is negligible. All Li, Na and K interstitials have only one stable charge state of +1 over the whole range of μ_e. In p-type CZTSe the respective formation energy for Li^+_{oc} and Li^+_{tc} are -1.49 eV and -1.51 eV respectively, and for Na^+_{oc} and Na^+_{tc} -1.14 eV and -1.41 eV, so they are all likely to form. Conversely, due to the larger size of the K impurity, K^+_{oc} and K^+_{tc} interstitials have considerably high formation energies of 1.08 eV and 0.57 eV, respectively. This suggests that in contrast to Li and Na, K interstitials are highly unlikely to be formed in CZTSe. These interstitial defects act as donor and give an electron to the conduction band of CZTSe. Interestingly these defects cause no gap state, i. e. the formation of these defects increases the density of the electrons as

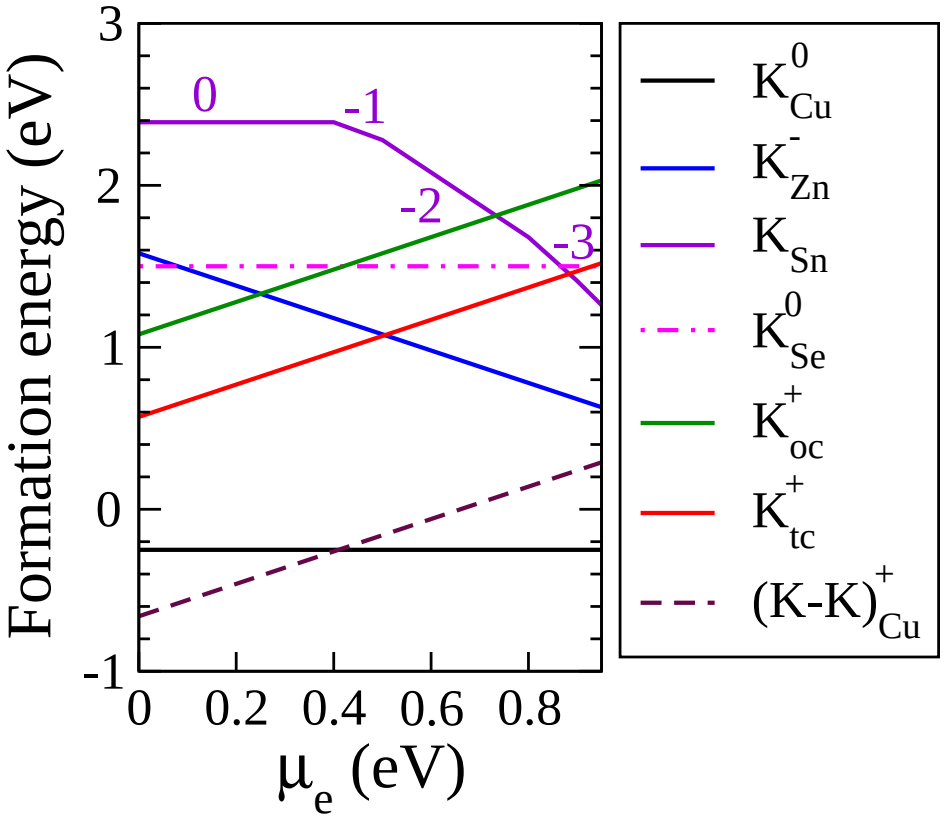

Figure 4.12: The calculated formation energies of K-related defects in $Cu_2ZnSnSe_4$ as a function of the chemical potential of the electrons μ_e.

charge carriers, without acting as recombination centers. Li and Na interstitial defects are metastable for n-type CZTSe, where Li_{Zn} and Na_{Zn} substitutionals become more stable than interstitial defects.

Next, I have studied the formation of Li, Na and K substitutional defects. On the basis of these results I can state that all Li, Na and K prefer to be incorporated into CZTSe in the copper sublattice as Li^0_{Cu}, Na^0_{Cu} and K^0_{Cu} substitutional defects. These defects are charge neutral, because all group-I dopants are highly electropositive monovalent elements, and they are substituting a monovalent Cu atom. For Li^0_{Cu}, Na^0_{Cu} and K^0_{Cu}, our computed formation energies are -1.53 eV, -1.56 eV and -0.23 eV, respectively. The negative formation energies of these defects indicate that at low concentrations it is energetically favorable to incorporate Li, Na and K impurities into V_{Cu} defects. Moreover, since the formation energies of the Li^0_{Cu} and Na^0_{Cu} are more than 1.3 eV lower than K^0_{Cu}, if a Cu site is already occupied by Li or Na, then K most likely cannot kick out Li or

Na to take their place. For the $CuInSe_2$ light absorber we have obtained qualitatively similar conclusions for the exchange between Na_{Cu} and K_{Cu} [164]. These point defects stay neutral for the whole range of the chemical potential of the electrons across the bandgap from VBM to CBM. Thus, these defects do not act as donors/acceptors and at the same time they do not create gap states either.

It is noteworthy to mention that in CZTSe we are dealing with two kinds of Cu positions in contrast to CISe, due to the lower symmetry of CZTSe compared to CISe. Because of the lower symmetry and the different free structure parameters, although both types of Cu sites are coordinated by four selenium atoms, half of them are located close to the four next neighbor zinc atoms, and the other half of the Cu sites are closer to the four next neighbor Sn atoms. For the intrinsic defect V_{Cu}, the formation energies differ only by about 50 meV for the two types of copper vacancies. For extrinsic defects and especially K-related defects, however, it does matter which Cu site we are considering. When K occupies a Cu site which is closer to four Zn atoms, its formation energy is about 220 meV lower than the formation energy of K_{Cu} which is closer to four Sn atoms. This difference for Na impurity is about 75 meV. In this work whenever I discuss the Cu-related defects in CZTSe, I am referring to the more stable site, which is located near to four Zn atoms rather than four Sn atoms.

Given the high formation energy of 1.58 eV for K^{-}_{Zn}, the formation of a K substitutional defect in a Zn position is not likely. In contrast to K^{-}_{Zn}, the formation energies of 0.02 eV and 0.34 eV computed for Li^{-}_{Zn} and Na^{-}_{Zn}, respectively, suggest that such substitutional defects might form, unlike their K-related counterparts. The formation energy of the studied group-I dopants in the Zn position decreases when μ_e increases and these point defects are more stable in the p-type material. These point defects act as acceptors and increase the density of the holes in the valence band of CZTSe. Similar to the interstitial defects, these point defects create no gap state. The other acceptor point defects are Sn-related defects that can have a wide range of stable charge states and their formation energy drops rapidly as μ_e increases. Since the light absorber layers are grown under p-type conditions, the role of Li_{Sn}, Na_{Sn} and K_{Sn} should be negligible in the films used for actual solar cells. The formation energy of Sn-related defects compete

Table 4.3: Defect formation energy (in eV) calculated by HSE06 using 27% of exact exchange for Li, Na and K incorporation in a 216-atom supercell of CZTSe near the valence band maximum (VBM), assuming a p-type material.

Defect	$Cu_2ZnSnSe_4$
Li^0_{Cu}	-1.53
Na^0_{Cu}	-1.56
K^0_{Cu}	-0.23
Li^-_{Sn}	1.28
Na^0_{Sn}	1.40
K^0_{Sn}	2.40
Li^-_{Zn}	0.02
Na^-_{Zn}	0.12
K^-_{Zn}	1.52
Li^0_{Se}	1.62
Na^0_{Se}	1.19
K^0_{Se}	2.56
Li^+_{oc}	-1.49
Na^+_{oc}	-1.27
K^+_{oc}	1.11
Li^+_{tc}	-1.51
Na^+_{tc}	-1.54
K^+_{tc}	0.60
$(Li\text{-}Li)^+_{Cu}$	-2.81
$(Na\text{-}Na)^+_{Cu}$	-3.35
$(Na\text{-}K)^+_{Cu}$	-1.95
$(K\text{-}K)^+_{Cu}$	-0.61

with interstitial defects in an extremely n-type CZTSe. While Zn-related defects do not create gap states, Sn-related defects cause the appearance of several gap states for different values of the chemical potential of the electrons. Regarding the Se site, my data shows that Na and K-related substitutional defects at the Se site in CZTSe have similar formation energies computed for substitutional defects in the $CuInSe_2$ thin film solar cell material [158,164]. The qualitatively and quantitatively similar results clearly show that Se-related substitutional defects are energetically rather unfavorable both in CZTSe and $CuInSe_2$. The Li_{Se} point defect with the formation energy of 1.62 eV is neutral over the bandgap; its formation energy is higher than all other point defects and it does not create a gap state [165].

Concerning the charge state of the defects, as one would expect, acceptor defects such as Na^{-}_{Zn} and Na^{3-}_{Sn} form more easily in a n-type material, where μ_e is at the CBM. Conversely, donor defects such as Na^{+}_{tc} form more easily in a p-type material where μ_e is at the VBM.

4.3.3 Li, Na and K Dumbbells in $Cu_2ZnSnSe_4$

In addition to the point defects, I have also looked into the formation of four types of dumbbells in CZTSe, namely (Li-Li), (Na-Na), (Na-K) and (K-K) dumbbells located in a copper site. Similar to Na and K, Li atoms can form dumbbells and occupy the vacant Cu sites. The $(\text{Li-Li})^{+}_{Cu}$ defect with the charge state of +1 for the whole range of μ_e is very stable, more stable than all the Li-related point defects (see Figure 4.10). It should be noted that two separate Li_{Cu} and $(\text{Li-Li})_{Cu}$ have the same formation energy in p-type CZTSe. When μ_e increases the formation of two separate Li_{Cu} is more likely than the formation of a dumbbell [165], i. e. in a p-type material dumbbells are preferred over spatially separated substitutional defects. The data presented in Figures 4.11 and 4.12 show that the formation of $(\text{Na-Na})^{+}_{Cu}$, $(\text{Na-K})^{+}_{Cu}$, and $(\text{K-K})^{+}_{Cu}$ dumbbells with the respective formation energies of -3.18 eV, -1.95 eV and -0.66 eV are also highly probable in CZTSe, similar to $CuInSe_2$ [158, 164]. The (Na-Na) dumbbells are the most stable defects over the whole range of the chemical potential of the electrons μ_e. For (Na-K)

and (K-K) as the system becomes more n-type, the Na^0_{Cu} and K^0_{Cu} substitutional defects will become more stable. Comparing the formation energies of a $(Na\text{-}Na)^+_{Cu}$ dumbbell (-3.18 eV) with two Na in two distinct and spatially well separated copper positions (-2.84 eV) unveils that for the p-type system it is more favorable to cluster two Na atoms together, probably to lower the strain in the material. A comparison between the formation energy of a $(K\text{-}K)^+_{Cu}$ dumbbell and two K_{Cu} point defects reveals that K atoms behave in the same way as Na: K impurities also have the preference to form dumbbells instead of occupying two distinct substitutional Cu positions.
Regarding the most stable charge state of Na- and K-related dumbbells, I found a qualitative difference between $CuInSe_2$ and CZTSe. Namely, while in the former compound dumbbells with the charge state +2 are stable [164] at the VBM, in CZTSe the +1 charged dumbbells are stable for the whole range of μ_e.

4.3.4 Band Structure and Charge Transition Levels in $Cu_2ZnSnSe_4$

In this section I discuss the effect of the defects upon the electronic structure of CZTSe. Since the band structure calculations with hybrid functionals are computationally extremely demanding, these calculations have been performed for a smaller 64-atom supercell employing the same methodology as described in the computational details. Figure 4.13 shows the band structure of the defect-free CZTSe bulk and native defects. While the Sn vacancy creates a gap state, other intrinsic defects induce no gap state. The charge transition level calculations for the large 216-atom supercell show that Se and Sn vacancies create gap states but Cu and Zn vacancies do not induce gap states. I note in passing that the discrepancy between band structure calculations and charge transition levels can have several origins. One reason is the difference between the supercell sizes. Band structure calculations are performed for 64-atom supercells, where there is a considerable interaction between a defect and its periodic replica. For comparison, the charge transition levels are calculated for supercells with 216 atoms. The other reason has to deal with the position of the orbitals that might be placed wrong

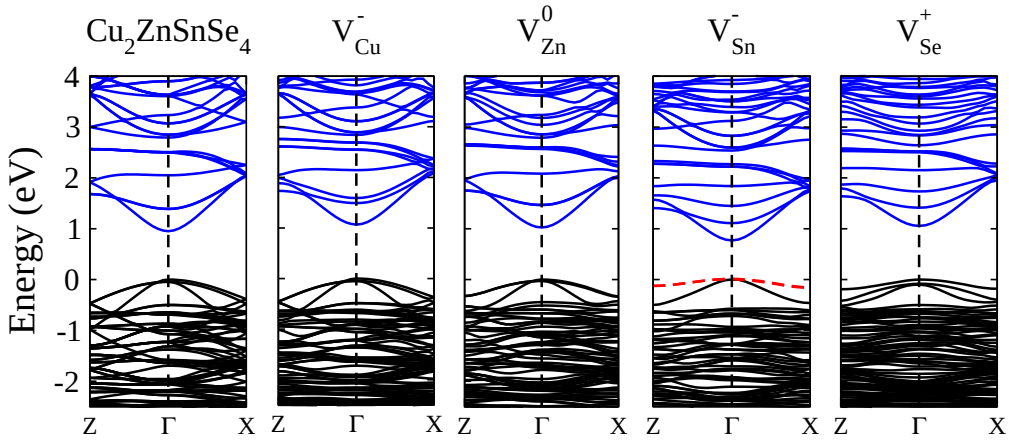

Figure 4.13: Band structure for the bulk CZTSe and pristine defects in CZTSe. The occupied bands are drawn in black and the unoccupied band are shown in blue. The red dashed line represents the defect level.

by DFT [166].

Figure 4.14 depicts the band structures calculated for the Li^{0}_{Cu}, Na^{0}_{Cu}, K^{0}_{Cu}, Li^{-}_{Zn}, Na^{-}_{Zn}, K^{-}_{Zn}, Li^{-}_{Sn}, Na^{3-}_{Sn}, K^{3-}_{Sn}, Li^{0}_{Se}, Na^{-}_{Se}, K^{-}_{Se}, Li^{+}_{tc}, Na^{+}_{tc} and K^{+}_{tc} defects. The band structures show that Na_{Se} and K_{Se} together with Na_{Sn} and K_{Sn} are responsible for introducing a defect level within the band gap. However, due to the high formation energy of such defects, one expects that Na and K impurities in Se and Sn substitutional positions play a negligible role in the efficiency of solar cells based on CZTSe. The charge transition levels calculated for the large 216-atom supercell reveal that only Sn-related defects have transition levels located close to the middle of the band gap. Therefore, they could act as a trap for charge carriers in CZTSe and become detrimental for the device performance. Li_{Sn} induces deep (0/-) and (-/2-) transition levels which are located at 0.51 eV and 0.58 eV above the VBM respectively. Na_{Sn} exhibit three transition levels: the ϵ(0/-) level around E_{VBM}+0.17 eV, the (-/-2) level close to E_{VBM}+0.55 eV that is a deep level, and the (-2/-3) level near E_{VBM}+0.87 eV. K_{Sn} also shows three transition levels within the band gap: (0/-), (-/-2) and (-2/-3) which are located at E_{VBM}+0.39 eV, E_{VBM}+0.45 eV and E_{VBM}+0.9 eV, respectively. Hence, these defects are detrimental for the efficiency of the CZTSe thin film solar cell devices. Other Na- and K-related defects do not show any charge transition levels and therefore they do not act as carrier traps.

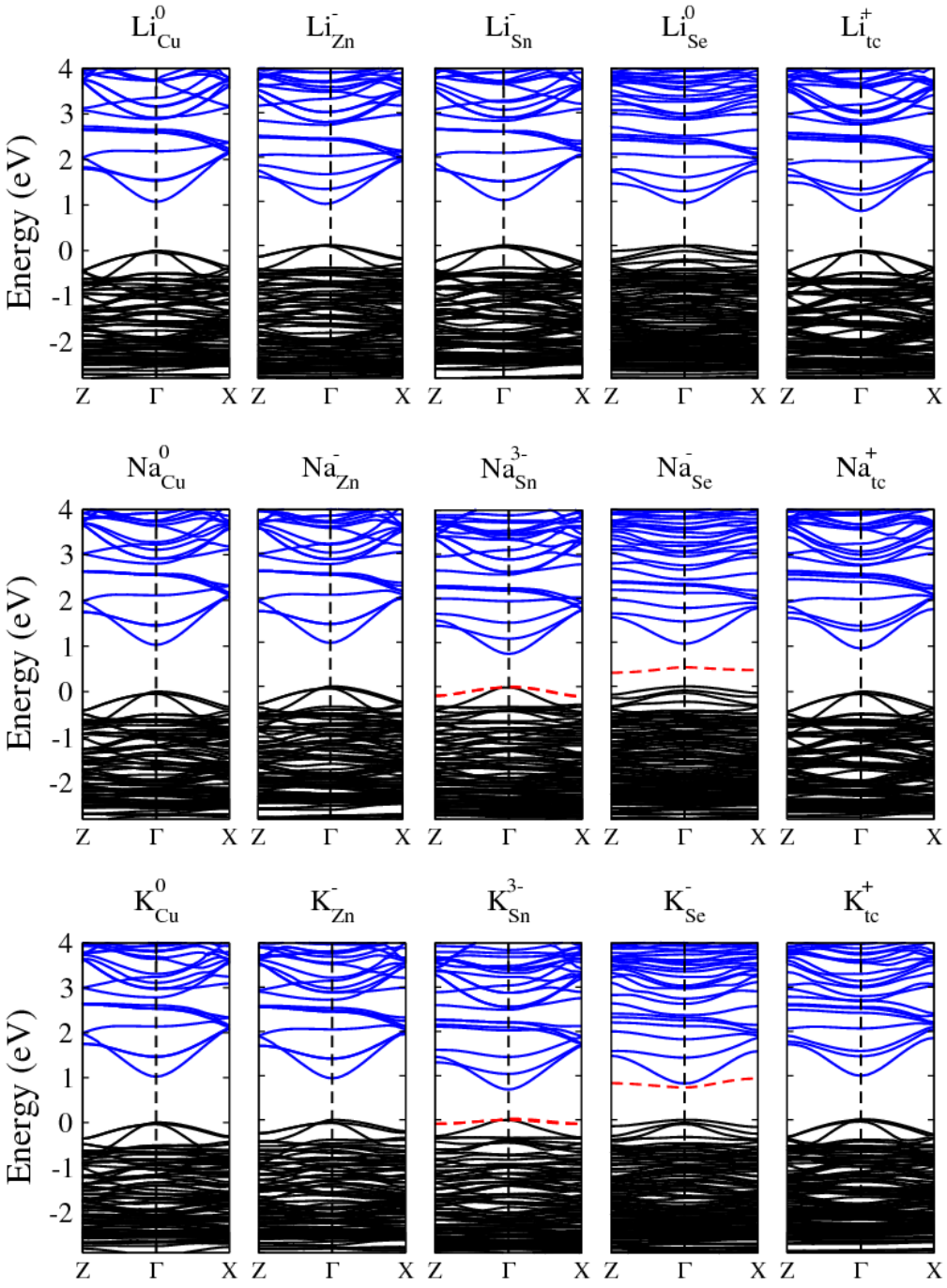

Figure 4.14: The calculated Kohn-Sham band structure for Li-, Na- and K-related defects in CZTSe. The occupied bands are drawn in black and the unoccupied band are drawn in blue. The red dashed lines representhe defect level.

4.4 Diffusion Kinetics

So far in this thesis I have focused on the properties of the static optimized atomic structures of the pristine defects and impurities. However, the diffusion properties of

these defects are another important topic of this thesis, where I investigate the material transport via climbing-image nudged elastic band (CI-NEB) calculations. This way I evaluate the diffusion paths and the barriers involved along these paths on the potential energy surface, which provides an approximate model for the diffusion kinetics at absolute zero temperature (T=0 K). Based on the diffusion kinetics I can provide novel insigths for experimental studies, and I can assess which diffusion processes are more likely to take place under the conditions of the industrial thin film deposition.

Diffusion in solids refers typically to the process of exchanging the sites between atoms. The most common diffusion processes are either vacancy mediated diffusion or interstitial mediated diffusion paths. In a vacancy mediated diffusion process, after getting over an activation barrier, the vacancy exchanges its lattice site with an atom, the atom substitutes the vacancy site and leaves a vacancy behind. Then the new vacancy can exchange its site with another atom if the activation energy could be provided by the external conditions. The product of vacancy concentration, C_{v}, and vacancy diffusivity, D_{v}, represents the probability for the vacancy mediated diffusion path. Concerning the interstitial mediated diffusion process, when an interstitial defect gains enough activation energy it jumps to another interstitial site. After seizing the new interstitial site, the interstitial atom would wait for acquiring the required energy for jumping to the next nearest interstitial position. If C_{i} and D_{i} stand for interstitial concentration and interstitial diffusivity respectively, $C_{\mathrm{i}}\mathrm{D}_{\mathrm{i}}$ indicates the attendance of the interstitial mediated diffusion path.

In the current section of this thesis I discuss the diffusion of pristine vacancies and Na-related impurities in the CISe and CZTSe solar cell materials. The diffusion paths have been modelled through employing the climbing image nudged elastic band (CI-NEB) method (as described earlier in Section 3.6) in a 216-atom supercell of CISe and CZTSe employing a 2x2x2 mesh of k-points for the sampling of the Brillouin zone. The structures on the intermediate images spanning the reaction path have been relaxed until the forces acting on each atom dropped below 0.01 eV/Å. The activation barrier, E_{m}, shows the energy difference on the potential energy landcape between the initial point of the given reaction (referred to as reactant structure) and the saddle point referred

as the transition state (as described earlier in Section 3.2).

4.4.1 Diffusion Kinetics in the CISe Absorber Layer

Here I discuss the activation barriers of four diffusion trajectories in CISe investigated via the CI-NEB method. According to these current CI-NEB calculations, the activation barrier of a copper vacancy in CISe is 1.11 eV. Because of its low activation barrier together with its low formation energy of 1.43 eV, V_{Cu} can mediate the transport of vacancies in $CuInSe_2$ with the activation energy of 2.57 eV at VBM, which drops to 1.52 eV in n-type CISe (see Figure 4.17). As a conclusion, Cu vacancies contribute substantially to the diffusion and accomodation of impurities in the copper sub-lattices. On the other hand, the selenium vacancy, which forms in $CuInSe_2$ in the neutral charge state with formation energy of 2.22 eV has a high diffusion barrier of 2.76 eV. In thermal equilibrium conditions, the activation energy (E_a) is a sum of the defect formation energy (E_f) and its migration barrier (E_m). Therefore, it can be concluded that the migration of V_{Se}, which is shown in Figure 4.15 is highly improbable to take place both in the p-type and in n-type CISe materials. Although the diffusion of selenium vacancies in bulk CISe would be prevented due to its high activation energy, according to References [167, 168] selenium atoms diffuse either in form of dumbbells under Se-rich conditions or through grain boundaries in the polycrystalline materials under the high temperature deposition conditions of the thin film.

Since the formation energy of In-related defects in CISe are very high, the diffusion of In atoms has not been studied in this work. I found, that sodium atoms due to their low

Table 4.4: Activation barriers and formation energies of studied defects in the CISe compound. Formation energies have been calculated for the electronic chemical potential located at the VBM.

Initial	Finial	Charge state	E_m (eV)	E_f
V_{Cu}	V_{Cu}	1-	1.11	1.43
V_{Se}	V_{Se}	0	2.76	2.22
Na_{int}	Na_{int}	1+	0.53	-1.25
Na_{Cu}-V_{Cu}	Na_{Cu}-V_{Cu}	1-	0.35	0.34

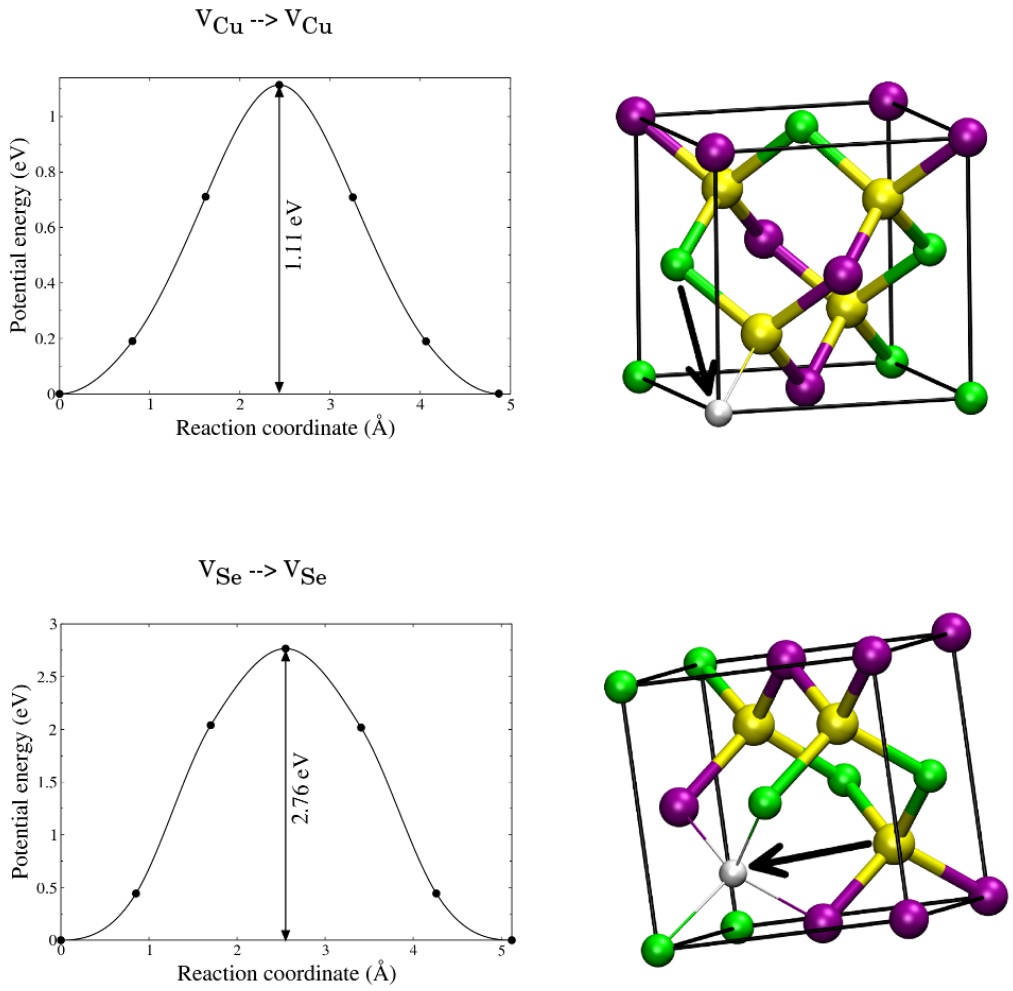

Figure 4.15: Optimized minimum energy paths from CI-NEB along the migration of V_{Cu} and V_{Se} as shown in the left side of the figure. The relative energies of the initial, intermediate and final images are shown with small black circles. The right side of the figure shows the schematic diagram of the corresponding migration path as a black arrow. Vacancies are represented as white spheres, and the other atoms are shown using the same color scheme as in Figure 4.1. For clarity, only one half of a $CuInSe_2$ conventional cell is shown.

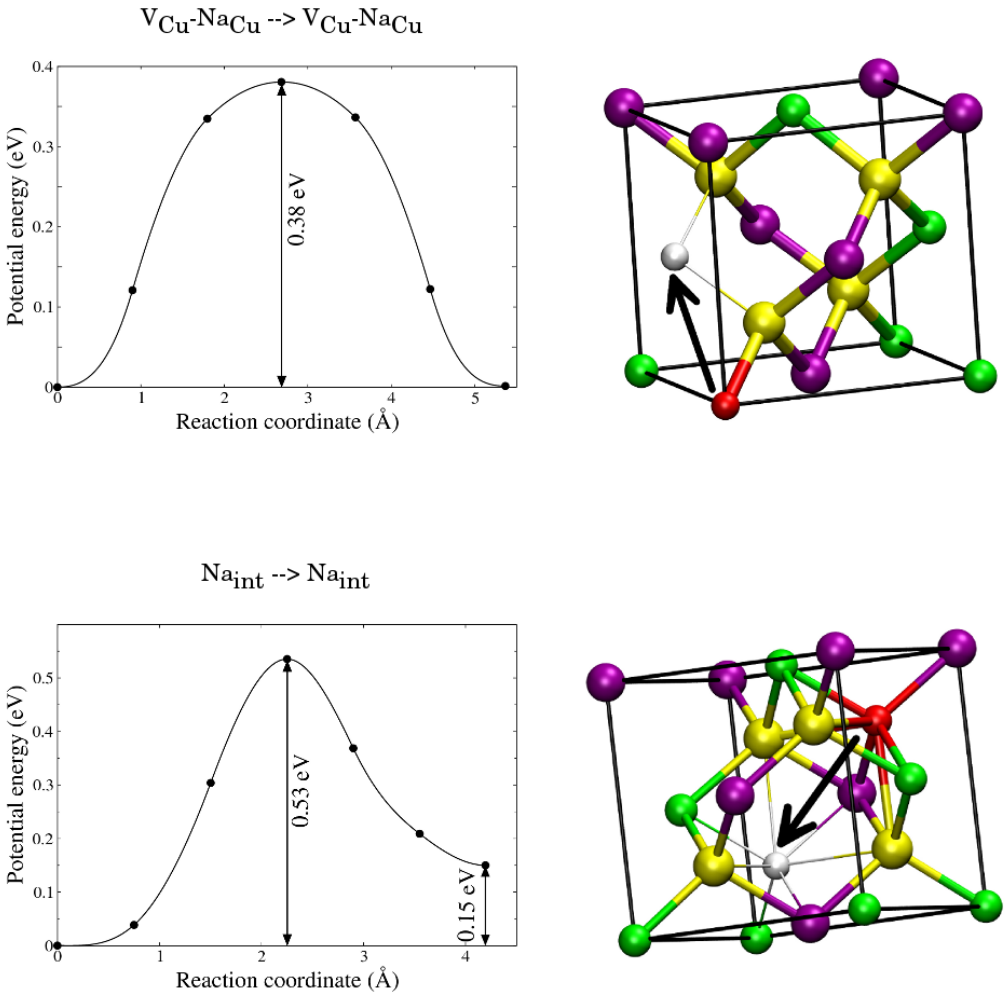

Figure 4.16: CI-NEB calculations presenting the minimum energy path for the migration of the neighbouring $V_{Cu} - Na_{Cu}$ and Na_{int} as shown in the left side of the figure. The relative energies of the initial, intermediate and final images are shown with small black circles. The right side of the figure represents the schematic diagram of the corresponding migration path. Vacancies and Na atoms are shown as white and red spheres, respectively. The other atoms are schematized using the same color scheme as in Figure 4.1. For clarity, only one half of a $CuInSe_2$ conventional cell is shown.

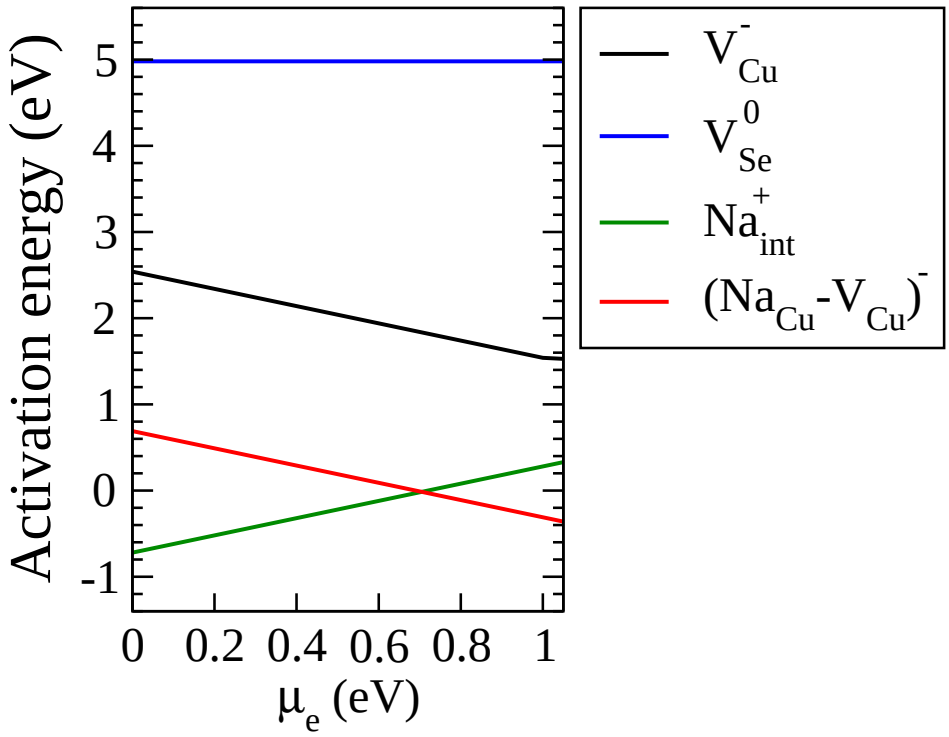

Figure 4.17: Activation energy of the studied point defects in CISe as a function of the electron chemical potential.

formation energies may diffuse with a high probability through the CISe film. I have considered Na_{int}-mediated and V_{Cu}-mediated mechanisms to study and compare the activation barriers along two diffusion paths for sodium. Neighbouring V_{Cu} and Na_{Cu} defects can exchange their positions with remarkably low diffusion barrier of 0.35 eV. Therefore, if V_{Cu} diffuses near a Na_{Cu} substitutional defect, it will probably jump back and forth around the Na_{Cu} instead of exchanging site with an atom from the Cu sublattice. In Section 4.2.1, I have mentioned that Na can occupy an interstitial position coordinated to two Cu and two In atoms with a low formation energy of -1.25 eV. My CI-NEB calculations confirm that the migration of an interstitial Na is highly likely even at relatively low temperatures, because by overcoming the activation energy barrier of 0.53 eV Na can easily jump to an onther position. A Na atom travelling from an interstitial site, which is tetrahedrally coordinated to four cations to a neighbouring equivalent interstitial site have access to another stable interstitial position in the middle of its journey along the diffusion path. In this intermediate interstitial position Na

is trigonally coordinated to three Cu atoms. Since the diffusion path is fully symmetric, in figure 4.16 only one half of the path has been presented between the tetragonally and the trigonally coordinated structures, and from there the path is mirror symmetric going to the other tetrahedral structure. Among the studied diffusion paths for the impurities in $CuInSe_2$, the V_{Cu}-Na_{Cu} and Na_{int} paths (see Figure 4.16) with the respective activation barriers of 0.35 eV and 0.53 eV are found to be the diffusion trajectories with the lowest activation energies, which means that they correspond to fast diffusion processes. According to Figure 4.17, the activation energy for the transfer of Na_{int} is about 1.4 eV smaller than the activation energy of V_{Cu}-Na_{Cu} under p-type conditions. However, in an n-type material the activation energy of Na_{int} rise with 0.33 eV.

4.4.2 Diffusion Kinetics in the CZTSe Absorber Layer

The exploration of the activation barriers at 0 K temperature corresponding to the potential energy differences along the diffusion trajectories of defects and impurities in the CZTSe light absorber are presented in this sub-section. Similar to the calculations performed on CISe, we have used the same methodology in combination with the CI-NEB to search for the transition state between reactant and product configurations. Among native vacancies, the copper vacancy with the charge state of -1 has the lowest activation barrier of 0.96 eV. Regarding the low formation energy of V_{Cu} (1.20 eV), coupled with its low diffusion barrier of 0.96 eV, it can be concluded that similar to CISe, V_{Cu} with the activation energy of 2.16 eV in p-type CZTSe stears the vacancy mediated mass transport mechanism in CZTSe, especially at the elevated temperatures of the film deposition. This activation energy drops to 1.21 eV under n-type conditions (see Figure 4.20). For comparison, the other two vacancies, namely V_{Zn} and V_{Se} with the charge states of -1 and 0, respectively, have a higher diffusion barrier of 1.76 eV and 2.73 eV. The activation energies of V_{Zn} and V_{Se} in p-type CZTSe are 4.34 eV and 4.64 eV respectively, which are considerably higher compared to 1.76 eV and 2.73 eV values in the n-type material. Since selenium defects exist mainly in the neutral charge state, their activation energy remains constant through the whole range of the chemical potential of

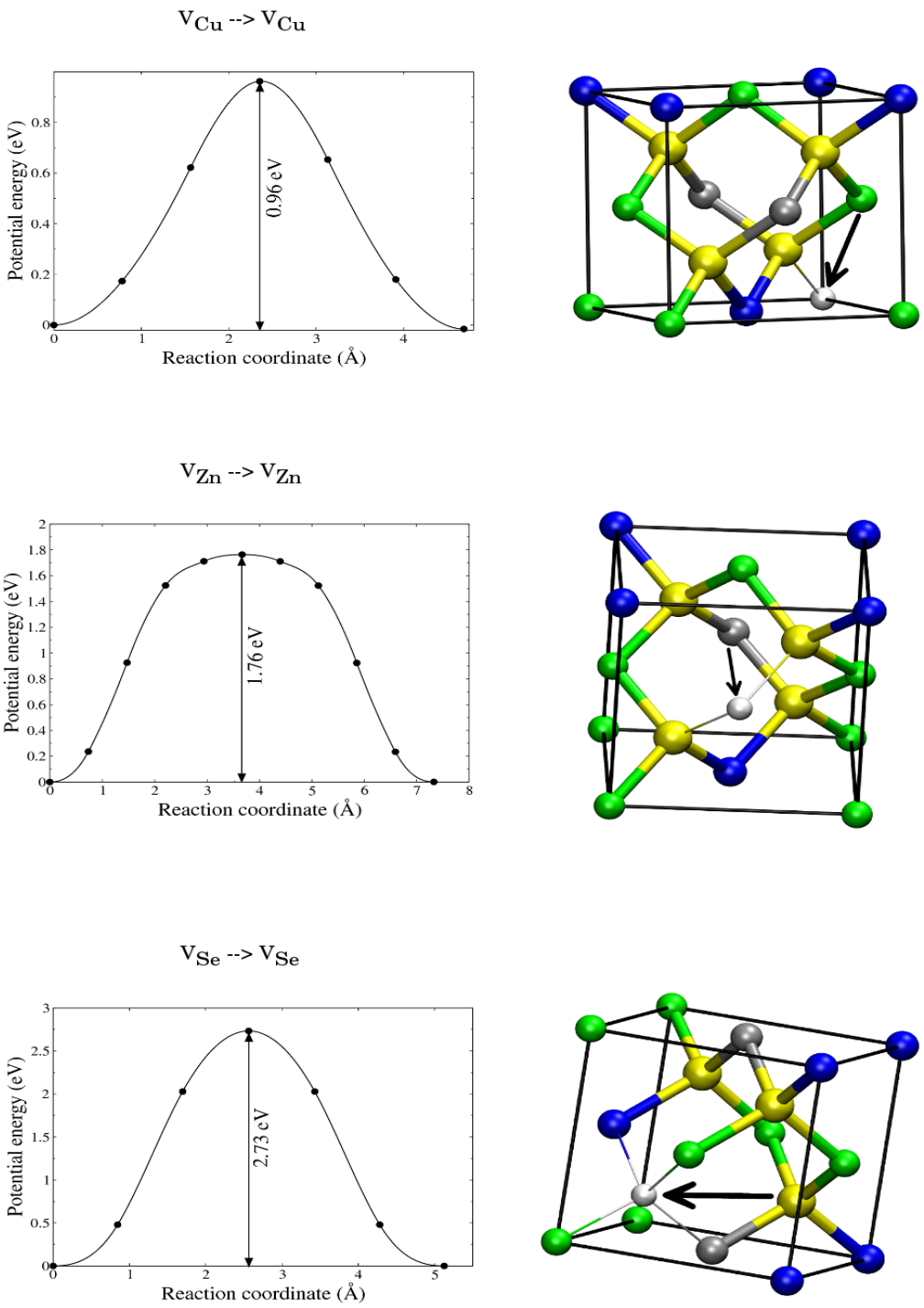

Figure 4.18: Minimum energy paths from CI-NEB calculations investigating the migration of the V_{Cu}, V_{Zn} and V_{Se}. The diffusion paths are presented in the left side of the figure. The right side of the figure shows the schematic diagram of the corresponding migration path.

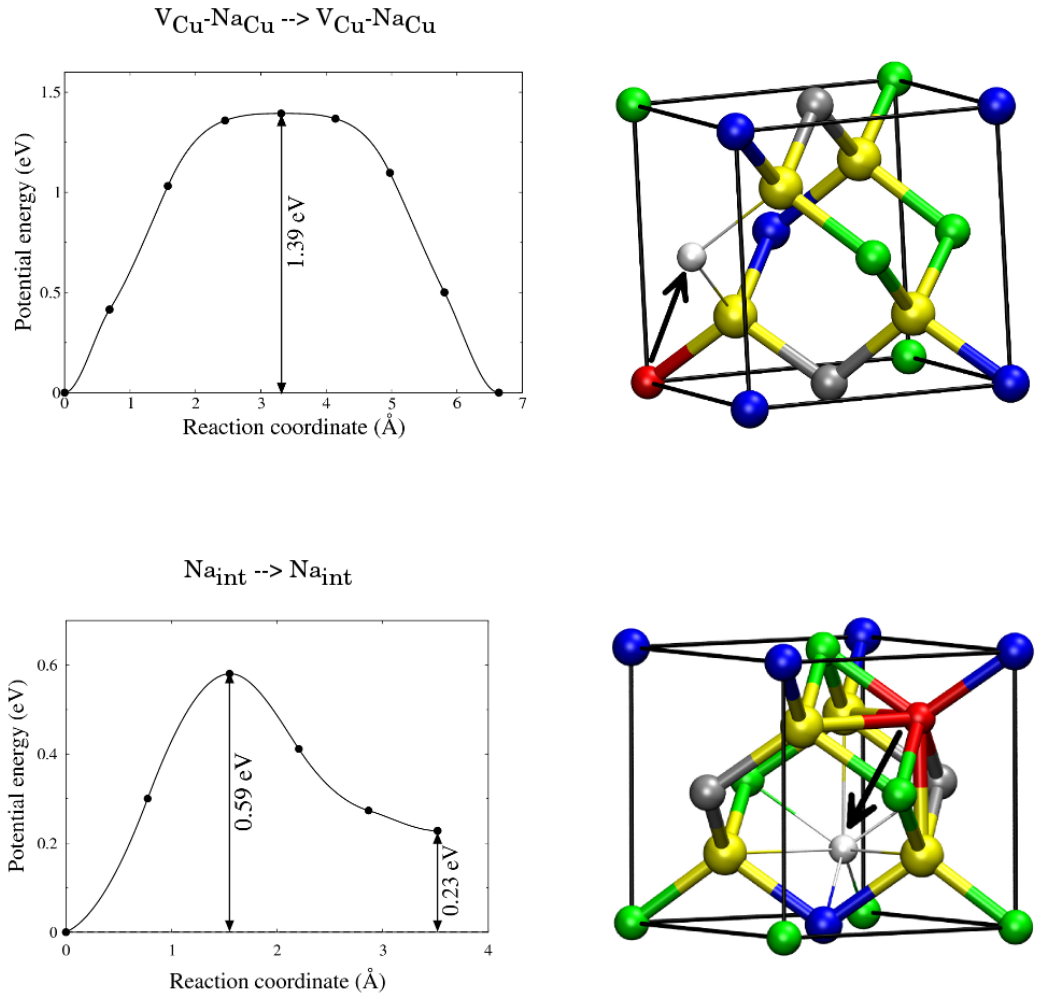

Figure 4.19: Minimum energy paths from CI-NEB calculations for the migration of the neighbouring $V_{Cu} - Na_{Cu}$ and Na_{int} (see the left side of the figure). The right side of the figure depicts the schematic diagram of the corresponding migration path in form of a black arrow.

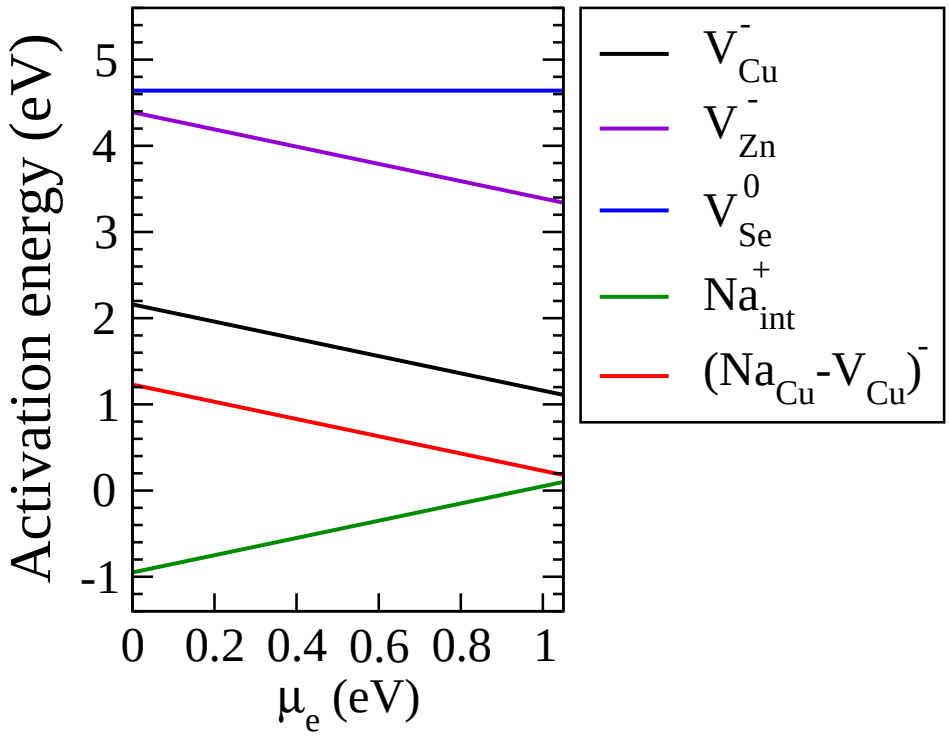

Figure 4.20: Activation energy of the studied point defects in CZTSe shown for the whole range of the Fermi energy.

the electrons μ_e. In contrast, the activation energy of zinc vacancy decreases to 3.39 eV in n-type CZTSe. Based on these results, one can conclude that both selenium and zinc vacancy-mediated mass transports are rather slow processes in the CZTSe material. Due to the large formation energy for V_{Sn} of 4.21 eV in the p-type material I have not studied the diffusion of V_{Sn} in CZTSe, because most probably it will be a very slow process even if the path would be barrierless due to this large energy difference between reactant and product. Similar to CISe, in order to study the diffusion trajectory of Na in

Table 4.5: Activation barriers and formation energies of studied defects in CZTSe. Formation energies have been calculated at μ_e=VBM.

Initial	Finial	Charge state	E_m (eV)	E_f (eV)
V_{Cu}	V_{Cu}	1-	0.96	1.20
V_{Zn}	V_{Zn}	1-	1.76	2.63
V_{Se}	V_{Se}	0	2.73	1.91
Na_{int}	Na_{int}	1+	0.59	-1.54
Na_{Cu}-V_{Cu}	Na_{Cu}-V_{Cu}	1-	1.39	-0.16

CZTSe, I have studied two possible diffusion mechanisms, a Na_{int}-mediated and a V_{Cu}-mediated path. As I already mentioned in Section 4.3.2, there are two distinguishable copper sites in CZTSe. To study the site-exchange between V_{Cu} and Na_{Cu}, I have selected two completely equivalent Cu positions resulting in a fully symmetric path. As a result, the reaction coordinate for this path in CZTSe is longer compared to CISe (see Figures 4.16 and 4.19). In CZTSe, Na_{Cu} has to overcome an activation barrier of 1.39 eV in order to jump to an equivalent copper vacancy. According to the results presented in this thesis, the formation energy of Na_{Cu}-V_{Cu} defect is -0.16 eV under p-type conditions. Therefore, this diffusion path with rather low activation energy of 1.23 eV is feasible at higher temperatures. The migration path of interstitial Na in CZTSe corresponds to the same path as in CISe. Similarly, the interstitial sodium that is jumping between two equivalent tetrahedrally coordinated interstitial sites goes through a metastable intermediate located in the middle of the path before moving to another inequivalent interstitial position. Since the path is mirror symmetric, only one half of the path is shown in Figure 4.19. The migration barrier for Na_{int} is 0.59 eV, so Na intersititals are very mobile even at relatively low temperatures within the whole range of μ_e and its activation energy changes from -0.95 eV at VBM to becoming barrierless at CBM.

Chapter 5

Summary and Conclusions

The rise in energy demand coupled with environmental limitations have highlighted the need for alternative energy resources in recent years. Photovoltaic (PV) is one of the highly competitive and widely deployed alternatives with great potentials for renewable energy applications. Thin film devices have become an important field in PV due to their relatively low fabrication cost and good performance. However, in order to make these solar cells commercially more applicable and competitive, a further boost in their efficiency is becoming apparent. Due to the complex nature of these devices, the experimental efforts to improve the efficiency of these devices based on trial and error procedures is both very much time and resource consuming. Therefore, the assistance for experimental works via theoretical calculations in this field is essential. Furthermore, computer simulations are a befitting support to provide new insights and to improve the explanation of the experimental findings.

In this thesis, the role of Li, Na and K as alkaline impurities in two kinds of thin film solar cell light absorber layers –namely $CuInSe_2$ (CISe) and $Cu_2ZnSnSe_4$ (CZTSe)– have been studied. It is widely accepted that doping these absorber layers with alkaline elements, especially Na and K have a beneficial effect on the performance of the solar cell device. Therefore my thesis is mainly focusing on the incorporation of these impurities into a large variety of sites in these materials from first principles hybrid functional calculations.

In spite of the fact that DFT is a very powerful method in characterizing the features of semiconductor materials, the results are quite often influenced by the particular exchange-correlation functional used in the given study. Since local DFT severely underestimates the band gap of semiconductor materials, I have employed the HSE06 hybrid functional to predict the atomic and electronic structure of the CISe and CZTSe solar cell materials more accurately.

The formation energy calculation of Na and K impurities in CISe reveals that, although Na and K behave somewhat similar, there is a qualitative difference between the inclusion of Na and K impurities. Namely, Na will be mostly incorporated into $CuInSe_2$ and $CuIn_5Se_8$ either as an interstitial defect coordinated by cations, or two Na impurities will form (Na-Na) dumbbells in the Cu sub-lattice. In contrast to Na, K impurities are less likely to form interstitial defects. Instead it is more preferable to accommodate K either as K_{Cu} substitutional defect, or to form (K-K) dumbbells on Cu substitution positions. The data presented in this work show, that all (Na-Na), (Na-K) and (K-K) dumbbells can form in both $CuInSe_2$ and in $CuIn_5Se_8$, which is a Cu-poor phase of $CuInSe_2$. In $CuIn_5Se_8$ the pristine Cu vacancies act as the most stable sites where Na and K can be inserted. The formation energy of Na-related defects is generally lower than the corresponding K-related defects, which would mean that if a defect site is already occupied by Na, then it is less likely that K is able to substitute Na during the post-deposition treatment. Regarding thermodynamic charge transition level calculations, in $CuInSe_2$ Na and K impurities located in the Cu sub-lattice do not create deep defect levels in the gap, so they are not detrimental for the efficiency of the solar cell. In contrast to $CuInSe_2$, in $CuIn_5Se_8$ the formation of Na and especially K substitutional defects in the Cu sub-lattice lead to the creation of defect levels which act as recombination centers, being very detrimental for the efficiency. Se-related substitutional defects introduce defect levels in the gap of both $CuInSe_2$ and $CuIn_5Se_8$, which act as charge traps, leading to severe degradation of the device efficiency. However, the formation energy of these Se-related defects are high, so that they should have a low concentration in the material.

Formation energy calculation for Li, Na and K impurities in the kesterite structure of

the CZTSe shows, that Li, Na and K atoms prefer to be incorporated into this material as substitutional defects in the Cu sub-lattice. At this site highly stable (Li-Li), (Na-Na) and (K-K) dumbbells can form as well. While Li and Na interstitial defects are stable in CZTSe, the formation of K interstitial defects is unlikely. In general, the resulting formation energies for Li and Na-related defects are comparable, and they are always lower compared to their equivalent K-related counterparts. Based on thermodynamic charge transition level calculations one can conclude that the external defects are harmless except Li_{Sn}, Na_{Sn} and K_{Sn}. These defects induce gap states that might be detrimental for the device performance.

In addition to the static structural relaxations and band structure calculations, the migration of point defects in CISe and CZTSe have been also investigated in this thesis. In order to find the minimum energy path between appointed initial and final states in a chemical reaction, corresponding to reactant and product states, I have utilized the climbing image nudged elastic band (CI-NEB) method. The activation barrier has been calculated by subtracting the energy of the saddle point from the energy of the reactant configuration. The CI-NEB calculations reveal that in both CISe and CZTSe, the V_{Cu} native defect due to its relatively low diffusion barrier easily contributes to the vacancy mediated mass transport mechanism. In contrast, the diffusion of V_{Se} requires overcoming a higher activation barrier. In CZTSe, the migration barrier of V_{Zn} diffusion is about 1 eV lower than the barrier for V_{Se} diffusion. However, considering its high formation energy, it can be concluded that the diffusion of V_{Zn} to a neighbouring Zn sub-lattice is highly unlikely. Modelling the diffusion of Na interstitials reveals that they have a very low activation barrier both in the CISe and CZTSe materials. Therefore, the migration of Na_{int} is very likely even at relatively low temperatures. Studying another diffusion path, which shows a site exchange between V_{Cu} and Na_{Cu} displays a sharp contrast between CISe and CZTSe. Namely, when V_{Cu} and Na_{Cu} are inserted at two equivalent Cu sub-lattice sites in CISe, the exchange between the sites would require a very low activation barrier of 0.35 eV. For comparison, in CZTSe this barrier is around 1 eV higher (1.39 eV).

The aim of this thesis was to present a comprehensive insight on the favourable and

detrimental inclusion sites for impurities in two absorber layers of thin film solar cells. In this work I have provided new data for the understanding of the structure and energetics of Na and K impurities in CISe and of Li, Na and K impurities in CZTSe. Since point defects can affect the material growth through mediating diffusion, the diffusion mechanisms presented in this thesis can provide helpful explanation for future experimental observations.

List of Figures

List of Tables

Acknowledgment

At the end I would like to thank all the people who made this work feasible with their help, guidance, encouragement and criticism.
First of all, I would like to express my deepest gratitude to Prof. Dr. Claudia Felser from Max Planck Institute for Chemical Physics of Solid for giving me the opportunity to join her group and providing me with her continuous support and encouragement.
I would like to express my sincere appreciation to Prof. Dr. Thomas Kühne from university of Paderborn who kindly accepted to be the co-supervisor of this thesis and for his excellent supervision. He has closely followed my work through every step and has opened new points of view to me in our regular discussions.
I would like to express profound thanks to my colleagues especially Dr. Janos Kiss and Dr. Guido Roma for their professional experience, advice and time.
I would like to thank Dr. Markus Schmidt, Dr. Hossein Mirhosseini, Dr. Thomas Spura and Kristof Karhan for proof-reading parts of this thesis.
Of course, I am thankful to the technical and administration staff at the Department of Chemistry for their support.
I would also like to acknowledge the IBM Mainz for the work proposal and for the computing resources. Financial support is gratefully acknowledged from the Bundesministerium für wirtschaft und Energie (BMWi) for the comCIGS-II project.
Last but not least I would like to thank my husband, Wahid, who did not stop supporting me even for a moment. Thank you my dearest.

Thank you, everyone!

Bibliography

[1] Martin A. Green, Keith Emery, Yoshihiro Hishikawa, Wilhelm Warta, and Ewan D. Dunlop. Solar cell efficiency tables (version 47). *Prog. Photovoltaics: Res. Appl.*, 24(1):3, 2016.

[2] S. M. Sze and K. K. Ng. *Physics of Semiconductor Devices*. John Wiley & Sons, Inc., 2006.

[3] Philip Jackson, Dimitrios Hariskos, Erwin Lotter, Stefan Paetel, Roland Würz, Richard Menner, Wiltraud Wischmann, and Michael Powalla. New world record efficiency for Cu(In,Ga)Se_2 thin-film solar cells beyond 20%. *Prog. Photovoltaics: Res. Appl.*, 19(7):894, 2011.

[4] R. Wuerz, A. Eicke, F. Kessler, S. Paetel, S. Efimenko, and C. Schlegel. CIGS thin-film solar cells and modules on enamelled steel substrates. *Sol. Energy Mater. Sol. Cells*, 100:132, 2012.

[5] K. Ramanathan, M. A. Contreras, C. L. Perkins, S. Asher, F. S. Hasoon, J. Keane, D. Young, M. Romero, W. Metzger, R. Noufi, J. Ward, and A. Duda. Properties of 19.2% efficiency ZnO/CdS/$CuInGaSe_2$ thin film solar cells. *Prog. Photovoltaics: Res. Appl.*, 11:225, 2003.

[6] K. Orgassa, H.W. Schock, and J.H. Werner. Alternative back contact materials for thin film Cu(In,Ga)Se_2 solar cells. *Thin Solid Films*, 431-432:387, 2003. Proceedings of Symposium B, Thin Film Chalcogenide Photovoltaic Materials, E-MRS Spring Meeting.

[7] Yoshinori Nagoya, Katsumi Kushiya, Muneyori Tachiyuki, and Osamu Yamase. Role of incorporated sulfur into the surface of Cu(InGa)Se_2 thin-film absorber. *Sol. Energy Mater. Sol. Cells*, 67(1-4):247, 2001.

[8] V. Alberts, J. Titus, and R.W. Birkmire. Material and device properties of single-phase Cu(In,Ga)(Se,S)$_2$ alloys prepared by selenization/sulfurization of metallic alloys. *Thin Solid Films*, 451-452:207, 2004.

[9] Sachin S. Kulkarni, Galymzhan T. Koishiyev, Helio Moutinho, and Neelkanth G. Dhere. Preparation and characterization of $CuIn_{(1-x)}Ga_xSe_{(2-y)}S_y$ thin film solar cells by rapid thermal processing. *Thin Solid Films*, 517(7):2121, 2009.

[10] C. J. Hibberd, E. Chassaing, W. Liu, D. B. Mitzi, D. Lincot, and A. N. Tiwari. Non-vacuum methods for formation of Cu(In, Ga)(Se, S)$_2$ thin film photovoltaic absorbers. *Prog. Photovoltaics: Res. Appl.*, 18(6):434, 2010.

[11] Qing Cao, Oki Gunawan, Matthew Copel, Kathleen B. Reuter, S. Jay Chey, Vaughn R. Deline, and David B. Mitzi. Defects in Cu(In,Ga)Se_2 chalcopyrite semiconductors: A comparative study of material properties, defect states, and photovoltaic performance. *Adv. Energy Mater.*, 1(5):845, 2011.

[12] Alexander R. Uhl, Carolin Fella, Adrian Chirila, Marc R. Kaelin, Lassi Karvonen, Anke Weidenkaff, Camelia N. Borca, Daniel Grolimund, Yaroslav E. Romanyuk, and Ayodhya N. Tiwari. Non-vacuum deposition of Cu(In,Ga)Se_2 absorber layers from binder free, alcohol solutions. *Prog. Photovoltaics: Res. Appl.*, 20(5):526, 2012.

[13] J. Rappich, M. Aggour, S. Rauscher, H.J. Lewerenz, and H. Jungblut. Electrochemical surface conditioning of n-Si(111). *Surf. Sci.*, 335:160, 1995. Proceedings of the IUVSTA Workshop on Surface Science and Electrochemistry.

[14] T. Tinoco, C. Rincon, M. Quintero, and G. Sanchez Perez. Phase diagram and optical energy gaps for $CuIn_yGa_{(1-y)}Se_2$ alloys. *Phys. Status Solidi A*, 124(2):427, 1991.

[15] Shota Minoura, Keita Kodera, Takuji Maekawa, Kenichi Miyazaki, Shigeru Niki, and Hiroyuki Fujiwara. Dielectric function of Cu(In,Ga)Se_2-based polycrystalline materials. *J. Appl. Phys.*, 113(6):063505, 2013.

[16] M. I. Alonso, K. Wakita, J. Pascual, M. Garriga, and N. Yamamoto. Optical functions and electronic structure of $CuInSe_2$, $CuGaSe_2$, $CuInS_2$ and $CuGaS_2$. *Phys. Rev. B*, 63:075203, Jan 2001.

[17] M.I. Alonso, M. Garriga, C.A. Durante Rincon, E. Hernandez, and M. Leon. Optical functions of chalcopyrite $CuGa_xIn_{(1-x)}Se_2$ alloys. *Appl. Phys. A*, 74(5):659, 2002.

[18] M. Turcu and U. Rau. Compositional trends of defect energies, band alignments, and recombination mechanisms in the Cu(In,Ga)$(Se,S)_2$ alloy system. *Thin Solid Films*, 431-432:158, 2003.

[19] P. D. Paulson, R. W. Birkmire, and W. N. Shafarman. Optical characterization of $CuIn_{(1-x)}Ga_xSe_2$ alloy thin films by spectroscopic ellipsometry. *J. Appl. Phys.*, 94(2):879, 2003.

[20] Sung-Ho Han, Falah S. Hasoon, Joel W. Pankow, Allen M. Hermann, and Dean H. Levi. Effect of Cu deficiency on the optical bowing of chalcopyrite $CuIn(1-x)Ga_xSe_2$. *Appl. Phys. Lett.*, 87(15):151904, 2005.

[21] Kentaro Ito and Tatsuo Nakazawa. Electrical and optical properties od stannite-type quaternary semiconductor thin films. *Jpn. J. Appl. Phys.*, 27:2094, 1988.

[22] Wei Wang, Mark T. Winkler, Oki Gunawan, Tayfun Gokmen, Teodor K. Todorov, Yu Zhu, and David B. Mitzi. Device characteristics of CZTSSe thin-film solar cells with 12.6% efficiency. *Adv. Energy Mater.*, 4(7):1301465, 2014.

[23] H. W. Spiess, U. Haeberlen, G. Brandt, A. Räuber, and J. Schneider. Nuclear magnetic resonance in IB-III-VI2 semiconductors. *Phys. Status Solidi B*, 62(1):183, 1974.

[24] JE. Jaffe and A. Zunger. Electronic structure of the ternary chalcopyrite semiconductors $CuAlS_2$, $CuGaS_2$, $CuInS_2$, $CuAlSe_2$, $CuGaSe_2$, and $CuInSe_2$. *Phys. Rev. B*, 28:5822, 1983.

[25] H. Mönig, Ch. H. Fischer, R. Caballero, C. A. Kaufmann, N. Allsop, M. Gorgoi, R. Klenk, H. W. Schock, S. Lehmann, M. C. Lux-Steiner, and I. Lauermann. Surface Cu depletion of $Cu(In,Ga)Se_2$ films: An investigation by hard X-ray photoelectron spectroscopy. *Acta Materialia*, 57:3645, 2009.

[26] S. B. Zhang, Su-Huai Wei, Alex Zunger, and H. Katayama-Yoshida. Defect physics of the $CuInSe_2$ chalcopyrite semiconductor. *Phys. Rev. B*, 57:9642, 1998.

[27] S. B. Zhang, S. H. Wei, and A. Zunger. Stabilization of ternary compounds via ordered arrays of defect pairs. *Phys. Rev. Lett.*, 78:4059, 1997.

[28] D. Schmid, M. Ruckh, F. Grunwald, and H. W. Schock. Chalcopyrite/defect chalcopyrite heterojunctions on the basis of $CuInSe_2$. *J. Appl. Phys.*, 73(6):2902, 1993.

[29] Shiyou Chen, X. G. Gong, Aron Walsh, and Su-Huai Wei. Crystal and electronic band structure of Cu_2ZnSnX_4 (X=S and Se) photovoltaic absorbers: First-principles insights. *Appl. Phys. Lett.*, 94(4):041903, 2009.

[30] D. S. Su and Su-Huai Wei. Transmission electron microscopy investigation and first-principles calculation of the phase stability in epitaxial $CuInS_2$ and $CuGaSe_2$ films. *Appl. Phys. Lett.*, 74(17):2483, 1999.

[31] R. Magri, S.-H. Wei, and Alex Zunger. Ground-state structures and the random-state energy of the madelung lattice. *Phys. Rev. B*, 42:11388, Dec 1990.

[32] James E. Bernard, L. G. Ferreira, S. H. Wei, and Alex Zunger. Ordering of isovalent intersemiconductor alloys. *Phys. Rev. B*, 38:6338, Sep 1988.

[33] S. Schorr. Structural aspects of adamantine like multinary chalcogenides. *Thin Solid Films*, 515(15):5985, 2007.

[34] A neutron diffraction study of the stannite-kesterite solid solution series. *Eur. J. Mineral.*, 19(1):65, 2007.

[35] Shiyou Chen, Aron Walsh, Ji-Hui Yang, X. G. Gong, Lin Sun, Ping-Xiong Yang, Jun-Hao Chu, and Su-Huai Wei. Compositional dependence of structural and electronic properties of $Cu_2ZnSn(S,Se)_4$ alloys for thin film solar cells. *Phys. Rev. B*, 83:125201, 2011.

[36] David B. Mitzi, Oki Gunawan, Teodor K. Todorov, Kejia Wang, and Supratik Guha. The path towards a high-performance solution-processed kesterite solar cell. *Solar Energy Materials and Solar Cells*, 95(6):1421, 2011. Special Issue : Thin film and nanostructured solar cells.

[37] B. E. McCandless and S. S. Hegedus. Influence of CdS window layer on thin film CdS/CdTe solar cell performance. *22th IEEE Photovoltaics Spec. Conf.*, page 967, 1999.

[38] K.M. Hynes and J. Newham. *16th Eur. photovoltaics Solar Energy Conf.*, page 2297, 2000.

[39] K. Orgassa, Uwe Rau, Quang Nguyen, Hans Werner Schock, and Jürgen H. Werner. Role of the CdS buffer layer as an active optical element in $Cu(In,Ga)Se_2$ thin-film solar cells. *Prog. Photovoltaics: Res. Appl.*, 10(7):457, 2002.

[40] Sylvie Faye, Jerome Steinhauser, Nuno Oliveira, Evelyne Vallat-Sauvain, and Christophe Ballif. Opto-electronic properties of rough LP-CVD ZnO:B for use as TCO in thin-film silicon solar cells. *Thin Solid Films*, 515(24):8558, 2007. First International Symposium on Transparent Conducting Oxides.

[41] Jean Rousset, Edgardo Saucedo, Konrad Herz, and Daniel Lincot. High efficiency CIGS based solar cells with electrodeposited ZnO:Cl as transparent conducting oxide front contact. *Prog. Photovoltaics: Res. Appl.*, 19(5):537, 2011.

[42] Sophie Peulon and Daniel Lincot. Cathodic electrodeposition from aqueous solution of dense or open-structured zinc oxide films. *Adv. Mater.*, 8(2):166, 1996.

[43] Ingrid Repins, Miguel A. Contreras, Brian Egaas, Clay DeHart, John Scharf, Craig L. Perkins, Bobby To, and Rommel Noufi. 19.9% efficient ZnO/CdS/$CuInGaSe_2$ solar cell with 81.2% fill factor. *Prog. Photovoltaics: Res. Appl.*, 16(3):235, 2008.

[44] Nawalage F. Cooray, Katsumi Kushiya, Atsushi Fujimaki, Ichiro Sugiyama, Tadayuki Miura, Daisuke Okumura, Masao Sato, Mineo Ooshita, and Osamu Yamase. Large area ZnO films optimized for graded band-gap Cu(InGa)Se_2-based thin-film mini-modules. *Sol. Energy Mater. Sol. Cells*, 49(1-4):291, 1997.

[45] R. J. D. Tilley. *Defects in Solids.* John Wiley & Sons, 2008.

[46] Chris G. Van de Walle and Anderson Janotti. Advances in electronic structure methods for defects and impurities in solids. *Phys. Status Solidi B*, 248(1):19, 2011.

[47] Chris G. Van de Walle and Joerg Neugebauer. First-principles calculations for defects and impurities: Applications to III-nitrides. *J. Appl. Phys.*, 95(8):3851, 2004.

[48] David A. Drabold and Stefan K Estreicher. *Theory of Defects in Semiconductors.* Springer-Verlag, 2007.

[49] Jonas Hedstrom, H. Ohlsen, M. Bodegard, A Kylner, Lars Stolt, D. Hariskos, Martin Ruckh, and H. Schock. ZnO/CdS/ Cu(In,Ga)Se_2 thin film solar cells with improved performance. In *Photovoltaic Specialists Conference, 1993., Conference Record of the Twenty Third IEEE*, page 364, May 1993.

[50] A. Chirila, P. Reinhard, F. Pianezzi, P. Bloesch, A. Uhl, C. Fella, L. Kranz, D. Keller, C. Gretener, H. Hagendorfer, D. Jaeger, R. erni, S. Nishiwaki, S. Buecheler, and A. N. Tiwari. Potassium-induced surface modification of Cu(In,Ga)Se_2 thin films for high-efficiency solar cells. *Nat. Mater.*, 12:1107, 2013.

[51] D. Rudmann, A. F. da Cunha, M. Kaelin, F. Kurdesau, H. Zogg, A. N. Tiwari, and G. Bilger. Efficiency enhancement of Cu(In,Ga)Se_2 solar cells due to post-deposition Na incorporation. *Appl. Phys. Lett.*, 84(7):1129, 2004.

[52] Anke Lämmle, Roland Würz, and Michael Powalla. Efficiency enhancement of Cu(In,Ga)Se_2 thin-film solar cells by a post-deposition treatment with potassium fluoride. *Phys. Status Solidi (RRL) - Rapid Res. Lett.*, 7(9):631, 2013.

[53] Pyuck-Pa Choi, Oana Cojocaru-Miredin, Roland Wuerz, and Dierk Raabe. Comparative atom probe study of Cu(In,Ga)Se_2 thin-film solar cells deposited on soda-lime glass and mild steel substrates. *J. Appl. Phys*, 110(12):124513, 2011.

[54] Ralf Schlesiger, Christian Oberdorfer, Roland Würz, Gerd Greiwe, Patrick Stender, Michael Artmeier, Patrick Pelka, Frank Spaleck, and Guido Schmitz. Design of a laser-assisted tomographic atom probe at münster university. *Rev. Sci. Instrum.*, 81(4):043703, 2010.

[55] Tokio Nakada, Daisuke Iga, Hiroki Ohbo, and Akio Kunioka. Effects of sodium on Cu(In,Ga)Se_2-based thin films and solar cells. *Jpn. J. Appl. Phys.*, 36(2R):732, 1997.

[56] Sodium co-evaporation for low temperature Cu(In,Ga)Se_2 deposition. *Thin Solid Films*, 387(1-2):33, 2001. Proceeedings of Symposium N on Thin Film Photovoltaicmaterials of the E-MRS Spring Conference.

[57] David W. Niles, Kannan Ramanathan, Falah Hasoon, Rommel Noufi, Brian J. Tielsch, and Julia E. Fulghum. Na impurity chemistry in photovoltaic CIGS thin films: Investigation with X-ray photoelectron spectroscopy. *J. Vac. Sci. Technol., A*, 15(6):3044, 1997.

[58] Leeor. Kronik, David Cahen, and Hans Werner Schock. Effects of sodium on polycrystalline Cu(In,Ga)Se_2 and its solar cell performance. *Adv. Mater.*, 10(1):31, 1998.

[59] E.S. Mungan, Xufeng Wang, and M.A. Alam. Modeling the effects of Na incorporation on CIGS solar cells. *IEEE J. Photovoltaics*, 3(1):451, Jan 2013.

[60] P. Reinhard, A. Chirila, P. Blosch, F. Pianezzi, S. Nishiwaki, S. Buechelers, and A.N. Tiwari. Review of progress toward 20% efficiency flexible CIGS solar cells and manufacturing issues of solar modules. *IEEE J. Photovoltaics*, 3(1):572, Jan 2013.

[61] P. Reinhard, F. Pianezzi, B. Bissig, A. Chirila, P. Bloesch, S. Nishiwaki, S. Buecheler, and A.N. Tiwari. Cu(In,Ga)Se_2 thin-film solar cells and modules-a boost in efficiency due to potassium. *IEEE J. Photovoltaics*, 5(2):656, 2015.

[62] Fabian Pianezzi, Patrick Reinhard, Adrian Chirila, Benjamin Bissig, Shiro Nishiwaki, Stephan Buecheler, and Ayodhya N. Tiwari. Unveiling the effects of post-deposition treatment with different alkaline elements on the electronic properties of CIGS thin film solar cells. *Phys. Chem. Chem. Phys.*, 16:8843, 2014.

[63] Miguel A. Contreras, Manuel J. Romero, Bobby To, F. Hasoon, R. Noufi, S. Ward, and K. Ramanathan. Optimization of CBD CdS process in high-efficiency Cu(In,Ga)Se_2-based solar cells. *Thin Solid Films*, 403-404(0):204, 2002.

[64] D. Güttler, A. Chirila, S. Seyrling, P. Blösch, S. Buecheler, X. Fontanee, V. Izquierdo-Roca, L. Calvo-Barrio, A. Pereez-Rodriguez, J. R. Morante, A. Eicke, and A. N. Tiwari. Influence of NaF incorporation during Cu(In,Ga)Se_2 growth on microstructure and photovoltaic performance. *35th IEEE Photovoltaics Spec. Conf.*, page 003420, 2010.

[65] A. Rockett, J.S. Britt, T. Gillespie, C. Marshall, M.M. Al Jassim, F. Hasoon, R. Matson, and B. Basol. Na in selenized Cu(In,Ga)Se_2 on Na-containing and Na-free glasses: distribution, grain structure, and device performances. *Thin Solid Films*, 372(1-2):212, 2000.

[66] J. C. Slater. The theory of complex spectra. *Phys. Rev.*, 34:1293, 1929.

[67] D. R. Hartree. The wave mechanics of an atom with a non-coulomb central field. part I- theory and methods. *Math. Proc. Cambridge Philos. Soc.*, 24:89, 1928.

[68] D. R. Hartree. The wave mechanics of an atom with a non-coulomb central field. part II- some results and discussion. *Math. Proc. Cambridge Philos. Soc.*, 24:111, 1928.

[69] J. C. Slater. Note on hartree's method. *Phys. Rev.*, 35:210, 1930.

[70] Per-Olov Löwdin. *Correlation Problem in Many-Electron Quantum Mechanics I. Review of Different Approaches and Discussion of Some Current Ideas*, page 207. John Wiley & Sons, Inc., 2007.

[71] P. Hohenberg and W. Kohn. Inhomogeneous electron gas. *Phys. Rev.*, 136:B864, 1964.

[72] W. Kohn and L. J. Sham. Self-consistent equations including exchange and correlation effects. *Phys. Rev.*, 140:A1133, 1965.

[73] R.G. Parr and W. Yang. *Density-Functional Theory of Atoms and Molecules*. International Series of Monographs on Chemistry. Oxford University Press, USA, 1994.

[74] G. L. Oliver and J. P. Perdew. Spin-density gradient expansion for the kinetic energy. *Phys. Rev. A*, 20:397, 1979.

[75] Yue Wang and John P. Perdew. Spin scaling of the electron-gas correlation energy in the high-density limit. *Phys. Rev. B*, 43:8911, 1991.

[76] John P. Perdew, Kieron Burke, and Matthias Ernzerhof. Generalized gradient approximation made simple. *Phys. Rev. Lett.*, 77:3865, 1996.

[77] Joachim Paier, Robin Hirschl, Martijn Marsman, and Georg Kresse. The perdew-burke-ernzerhof exchange-correlation functional applied to the G2-1 test set using a plane-wave basis set. *J. Chem. Phys.*, 122(23):234102, 2005.

[78] J. Paier, M. Marsman, K. Hummer, G. Kresse, I. C. Gerber, and J. G. Angyan. Screened hybrid density functionals applied to solids. *J. Chem. Phys.*, 124(15):154709, 2006.

[79] Charles Kittel. *Introduction to Solid State Physics*. 1996.

[80] Neil W. Ashcroft and N. David Mermin. *Solid State Physics*. 1976.

[81] H. Hellmann. A new approximation method in the problem of many electrons. *J. Chem. Phys.*, 3(1):61, 1935.

[82] M. C. Payne, M. P. Teter, D. C. Allan, T. A. Arias, and J. D. Joannopoulos. Iterative minimization techniques for *ab initio* total-energy calculations: molecular dynamics and conjugate gradients. *Rev. Mod. Phys.*, 64:1045, 1992.

[83] Hendrik J. Monkhorst and James D. Pack. Special points for brillouin-zone integrations. *Phys. Rev. B*, 13:5188, 1976.

[84] Juana Moreno and José M. Soler. Optimal meshes for integrals in real- and reciprocal-space unit cells. *Phys. Rev. B*, 45:13891, 1992.

[85] Chris G. Van de Walle, P. J. H. Denteneer, Y. Bar-Yam, and S. T. Pantelides. Theory of hydrogen diffusion and reactions in crystalline silicon. *Phys. Rev. B*, 39:10791, May 1989.

[86] Hannu-Pekka Komsa, Tapio T. Rantala, and Alfredo Pasquarello. Finite-size supercell correction schemes for charged defect calculations. *Phys. Rev. B*, 86:045112, Jul 2012.

[87] Stephan Lany and Alex Zunger. Assessment of correction methods for the band-gap problem and for finite-size effects in supercell defect calculations: Case studies for ZnO and GaAs. *Phys. Rev. B*, 78:235104, 2008.

[88] S. B. Zhang and John E. Northrup. Chemical potential dependence of defect formation energies in GaAs: Application to Ga self-diffusion. *Phys. Rev. Lett.*, 67:2339, Oct 1991.

[89] S. A. Arrhenius. Über die Dissociationswärme und den Einfluss der Temperatur auf den Dissociationsgrad der Elektrolyte. *Z. Physik. Chem.*, 4:96, 1889.

[90] H. Pelzer and E. Wigner. The speed constansts of the exchange reactions. *Z. Phys. Chem.*, B15:445, 1932.

[91] E. Wigner. Effects of the electron interaction on the energy levels of electrons in metals. *Trans. Faraday Soc.*, 34:678, 1938.

[92] M. G. Evans and M. Polanyi. Some applications of the transition state method to the calculation of reaction velocities, especially in solution. *Trans. Faraday Soc.*, 31:875, 1935.

[93] Henry Eyring. The activated complex in chemical reactions. *J. Chem. Phys.*, 3, 1935.

[94] John W. Moore and Ralph G. Pearson. *Kinetics and Mechanism.* John Wiley & Sons, Inc., 1961.

[95] Gregory Mills and Hannes Jonsson. Quantum and thermal effects in H_2 dissociative adsorption: Evaluation of free energy barriers in multidimensional quantum systems. *Phys. Rev. Lett.*, 72:1124, Feb 1994.

[96] Gregory Mills, Hannes Jonsson, and Gregory K. Schenter. Reversible work transition state theory: application to dissociative adsorption of hydrogen. *Surf. Sci.*, 324(2-3):305, 1995.

[97] Michael L. Mckee and Michael Page. *Computing Reaction Pathways on Molecular Potential Energy Surfaces*, page 35. John Wiley & Sons, Inc., 2007.

[98] Charles J. Cerjan and William H. Miller. On finding transition states. *J. Chem. Phys.*, 75(6):2800, 1981.

[99] Dzung T. Nguyen and David A. Case. On finding stationary states on large-molecule potential energy surfaces. *J. Phys. Chem.*, 89(19):4020, 1985.

[100] Hugh Taylor and Jack Simons. Imposition of geometrical constraints on potential energy surface walking procedures. *J. Phys. Chem.*, 89(4):684, 1985.

[101] Jon Baker. An algorithm for the location of transition states. *J. Comput. Chem.*, 7(4):385, 1986.

[102] Wolfgang Quapp. A gradient-only algorithm for tracing a reaction path uphill to the saddle of a potential energy surface. *Chem. Phys. Lett.*, 253(3-4):286, 1996.

[103] Carlos Gonzalez and H. Bernhard Schlegel. An improved algorithm for reaction path following. *J. Chem. Phys.*, 90(4):2154, 1989.

[104] Carlos. Gonzalez and H. Bernhard. Schlegel. Reaction path following in mass-weighted internal coordinates. *J. Phys. Chem.*, 94(14):5523, 1990.

[105] Carlos Gonzalez and H. Bernhard Schlegel. Improved algorithms for reaction path following: Higher-order implicit algorithms. *J. Chem. Phys.*, 95(8), 1991.

[106] H. P. Hratchian and H. B. Schlegel. Using hessian updating to increase the efficiency of a hessian based predictor-corrector reaction path following method. *J. Chem. Theory Comput.*, 1(1):61, 2005.

[107] Hrant P. Hratchian and Michael J. Frisch. Integrating steepest-descent reaction pathways for large molecules. *J. Chem. Phys.*, 134(20):204103, 2011.

[108] Lawrence R. Pratt. A statistical method for identifying transition states in high dimensional problems. *J. Chem. Phys.*, 85(9), 1986.

[109] H. Jonsson, G. Mills, and K. W. Jacobsen. Nudged elastic band method for finding minimum energy paths of transitions, in classical and quantum dynamics in condensed phase simulations. *Worlds Scientific, Singapore*, page 385, 1998.

[110] Dominic R. Alfonso and Kenneth D. Jordan. A flexible nudged elastic band program for optimization of minimum energy pathways using ab initio electronic structure methods. *J. Comput. Chem.*, 24(8):990, 2003.

[111] Ryszard Czerminski and Ron Elber. Reaction path study of conformational transitions in flexible systems: Applications to peptides. *J. Chem. Phys.*, 92(9):5580, 1990.

[112] E. Weinan, W. Ren, and E. Vanden-Eijnden. Finite temperature string method for the study of rare events. *J. Phys. Chem. B*, 109(14):6688, 2005.

[113] R. Elber and M. Karplus. A method for determining reaction paths in large molecules: Application to myoglobin. *Chem. Phys. Lett.*, 139(5):375, 1987.

[114] J.J. Mortensen, Y. Morikawa, B. Hammer, and J.K. Norskov. Density functional calculations of N_2 adsorption and dissociation on a Ru(0001) surface. *J. Catal.*, 169(1):85, 1997.

[115] Graeme Henkelman, Blas P. Uberuaga, and Hannes Jonsson. A climbing image nudged elastic band method for finding saddle points and minimum energy paths. *J. Chem. Phys.*, 113(22):9901, 2000.

[116] Graeme Henkelman and Hannes Jonsson. Improved tangent estimate in the nudged elastic band method for finding minimum energy paths and saddle points. *J. Chem. Phys.*, 113(22):9978, 2000.

[117] M. I. Hoffert, K. Caldeira, A. K. Jain, E. F. Haites, L. D. D. Harvey, S. D. Potter, S. H. Schneider, R. G. Watts, T. M. L. Wigley, and D. J. Wuebbles. Energy implications of future stabilization of atmospheric CO_2 content. *Nature*, 395:881, 1998.

[118] Philip Jackson, Dimitrios Hariskos, Roland Wuerz, Oliver Kiowski, Andreas Bauer, Theresa Magorian Friedlmeier, and Michael Powalla. Properties of Cu(In,Ga)Se_2 solar cells with new record efficiencies up to 21.7%. *Phys. Status Solidi (RRL) - Rapid Res. Lett.*, 9(1):28, 2015.

[119] Martin A. Green, Keith Emery, Yoshihiro Hishikawa, Wilhelm Warta, and Ewan D. Dunlop. Solar cell efficiency tables (version 42). *Prog. Photovoltaics: Res. Appl.*, 21(5):827, 2013.

[120] P. Jackson, D. Hariskos, R. Wuerz, W. Wischmann, and M. Powalla. Compositional investigation of potassium doped Cu(In,Ga)Se_2 solar cells with efficiencies up to 20.8%. *Phys. Status Solidi RRL*, 8:219, 2014.

[121] T. Kobayashi, H. Yamaguchi, and T. Nakada. Effects of combined heat and light soaking on device performance of Cu(In,Ga)Se_2 solar cells with ZnS(O,OH) buffer layer. *Progr. Photovoltaics*, 22:115, 2014.

[122] M. Nakamura, Y. Kouji, Y. Chiba, H. Hakuma, T. Kobayashi, and T. Nakada. Achievement of 19.7% efficiency with a small-sized Cu(In,Ga)$(SeS)_2$ solar cells prepared by sulfurization after selenizaion process with Zn-based buffer. *39th IEEE PVSC*, page 0849, 2013.

[123] Janos Kiss, Thomas Gruhn, Guido Roma, and Claudia Felser. Theoretical study on the structure and energetics of Cd insertion and Cu depletion of $CuIn_5Se_8$. *J. Phys. Chem. C*, 117(21):10892, 2013.

[124] Björn A. Andersson. Materials availability for large-scale thin-film photovoltaics. *Prog. Photovoltaics: Res. Appl.*, 8(1):61, 2000.

[125] Shogo Ishizuka, Akimasa Yamada, Paul J. Fons, Hajime Shibata, and Shigeru Niki. Interfacial alkali diffusion control in chalcopyrite thin-film solar cells. *ACS Appl. Mater. Interfaces*, 6(16):14123, 2014.

[126] J.E. Granata, J.R. Sites, S. Asher, and R.J. Matson. Quantitative incorporation of sodium in $CuInSe_2$ and Cu(In,Ga)Se_2 photovoltaic devices. In *Photovoltaic Specialists Conference, 1997., Conference Record of the Twenty-Sixth IEEE*, page 387, Sep 1997.

[127] D. Braunger, D. Hariskos, G. Bilger, U. Rau, and H.W. Schock. Influence of sodium on the growth of polycrystalline Cu(In,Ga)Se_2 thin films. *Thin Solid Films*, 361-362:161, 2000.

[128] David J. Schroeder and Angus A. Rockett. Electronic effects of sodium in epitaxial $CuIn_{(1-x)}Ga_xSe_2$. *J. Appl. Phys.*, 82(10):4982, 1997.

[129] Dominik Rudmann. *Effect of sodium on growth and properties of Cu(In,Ga)Se_2 thin film solar cells.* PhD thesis, Swiss federal institute of technology (ETH) Zuerich, 2004.

[130] Dong Han, Y. Y. Sun, Junhyeok Bang, Y. Y. Zhang, Hong-Bo Sun, Xian-Bin Li, and S. B. Zhang. Deep electron traps and origin of p-type conductivity in the earth-abundant solar-cell material Cu_2ZnSnS_4. *Phys. Rev. B*, 87:155206, Apr 2013.

[131] U. Rau and H.W. Schock. Electronic properties of Cu(In,Ga)Se_2 heterojunction solar cells-recent achievements, current understanding, and future challenges. *Appl. Phys. A*, 69(2):131, 1999.

[132] Su-Huai Wei, S. B. Zhang, and Alex Zunger. Effects of Na on the electrical and structural properties of $CuInSe_2$. *J. Appl. Phys.*, 85(10):7214, 1999.

[133] G. Kresse and J. Furthmueller. Efficient iterative schemes for ab initio total-energy calculations using a plane-wave basis set. *Phys. Rev. B*, 54:11169, Oct 1996.

[134] G. Kresse and J. Furthmueller. Efficiency of ab-initio total energy calculations for metals and semiconductors using a plane-wave basis set. *Comput. Mater. Sci.*, 6(1):15, 1996.

[135] G. Kresse and D. Joubert. From ultrasoft pseudopotentials to the projector augmented-wave method. *Phys. Rev. B*, 59:1758, Jan 1999.

[136] P. E. Bloechl. Projector augmented-wave method. *Phys. Rev. B*, 50:17953, Dec 1994.

[137] Jochen Heyd, Gustavo E. Scuseria, and Matthias Ernzerhof. Hybrid functionals based on a screened coulomb potential. *J. Chem. Phys.*, 118(18):8207, 2003.

[138] Y. Kumagai, Y. Soda, F. Oba, A. Seko, and I. Tanaka. First-principles calculations of the phase diagrams and band gaps in $CuInSe_2$-$CuGaSe_2$ and $CuInSe_2$-$CuAlSe_2$ pseudobinary systems. *Phys. Rev. B*, 85:033203, 2012.

[139] Y. Hinuma, F. Oba, Y. Kumagai, and I. Tanaka. Ionization potentials of (112) and (11-2) facet surfaces of $CuInSe_2$ and $CuGaSe_2$. *Phys. Rev. B*, 86:245433, 2012.

[140] Janos Kiss, Thomas Gruhn, Guido Roma, and Claudia Felser. Theoretical study on the diffusion mechanism of Cd in the Cu-poor phase of $CuInSe_2$ solar cell material. *J. Phys. Chem. C*, 117:25933, 2013.

[141] J. Pohl and K. Albe. Intrinsic point defects in $CuInSe_2$ and $CuGaSe_2$ as seen via screened-exchange hybrid density functional theory. *Phys. Rev. B*, 87:245203, 2013.

[142] Johan Pohl, Andreas Klein, and Karsten Albe. Role of copper interstitials in $CuInSe_2$: First-principles calculations. *Phys. Rev. B*, 84:121201, Sep 2011.

[143] Hiroaki Matsushita, Takashi Maeda, Akinori Katsui, and Takeo Takizawa. Thermal analysis and synthesis from the melts of Cu-based quaternary compounds Cu-III-IV-VI_4 and Cu_2-II-IV-VI_4 (II=Zn, Cd; III=Ga, In; IV=Ge, Sn; VI=Se). *J. Cryst. Growth*, 208(1-4):416, 2000.

[144] Hironori Katagiri, Kotoe Saitoh, Tsukasa Washio, Hiroyuki Shinohara, Tomomi Kurumadani, and Shinsuke Miyajima. Development of thin film solar cell based on Cu_2ZnSnS_4 thin films. *Sol. Energy Mater. Sol. Cells*, 65(1-4):141, 2001.

[145] Min-Ling Liu, Fu-Qiang Huang, Li-Dong Chen, and I-Wei Chen. A wide-band-gap p-type thermoelectric material based on quaternary chalcogenides of Cu_2ZnSnQ_4(Q=S,Se). *Appl. Phys. Lett.*, 94(20):202103, 2009.

[146] G. Suresh Babu, Y.B. Kishore Kumar, P. Uday Bhaskar, and Sundara Raja Vanjari. Effect of Cu/(Zn+Sn) ratio on the properties of co-evaporated $Cu_2ZnSnSe_4$ thin films. *Sol. Energy Mater. Sol. Cells*, 94(2):221, 2010.

[147] W Paszkowicz, R Lewandowska, and R Bacewicz. Rietveld refinement for $CuInSe_2$ and $CuIn_3Se_5$. *J. Alloys Compd.*, 362(1-2):241, 2004. Proceedings of the Sixth International School and Symposium on Synchrotron Radiation in Natural Science (ISSRNS).

[148] G. Ariswan, El Haj Moussa, F. Guastavino, and C. Llinares. Band gap of $CuInSe_2$ thin films fabricated by flash evaporation determined from transmission data. *J. Mater. Sci. Lett.*, 21(3):215, 2002.

[149] L. Duran, C. Guerrero, E. Hernandez, J.M. Delgado, J. Contreras, S.M. Wasim, and C.A. Durante Rincon. Structural, optical and electrical properties of $CuIn_5Se_8$ and $CuGa_5Se_8$. *J. Phys. Chem. Solids*, 64(9-10):1907, 2003. 13th International Conference on Ternary and Multinary Compounds.

[150] C. Rincon, S. M. Wasim, G. Marin, R. Marquez, L. Nieves, G. Sanchez Perez, and E. Medina. Temperature dependence of the optical energy gap and urbachs energy of $CuIn_5Se_8$. *J. Appl. Phys.*, 90(9):4423, 2001.

[151] Hitoshi Tampo, Kikuo Makita, Hironori Komaki, Akimasa Yamada, Shigenori Furue, Shogo Ishizuka, Hajime Shibata, Koji Matsubara, and Shigeru Niki. Composition control of $Cu_2ZnSnSe_4$-based solar cells grown by coevaporation. *Thin Solid Films*, 551:27, 2014.

[152] F. Gao, S. Yamazoe, T. Maeda, and T. Wada. Structural study of cu-deficient $Cu_{2(1-x)}ZnSnSe_4$ solar cell materials by X-ray diffraction and X-ray absorption fine structure. *Jpn. J. Appl. Phys.*, 51:10NC28, 2012.

[153] M. Grossberg, J. Krustok, K. Timmo, and M. Altosaar. Radiative recombination in $Cu_2ZnSnSe_4$ monograins studied by photoluminescence spectroscopy. *Thin Solid Films*, 517(7):2489, 2009.

[154] SeJin Ahn, Sunghun Jung, Jihye Gwak, Ara Cho, Keeshik Shin, Kyunghoon Yoon, Doyoung Park, Hyeonsik Cheong, and Jae Ho Yun. Determination of band gap

energy (Eg) of $Cu_2ZnSnSe_4$ thin films: On the discrepancies of reported band gap values. *Appl. Phys. Lett.*, 97(2):021905, 2010.

[155] T. M. Friedlmeier, N. Wieser, T. Walter, H. Dittrich, and H. W. Schock. Heterojuncitons based on Cu_2ZnSnS_4 and $Cu_2ZnSnSe_4$ thin films. *Proc. of the 14th Eur. Conf. Photovoltaic Sci. Eng. Exhibition*, page 1242, 1997.

[156] L.E. Oikkonen, M.G. Ganchenkova, AP. Seitsonen, and R.M. Nieminen. Vacancies in $CuInSe_2$: new insights from hybrid-functional calculations. *J. Phys.: Condens. Matter*, Oct 2011.

[157] Johan Pohl and Karsten Albe. Thermodynamics and kinetics of the copper vacancy in $CuInSe_2$, $CuGaSe_2$, $CuInS_2$, and $CuGaS_2$ from screened-exchange hybrid density functional theory. *J. Appl. Phys.*, 108(2):023509, 2010.

[158] L.E. Oikkonen, M.G. Ganchenkova, AP. Seitsonen, and R.M. Nieminen. Effect of sodium incorporation into $CuInSe_2$ from first principles. *J. Appl. Phys.*, 114(8):083503, Aug 2013.

[159] Fabian Hans Pianezzi. *Electronic transport and doping mechanisms in Cu(In,Ga)Se_2 thin film solar cells.* PhD thesis, ETH Zurich, 2014.

[160] Shiyou Chen, Xin-Gao Gong, Aron Walsh, and Su-Huai Wei. Structural, electronic and defect properties of $Cu_2ZnSn(S,Se)_4$ alloys. In *Symposium YY - Computational Semiconductor Materials Science*, volume 1370 of *MRS Online Proceedings Library Archive*, 2011.

[161] Elaheh Ghorbani, Janos Kiss, Hossein Mirhosseini, Markus Schmidt, Johannes Windeln, Thomas D. Kuehne, and Claudia Felser. Insights into intrinsic defects and the incorporation of Na and K in the $Cu_2ZnSnSe_4$ thin-film solar cell material from hybrid-functional calculations. *J. Phys. Chem. C*, 120(4):2064–2069, 2016.

[162] Tsuyoshi Maeda, Atsuhito Kawabata, and Takahiro Wada. First-principles study on alkali-metal effect of Li, Na, and K in Cu_2ZnSnS_4 and $Cu_2ZnSnSe_4$. *Phys. Status Solidi C*, 12(6):631, 2015.

[163] Silvana Botti, David Kammerlander, and Miguel A. L. Marques. Band structures of Cu_2ZnSnS_4 and $Cu_2ZnSnSe_4$ from many-body methods. *Appl. Phys. Lett.*, 98(24):241915, 2011.

[164] Elaheh Ghorbani, Janos Kiss, Hossein Mirhosseini, Guido Roma, Markus Schmidt, Johannes Windeln, Thomas D. Kühne, and Claudia Felser. Hybrid-functional calculations on the incorporation of Na and K impurities into the $CuInSe_2$ and $CuIn_5Se_8$ solar-cell materials. *J. Phys. Chem. C*, 119(45):25197, 2015.

[165] Elaheh Ghorbani, Hossein Mirhosseini, Janos Kiss, and Claudia Felser. Incorporation of Li dopant into $Cu_2ZnSnSe_4$ photovoltaic absorber: hybrid-functional calculations. *J. Phys. D: Appl. Phys.*, 48(48):482001, 2015.

[166] Viktor Ivády, I. A. Abrikosov, E. Janzén, and A. Gali. Role of screening in the density functional applied to transition-metal defects in semiconductors. *Phys. Rev. B*, 87:205201, May 2013.

[167] LE Oikkonen, MG Ganchenkova, AP Seitsonen, and RM Nieminen. Mass transport in $CuInSe_2$ from first principles. *Journal of Applied Physics*, 113(13):133510, 2013.

[168] P. Migliorato, J. L. Shay, H. M. Kasper, and Sigurd Wagner. Analysis of the electrical and luminescent properties of $CuInSe_2$. *Journal of Applied Physics*, 46(4):1777, 1975.